BARIUM RELEASES at ALTITUDES BETWEEN 200 and 1000 KILOMETERS

A JOINT MAX-PLANCK-INSTITUT– NASA EXPERIMENT

NATIONAL AERONAUTICS AND SPACE ADMINISTRATION

BARIUM RELEASES at ALTITUDES BETWEEN 200 and 1000 KILOMETERS

A JOINT MAX-PLANCK-INSTITUT– NASA EXPERIMENT

Compiled by

HAL T. BABER, JR., KENNETH H. CRUMBLY, AND DAVID ADAMSON

Prepared at
NASA Langley Research Center

FOREWORD

In September 1966 two sounding rockets were launched from Wallops Island, Virginia, under a joint agreement between the National Aeronautics and Space Administration and der Bundeministerium für wissenschaftliche Forschung of West Germany. The Langley Research Center, Hampton, Virginia, represented the NASA with the Institut für extraterrestrische Physik am Max-Planck-Institut für Physik und Astrophysik, Garching b. München representing the West German Government. These rocket vehicles carried barium chemical release payloads to produce artificial clouds in the ionosphere and the exosphere.

This publication presents the results of the observation of these artificial clouds, both neutral and ionized. Data are presented on the payload yield, expansion of the neutral cloud, ionization, and growth and motion of the ionized cloud. Payload and vehicle descriptions are also given.

Participants in the joint experiment from the following agencies and educational institutions have contributed to this document:

> NASA – Langley Research Center
> MPI – Institut für extraterrestrische Physik
> Johns Hopkins University – Institute for Cooperative Research
> North Carolina State University – Department of Physics
> Georgia Institute of Technology – School of Aerospace Engineering

Page intentionally left blank

CONTENTS

I. INTRODUCTION

By Hal T. Baber, Jr.
NASA Langley Research Center

A broad picture of the topology of the earth's magnetic field has emerged in recent years through data obtained from magnetometers flown on satellites. One shortcoming of such data lies in the fact that magnetometers make point-to-point measurements along the spacecraft trajectory and one cannot therefore distinguish between spatial inhomogeneities and timewise fluctuations. In addition to learning more about the magnetic field, there is a pressing need to improve the knowledge of the electric fields in space about which, at present, virtually nothing is known.

The use of ionized clouds provides a direct means of charting electric and magnetic fields in space. The concept is simple. Neutral barium released in space and exposed to the sun's ultraviolet radiation rapidly becomes ionized. The individual ions composing the cloud spiral along the magnetic-field lines, and since they are excited by sunlight they can be seen when viewed against the night sky. As the cloud elongates along the field line, it serves to define the shape of the field line. Electric fields produce a motion of the field lines which, in turn, is imparted to the cloud and can therefore be measured.

In the period from 1963 to 1965 the Langley Research Center of the National Aeronautics and Space Administration (NASA) became interested in the use of ionized clouds for making direct measurements of the electric field in the magnetosphere. Results of theoretical (unpublished) calculations made at Langley Research Center indicated that the chemical release of ionized (or ionizable) particles, radiating in the visible region of the spectrum, held considerable promise for the aforementioned application. Meanwhile, under Professor Riemar Lüst, the Institut für extraterrestrische Physik of the Max-Planck-Institut für Physik und Astrophysik (hereinafter referred to as MPI) conducted a series of chemical-release payload-development test flights from rocket ranges in Africa and Europe (refs. I-1 and I-2). Of the several solid-chemical systems tested, a mixture of barium and copper oxide (75 percent Ba, 25 percent CuO, by weight) provided the best yield of ionized barium vapor. With an adequately functioning barium-release payload now available, MPI in May 1965 requested NASA participation in joint barium-release experiments from Wallops Island, Virginia. In implementation of this cooperative international effort, NASA Headquarters requested in November 1965 that Langley Research Center coordinate this flight project because of their interest in the application of the barium ion cloud technique. One scientific objective of these joint experiments was to study the ion cloud technique at altitudes between 200 and 1000 km and to evaluate the technique for possible application to releases in deep space. A second objective was the

measurement of electric fields in the lower magnetosphere by optical observations of the motions of the ionized clouds.

The experiments consisted, essentially, of optical observations of multiple releases from payloads carried onboard two sounding rockets, one launched on September 24, 1966, and the other the following day. There were two releases from the first payload and three from the second. Rocket vehicle and release-point location details are presented in section II.

Results of observations of the artificial clouds produced by these barium releases in the exosphere and the ionosphere are presented. Due to the scientific interest in future application of the barium-release technique at much greater distances, the bulk of the analysis performed to date has been on the release at the maximum altitude, namely, 930 km. The contributions of the participants — supporting personnel as well as experimenters — are indicated, and the applicable references are given for each section.

It should be noted that sections V and X, which cover the analysis of the release from the Javelin at an altitude of about 930 km, were prepared independently by MPI and NASA project scientists, respectively; consequently, there are certain minor differences in interpretation. To avoid further delays in publication of these data no attempt has been made to resolve these differences.

REFERENCES

I-1. Föppl, H.; Haerendel, G.; Loidl, J.; Lüst, R.; Melzner, F.; Meyer, B.; Neuss, H.; and Rieger, E.: Preliminary Experiments for the Study of the Interplanetary Medium by the Release of Metal Vapour in the Upper Atmosphere. Planetary Space Sci., vol. 13, no. 2, Feb. 1965, pp. 95-114.

I-2. Föppl, H.; Haerendel, G.; Haser, L.; Loidl, J.; Lütjens, P.; Lüst, R.; Melzner, F.; Meyer, B.; Neuss, H.; and Rieger, E.: Artificial Strontium and Barium Clouds in the Upper Atmosphere. Planetary Space Sci., vol. 15, no. 2, Feb. 1967, pp. 357-372.

II. VEHICLES AND TRAJECTORIES

By Hal T. Baber, Jr.
NASA Langley Research Center

VEHICLE DESCRIPTION

In the barium-release experiment conducted on September 24, 1966, the payload was carried aloft by a Javelin sounding rocket. This rocket vehicle consists of four solid-propellant rocket motors. The four stages are Honest John M6, Nike Ajax M88 modified, Nike Ajax M88 modified, and Altair 1-A6, respectively. This vehicle is stabilized through third-stage burnout by cruciform fins attached to the aft end of each of the first three stages. Stabilization of the fourth stage is by spinning which is achieved by the canted fins of the preceding stages. More detailed information on this vehicle is presented in references II-1 and II-2.

The barium releases of September 25, 1966, were made from a Nike-Tomahawk, which is a two-stage sounding rocket vehicle. The two solid-propellant motors are Nike Ajax M88 modified and Tomahawk TE-M-416, respectively. Cruciform fins are attached to the aft end of each motor for stabilization and, as a result of being canted, provide a spin rate adequate for stabilization of the second stage at the higher altitudes where the dynamic pressure is insufficient for aerodynamic stability. More detail on this vehicle can be obtained from reference II-3.

TRAJECTORIES

The Javelin was launched at 9 hours 13 minutes UT and the Nike-Tomahawk was launched at 9 hours 51 minutes UT. Releases from the Javelin and Nike-Tomahawk occurred while both vehicles were coasting on a ballistic trajectory. In the following table, the release times (from launch) shown were determined from radar-signal enhancement. The altitude, horizontal range from Wallops Island, and the latitude and longitude of the release points are included in the table.

Release	Time, from launch, min	sec	Altitude, km	Horizontal range, km	Latitude, ^{o}N	Longitude, ^{o}W
Javelin						
First	3	44	506.6	246.4	37.29	72.77
Second	9	24.5	929.6	694.3	36.01	68.03
Nike-Tomahawk						
First	2	17.5	213	59.1	37.42	75.08
Second	3	25	267.8	89.3	37.19	74.88
Third	5	39	255.8	148.7	36.74	74.50

The relationship between altitude and horizontal range for the Javelin and Nike-Tomahawk flights is shown in figure II-1 and II-2, respectively, with release points indicated. Figures II-3 and II-4 show the ground track of the Javelin and Nike-Tomahawk, respectively, in a latitude-longitude geographic representation. Release points are also indicated in these figures.

REFERENCES

II-1. Anon.: Performance Summary for the Javelin Sounding Rocket Vehicle. Rep. No. AST/E1R-13326 (Contract No. NAS1-1013), Vought Astronautics, Chance Vought Corp., Apr. 18, 1961.

II-2. Clancy, Thomas; Clark, Leo J.; Daniels, Peter; Koplow, Michael; and Smallman, Frank: Methods of Computations of Aerodynamic Parameters for Javelin. Tech. Note 01756.01-1 (Contract NAS 5-2909), Vitro Lab., Vitro Corp. Amer., June 1963.

II-3. Anon.: NASA Nike-Tomahawk Handbook. Contract NAS5-9693, Astro-Met Div., Thiokol Chem. Corp., Dec. 19, 1966.

Horizontal range, km
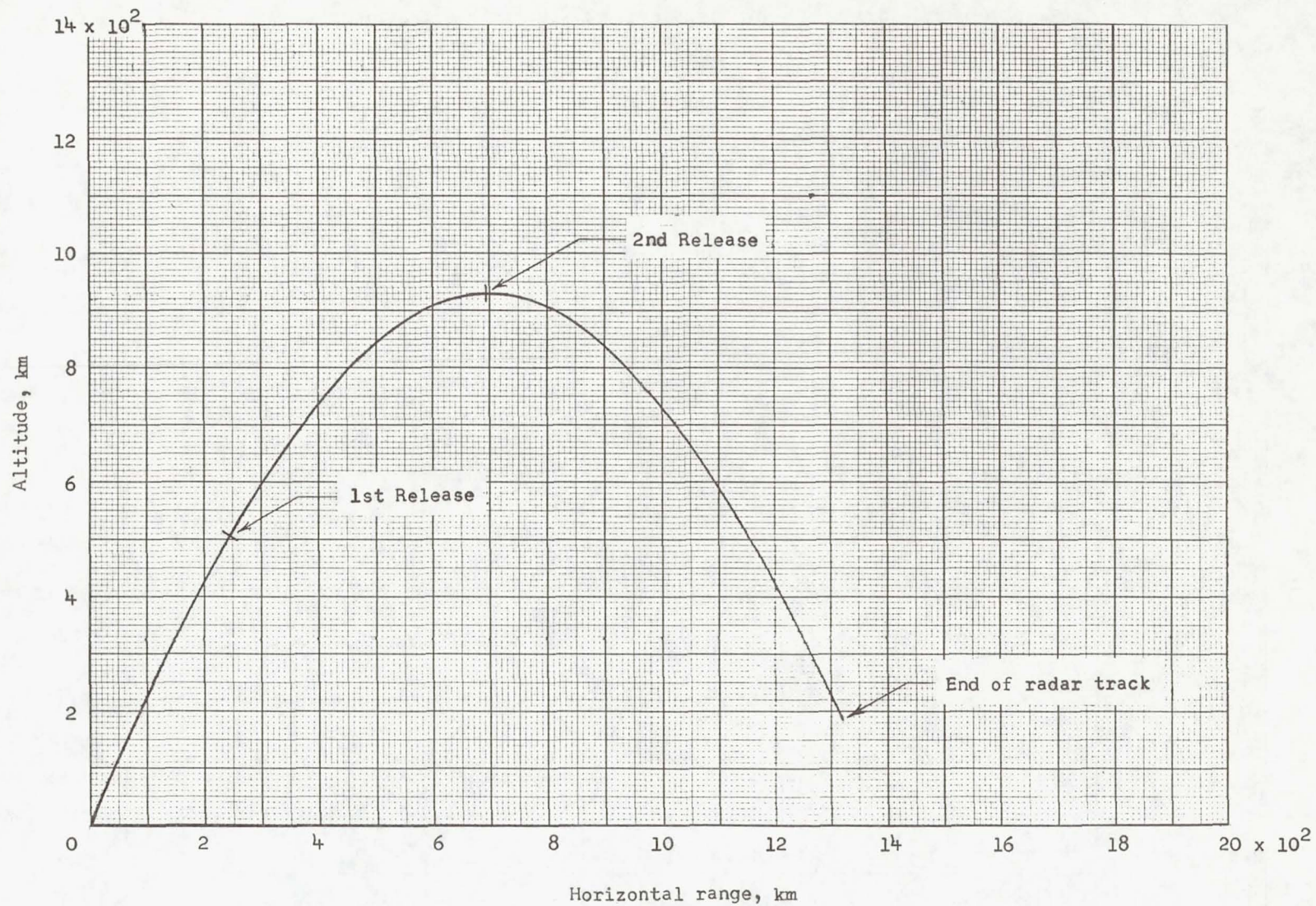
(Curved earth distance from launcher to vehicle projection on earth)

Figure II-1.- Javelin trajectory profile.

Figure II-2.- Nike-Tomahawk trajectory profile.
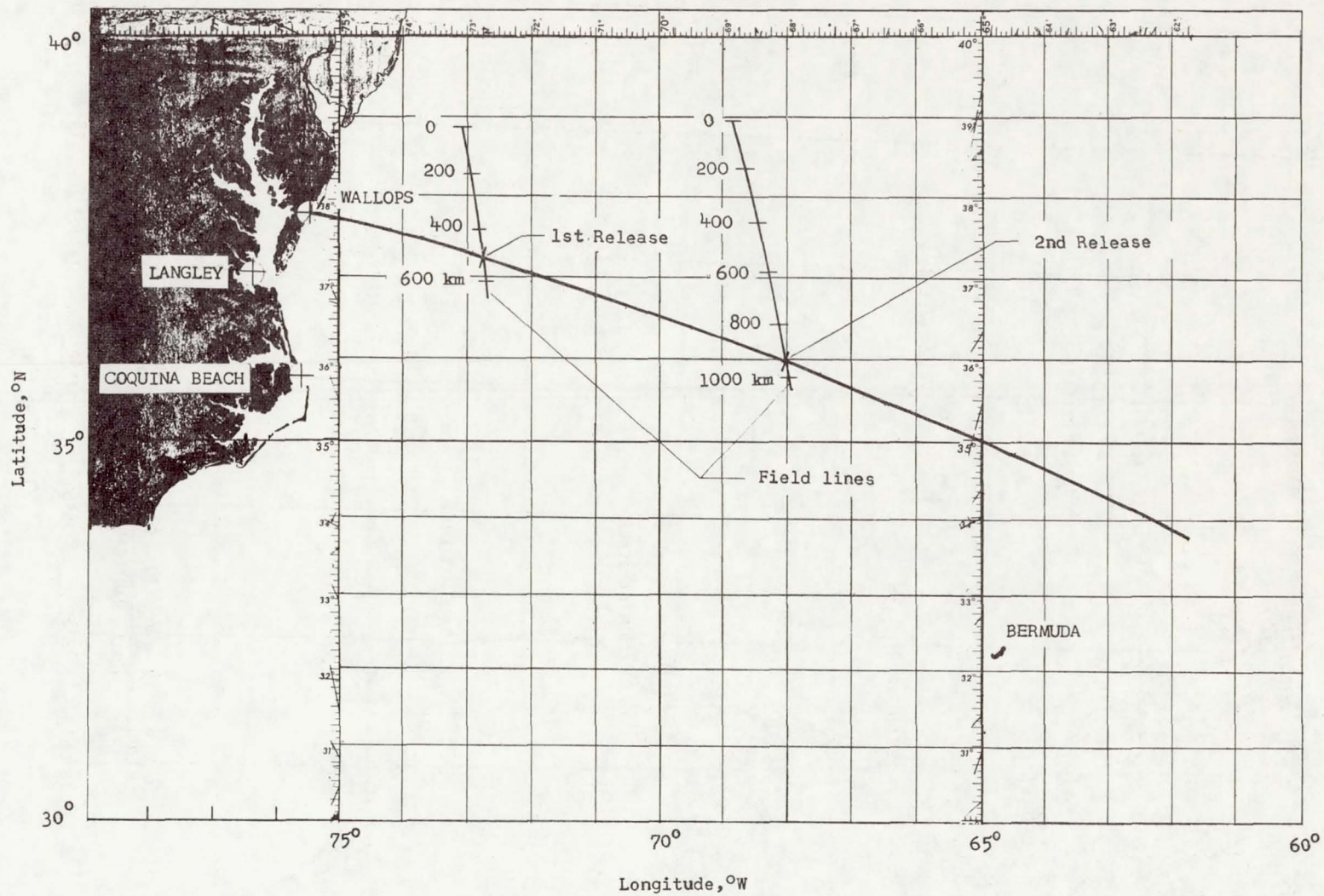
Figure 11-3.- Ground track of Javelin.
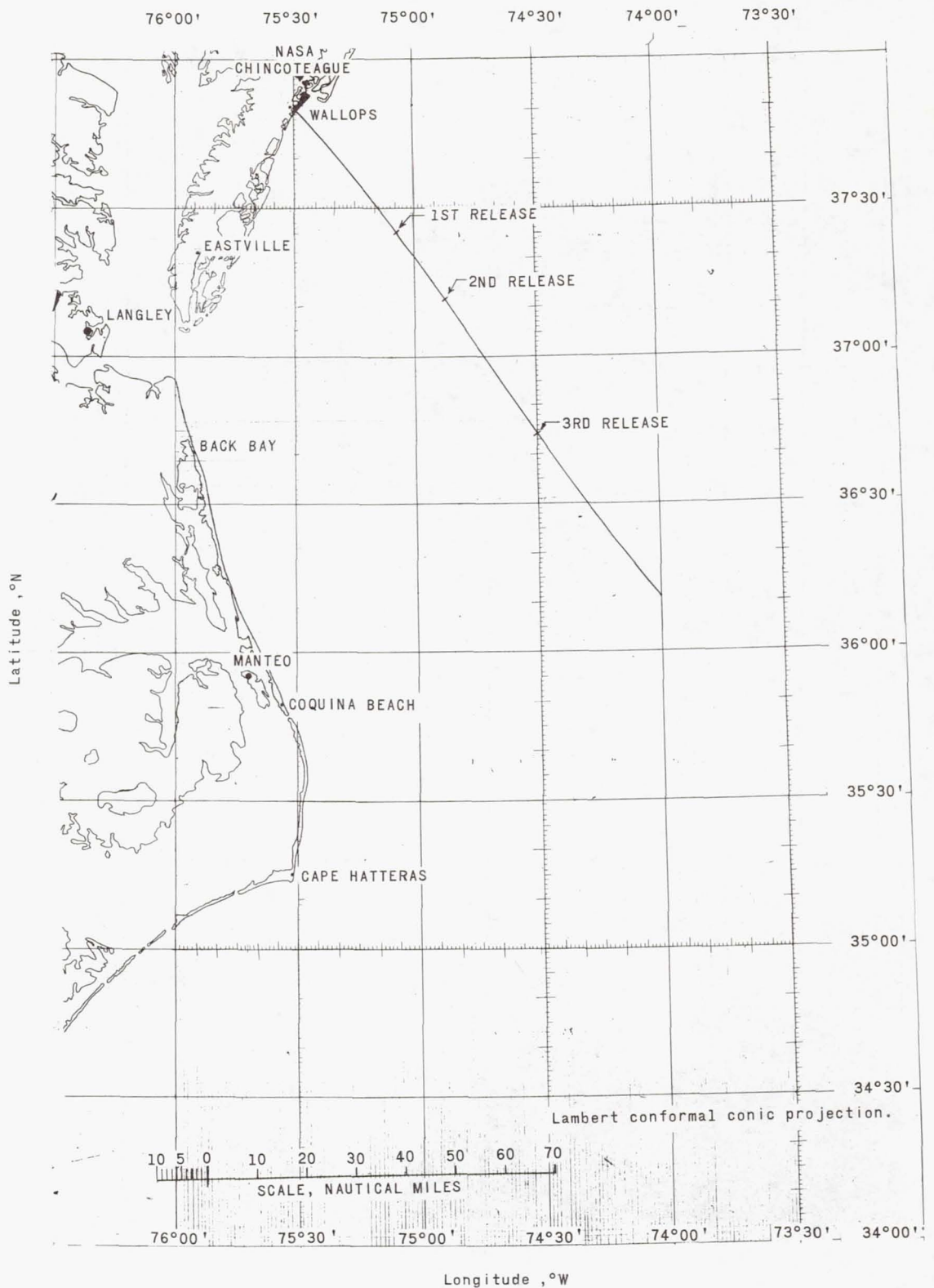
Figure II-4.- Ground track of Nike-Tomahawk.

8

III. PAYLOAD DESCRIPTION

By H. Föppl and J. Stöcker
Institut für extraterrestrische Physik,
Max-Planck-Institut für Physik und Astrophysik

JAVELIN PAYLOAD

The payload section of the Javelin rocket (fig. III-1) carried three cylindrical containers, or canisters, with longitudinal axes oriented orthogonal to the longitudinal axis of the rocket. The two lower containers were mounted back to back and were ignited simultaneously for production of the upper cloud. The axes of the nozzles were either parallel to, or coincident with, the longitudinal axes of the containers. The container in the upper part was filled with 957 grams of the mixture of barium (Ba) and copper oxide (CuO), whereas each of the two lower containers carried about 5.7 kilograms. Details of the chemical composition of this mixture are given in table III-I. The small quantity of strontium carbonate ($SrCO_3$) functioned as a gas former to increase pressure in the containers upon ignition. Following the reaction and release, the strontium, since it was not photoionized and has a high rate of excitation, aided in definition of the neutral cloud.

Between the two lower canisters and the small upper canister was the ignition electronics, which had two independent, identical circuits for redundancy. Each circuit consisted of one mechanical timer, two parallel baroswitches, and one set of silver-cell batteries. The igniters were squib type. The small container was equipped with one igniter, whereas the two large containers had two each.

Timer setting for the small container (lower cloud) was 218 seconds (actual, 224 seconds) and for the two large ones 558 seconds (actual, 564.5 seconds) after launch.

From the second Javelin cloud a yield of about 2 percent of the total weight was deduced, or about 6 percent of the maximum vaporizable amount of barium which is listed in the last column of table III-I.

NIKE-TOMAHAWK PAYLOAD

A sketch of the payload, as flown on the Nike-Tomahawk, is shown in figure III-2. The Nike-Tomahawk carried five containers, four of which were similar to the large ones on the Javelin. Each of these was filled with about 5 kilograms of mixture. See table III-I for composition details. The longitudinal axes of the containers were parallel to the longitudinal axis of the rocket with the nozzles in the cylindrical part of the container wall. Two main clouds were produced by igniting two of the large containers for each cloud.

The first cloud, intended as a small tracer, was generated by a small container filled with about 400 grams of mixture and situated in the bottom part of the payload. Times and locations of the three discrete releases are presented in section II. All releases resulted in visible clouds.

TABLE III-I.- CHEMICAL COMPOSITION OF MIXTURE

Release	Mixture weight, g	Composition of mixture						Moles of excess Ba
		Weight, g			Moles			
		Ba	CuO	$SrCO_3$	Ba	CuO	$SrCO_3$	
Javelin								
First	957	684	241	31	4.98	3.03	0.21	1.95
Second	5788	4144	1456	188	30.2	18.3	1.27	11.9
	5684	4070	1430	184	29.7	18.0	1.25	11.7
Nike-Tomahawk								
First	413	296	104	13	2.15	1.31	0.1	0.84
Second	5063	3625	1273	164	26.4	16.0	1.12	10.4
	4961	3551	1249	161	25.85	15.7	1.10	10.15
Third	5168	3695	1305	168	26.9	16.4	1.14	10.5
	5168	3695	1305	168	26.9	16.4	1.14	10.5
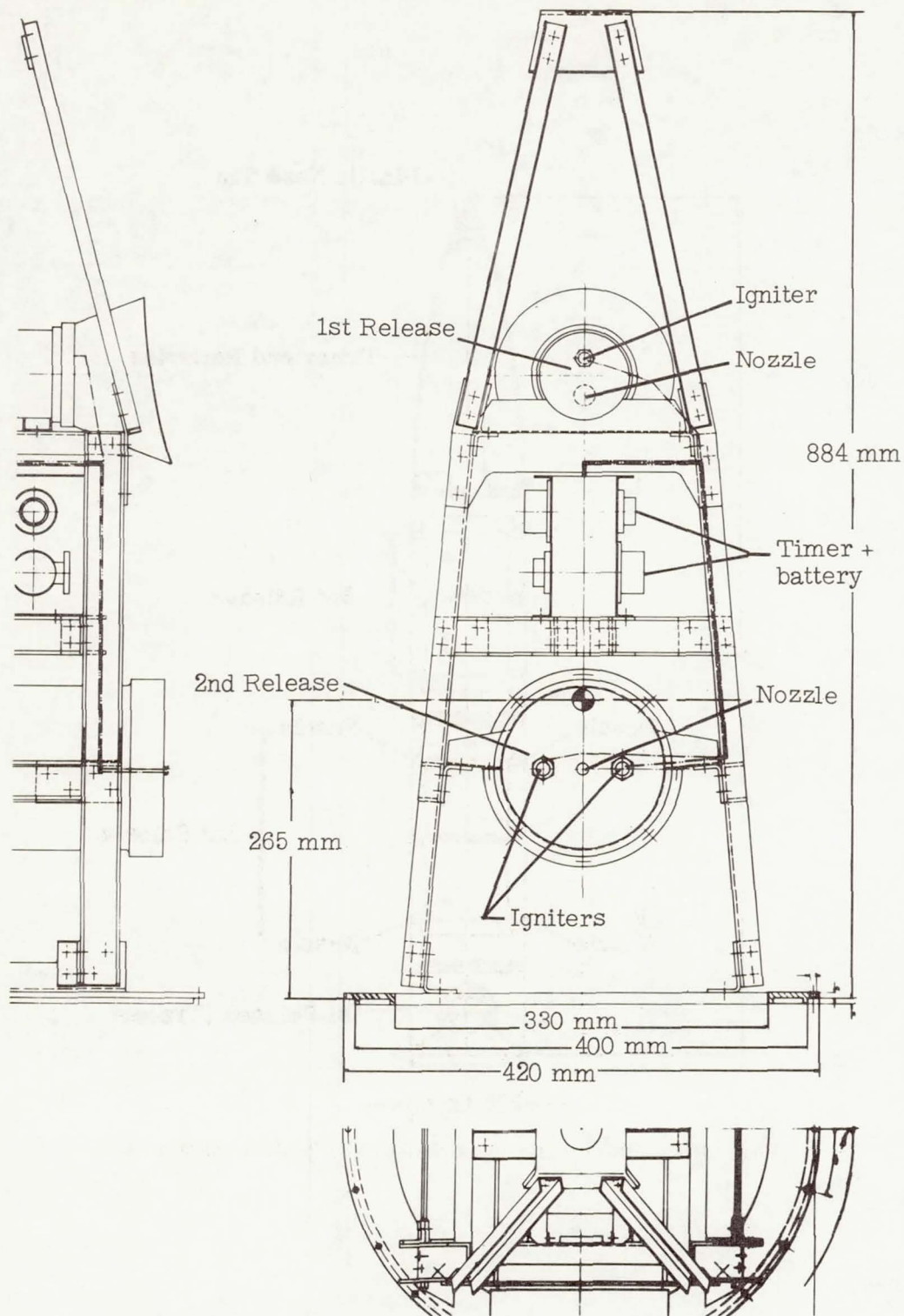
Figure III-1.- Barium-release payload flown on Javelin sounding rocket.
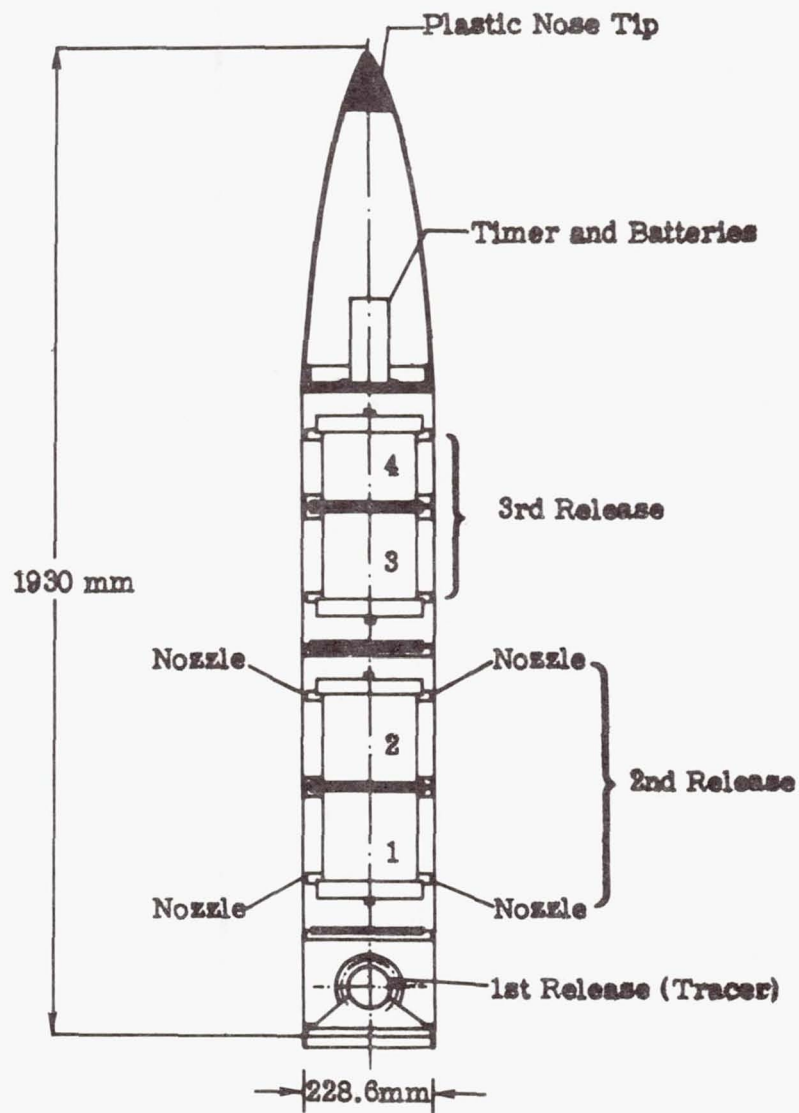
Figure III-2.- Barium-release payload flown on Nike-Tomahawk sounding rocket.

IV. MPI OBSERVATIONAL EQUIPMENT

By B. Meyer and H. Neuss
Institut für extraterrestrische Physik,
Max-Planck-Institut für Physik und Astrophysik

LOCATION AND TYPE OF EQUIPMENT

The Max-Planck-Institute operated two observation sites: the main site at Coquina Beach, North Carolina (35.846^O N, 75.565^O W) and a secondary one at Wallops Island, Virginia (37.867^O N, 75.451^O W) for triangulation in conjunction with the main site. Four types of optical instruments were used: the K-24 aerial cameras, the 35-mm Robot cameras, a spectrograph, and a spectral streak camera. Their distribution was as follows:

Coquina Beach:
   2 K-24 cameras
   1 set of 5 Robot cameras
   1 set of 2 Robot cameras
   1 spectrograph
   1 spectral streak camera

Wallops Island:
   2 K-24 cameras

DESCRIPTION OF OPTICAL EQUIPMENT

Nearly all the instruments described in the following paragraphs performed satisfactorily. It should be mentioned, however, that exposure times for some of the cameras equipped with interference filters were chosen too short to allow a good coverage of the maximum-dilution phase of the high-altitude clouds.

K-24 Cameras

Normal K-24 cameras were used with lenses having a focal length of 178 mm and an aperture of f/2.5. Kodak Wratten filters 45 and 77A were used. Film types were Kodak Tri-X and 2475.

Robot Cameras

The Robot camera was automatically operated with a frame size of 24 by 24 mm. Lenses having focal lengths of 40 and 50 mm and apertures of f/1.9 and f/2, respectively,

13

were used. These cameras were equipped with interference filters which adequately cover the lines of dominant interest and which are listed in the following table:

Filter peak wavelength, Å	Maximum transmission	Width at half maximum, Å
4580	41%	110
4598	61%	46
4934	66%	35
4936	63%	62
5540	60%	11
4556	59%	42

One camera was used without a filter. Kodak 2475 film was used in each of the Robot cameras.

Spectrograph

The dispersion of the grating spectrograph was 190 Å/mm. The camera had an aperture of f/0.75. Registration of the spectrum was photographic. The exposures were programed automatically.

Spectral Streak Camera

This slitless grating spectrograph was a modified K-24 camera with continuous film transport which permitted a monitoring of changes in intensity of spectral lines with a time resolution of 0.1 second.

V. MPI ANALYSIS OF OBSERVATIONS

By G. Haerendel, R. Lüst, and B. Meyer
Institut für extraterrestrische Physik,
Max-Planck-Institut für Physik und Astrophysik

SURVEY OF OBSERVED PHENOMENA

The discussion presented in this section is concentrated on the second release from the Javelin vehicle at an altitude of about 930 km, since this particular experiment exhibited the widest spectrum of fascinating physical and visual phenomena.

The neutral barium vapor in the high-altitude release expanded like a thin, nearly spherical shell. The total brightness of the cloud of neutral barium atoms decreased rapidly because of the photoionization which leads to the creation of the ion cloud. This ion cloud was easily distinguishable from the neutral cloud by its different color and shape. Once formed, it became discernible shortly after release as a narrow cloud elongated along the direction of the magnetic-field line intersecting the point of release. The cloud attained a maximum length of about 1000 km. Particles initially moving upward and subjected to the pull of gravity began to descend after a while, and the cloud began to shrink. Particles piled up in the altitude range from about 300 to 350 km as a result of their being slowed down by collisions with the neutral atmosphere. This is the so-called sedimentation phase during which the cloud's lower extremity grew in brightness and apparent width and its length decreased to about 80 km. While the sedimentation was proceeding, striations parallel to magnetic-field lines were observed to appear within the cloud; at the same time it drifted slowly at right angles to the magnetic field as a result of the influence of the electric field, the measurement of which was one of the essential goals of the ion cloud experiments (ref. V-1).

Symbols used in this analysis are defined in the appendix.

EXPANSION OF THE NEUTRAL CLOUD

As the neutral gas cloud expanded as a nearly spherical shell with a velocity of 1.2 km/sec, its center of mass followed a ballistic path close to the trajectory of the fourth stage of the Javelin vehicle. In figure V-1 a sequence of photographs taken with Robot cameras from Coquina Beach, North Carolina (nearly at right angles to the plane of the trajectory) shows the separation of the neutral cloud from the ionized cloud, the center of which is located on the field line intersecting the point of release.

The expansion of the neutral cloud was collision free after less than 1 sec. The density distribution as a function of time was a simple consequence of the velocity distribution that was established shortly after evaporation in a small volume surrounding the container. To estimate the critical radius r_c at which the transition to collision-free expansion takes place, the radius of the cloud is equated to the mean free path for collisions among the barium atoms. Thus

$$r_c \propto \sigma_{Ba-Ba}\sqrt{N} \qquad (1)$$

where

σ_{Ba-Ba} radius of collisional cross section of neutral barium atoms

N total number of atoms

According to diffusion coefficients derived from barium cloud experiments at lower altitudes (ref. V-2), σ_{Ba-Ba} should be close to 3 Å. (See later discussion on sedimentation of the ions.) With a total number of 10^{24} atoms, r_c is approximately 0.6 km. For the first release, at an altitude of 506.6 km, the transitional radius was one-third of this value.

The shell-like expansion has been observed in several earlier experiments at altitudes above about 350 km. The most distant ones were Soviet sodium releases at distances of more than 100 000 km (ref. V-3). The expansion is not always as nearly spherically symmetric as it was in the upper Javelin release. The lower release, for instance, was much more irregular. This difference seems to be quite plausible since the establishment of spherical symmetry certainly requires a sufficiently long-lasting collision-dominated expansion period r_c/v_o as compared with the time necessary for ejection of the gas from the container which usually varies between 0.1 and 0.2 sec.

In order to describe the velocity distribution with the minimum set of parameters, the following spherically symmetric velocity distribution function is adopted:

$$f(v) \propto v^2 \exp\left[-\left(\frac{v - v_o}{v_t}\right)^2\right] \qquad (2)$$

where

v_o average value of radial velocity of particles

v_t mean thermal velocity of particles

16

The particles between r and $r + dr$ at $t \gg \frac{r_c}{v_o}$ are those having initial velocities in the range $\frac{r}{t}$ to $\frac{r + dr}{t}$. Thus, the number of particles in the annular shell is proportional to

$$\frac{r^2}{t^2} \exp\left[-\left(\frac{\frac{r}{t} - v_o}{v_t}\right)^2\right]\frac{dr}{t}$$

The particle density is obtained by dividing by $4\pi r^2 dr$. Thus

$$n(r,t) \propto t^{-3} \exp\left[-\eta^2\left(\frac{r}{v_o t} - 1\right)^2\right] \tag{3}$$

where

$$\eta = \frac{v_o}{v_t} \cdot$$

As η is independent of time, the relative density and brightness distributions should remain invariant, only the length scale increases as $v_o t$, and the total number of neutral atoms decreases steadily because of photoionization.

The surface brightness is determined by the integral of $n(r,t)$ along the line of sight at a distance a from the cloud center; thus

$$\tilde{N}(a,\eta,t) = \int_{-\infty}^{+\infty} n\left(\sqrt{a^2 + y^2}, \eta, t\right) dy \tag{4}$$

The ratio of the maximum brightness (corresponding to line of sight through the densest part of the annular shell) to the brightness at the cloud center $\tilde{N}_{max}/\tilde{N}_{center}$ is solely a function of η. This function is plotted in figure V-2. The same plot contains the radius of maximum brightness measured in units of $v_o t$. For large values of η (very narrow velocity distribution around v_o) this radius approaches unity.

Figure V-3 shows a densitometer trace taken parallel to the magnetic-field line along which the ion cloud elongates. The trace is through the center of the photographic image (fourth in sequence in figure V-1) of the neutral cloud 21 sec after release. The spherical symmetry is far from perfect, as is quite apparent from the shape of the trace. The relative width of the velocity distribution varies appreciably. The upper portion shows higher values than the lower one. Figure V-4 has been obtained from figure V-3 by converting from photographic density to cloud brightness expressed in relative units,

at the same time doing some statistical smoothing. The ratio $\tilde{N}_{max}/\tilde{N}_{center}$ has been measured from 15 frames taken between 15 and 31 sec after release, and the results plotted in figure V-5. The average value of $\tilde{N}_{max}/\tilde{N}_{center}$ over the time interval is 2.9 for the upper portion and 2.2 for the lower portion of the cloud; in figure V-2, these values correspond to $\eta = 11$ and $\eta = 6$, respectively. This means that the dispersion of velocities is only on the order of 10 to 15 percent of the bulk velocity.

Interpretation of the shell-like expansion starts with noting that the kinetic energy of the expanding barium gas is much higher than the internal energy of the gas during evaporation. The measured expansion velocity of 1.2 km/sec, if randomized, corresponds to a temperature of 12 000° K, whereas the temperature inside the container after the reaction is completed is only 2300° K. This difference in temperature means that the gas must have been accelerated after leaving the container. According to the theory of reference V-4, this acceleration is a consequence of the heat flow from the hot droplets consisting of BaO, Ba, and Cu to the faster expanding Ba gas. More than 95 percent of the chemical energy released in the reaction is stored as internal energy of the condensed matter. Part of this energy is used for counteracting the cooling of the expanding gas. Hence, the kinetic energy increases steadily and particles that were initially at the lower end of the Maxwellian distribution interact longer with the condensed matter and are thereby accelerated. This is a very rough description of the origin of the observed density distribution.

IONIZATION AND YIELD

Neutral cloud brightness diminished very rapidly because of the increasing size of the cloud and the loss of neutral atoms by photoionization. After only 1 minute the ion cloud was dominant in brightness. The photoionization time scale is surprisingly short. The important role that the intermediate population of the metastable $^1D_2$ and $^3D_{1,2,3}$ states is playing is discussed in reference V-5. The observed time scale is explained in a theoretical investigation (ref. V-6).

A measure of the total luminosity of the ring-shaped cloud can be obtained from the product of the central brightness and the cloud diameter squared. From one of the photographs (obtained from camera with f/1.9 optics without filter) the points plotted in figure V-6 were obtained. Because of malfunctioning of the camera, the coverage was not complete. In addition, calibration of the film was not very reliable. Therefore, the observed exponential decay time of 19 sec must be regarded as only approximate although the value agrees roughly with other measurements made by MPI.

During the first 15 sec of the neutral cloud expansion an increase in brightness at 5535 Å was noted; thereafter the luminosity at this wavelength fell off exponentially.

From this it is inferred that the neutral cloud became optically thin 15 sec after release. This permitted an upper limit for the total number of atoms to be arrived at as follows.

The resonant spectral line is approximated by a rectangle (shown by dash lines in the following sketch) of width γ equal to the width in radians/sec at half-intensity of the actual spectral line.
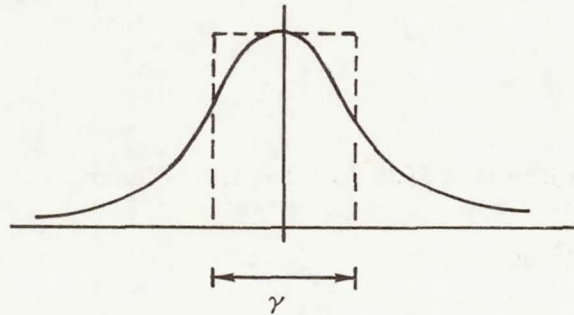
The absorption coefficient per unit volume κ is assumed to be constant over the line width and equal to that at the center of the line in question, that is

$$\kappa = 4\pi \, \frac{e^2}{\gamma m_e c} \, fn$$

where

e   electronic charge

m_e mass of electron

c   velocity of light

f   oscillator strength

n   particle density

Because of Doppler shift the line profiles for absorption and emission of the resonance line ($\lambda = 5535$ Å) overlap only for those particles having a velocity spread of $\lambda \frac{\gamma}{2\pi}$.

The notion of optical thickness is somewhat different from the conventional one in that in this case, at a given time, the distance of a particle from the center is a direct measure of its velocity. Hence, thickness of the layer in which there is absorption of the 5535 Å line is given by

$$s = \lambda \frac{\gamma}{2\pi} t$$

Optical thickness is expressed

$$\tau = \kappa s$$

$$= \frac{2e^2}{m_e c} f\lambda nt \tag{5}$$

For the resonance line $(\lambda = 5535 \text{ Å})$, $f = 1.4$. Hence

$$\tau = 1.3 \times 10^{-6} nt \tag{6}$$

The maximum density in the shell derived from the density distribution (eq. (3)) is

$$n_{max} \approx \frac{\eta N(t)}{4\pi^{3/2} v_0^3 t^3} \tag{7}$$

By setting $t = 15$ sec, $\eta = 8$, and $v_0 = 1.2 \times 10^5$ cm/sec, and making use of equations (6) and (7), the upper limit for the total number of neutral barium atoms after 15 sec can be derived from $\tau \lesssim 1$ as being

$$N(15 \text{ sec}) \lesssim 8.4 \times 10^{23}$$

With an assumed effective photoionization time of 20 sec and taking into account the loss of neutral atoms by photoionization during the first 15 sec, the total number of atoms released is

$$N(0) \lesssim 1.8 \times 10^{24}$$

Therefore, the yield was less than 410 g, or the overall efficiency of the Ba-CuO mixture was less than 4 percent.

Another estimate of the yield can be made from the absolute values of the brightness by using the sensitivity of the Kodak 2475 film. After 31 sec, with an exposure time of 0.5 sec and f/1.9 optics, a cloud image was obtained with a maximum density in the shell of 0.2 above gross fog for which an exposure of 1.2×10^{-3} meter-candle-sec is needed; this leads to $N(31 \text{ sec}) \approx 2.3 \times 10^{23}$ or $N(0) \approx 10^{24}$ atoms, corresponding to a yield of about 2 percent.

CHARACTERISTICS OF THE ION CLOUD

Generation of the Ion Cloud

The total rate of production of ions from the expanding neutral gas cloud is proportional to the mass of neutral gas and the rate of ionization. The ions are trapped immediately. Since the neutral density is decreasing as $t^{-3} \exp\left(-\dfrac{t}{19 \text{ sec}}\right)$ and the neutral cloud is moving, in addition, along its ballistic trajectory, the ion cloud is strongly concentrated at field lines which pass close to the point of release (see fig. V-1). This concentration is due mainly to the geometric expansion of the neutral atoms. The exponential decrease of the total number of neutral atoms determines only the cut-off at the edges of the ion cloud. The resulting apparent width of the ion cloud was about 40 km.

The component of the neutral gas velocity transverse to the magnetic field is lost very quickly by momentum transfer to the ionospheric plasma distributed along the same magnetic-flux tube via an electric polarization field E_p. This field propagates with Alfvén velocity along the field lines, and in less than a second it has reached the E-layer of the ionosphere. Here, the electric field will drive a Pedersen current whose ohmic losses provide the ultimate sink of momentum.

The force acting on the ions is

$$\rho \frac{dv}{dt} = \frac{1}{c} j_D B \tag{8}$$

where

ρ mass density of cloud

j_D density of polarization current associated with cloud deceleration

B magnetic-field strength

Integrating along the field lines, the estimated total polarization current I_D is given by

$$I_D = \frac{c}{B} \frac{m_{Ba} N}{\pi R^2} \left| \frac{dv}{dt} \right| \tag{9}$$

where

m_{Ba} mass of barium ion

R effective radius of ion cloud

21

If the propagation of the electric field into the lower ionosphere is neglected, the polarization current is closed by a conduction current I_c in the E-layer of the ionosphere, determined by both the height-integrated Pedersen conductivity Σ_P and the electric polarization field $|E_p| = \frac{v}{c} B$. By equating I_c and I_D (see ref. V-7), the time scale of momentum transfer t_D is found to be

$$t_D = \frac{v}{\left|\frac{dv}{dt}\right|} = \frac{m_{Ba} c^2 N}{B^2 \pi R^2 \Sigma_P} \tag{10}$$

With $R = 20$ km, $B = 0.4$ gauss, $\Sigma_P = 1 \ \Omega^{-1} \hat{=} \ 9 \times 10^{11}$ electrostatic units, and $N = 10^{24}$ atoms, deceleration time t_D is approximately 0.1 sec.

This time scale is of the same magnitude as the time necessary for propagating the electric polarization field into the lower ionosphere. During the first few seconds, when R is an order of magnitude smaller and N is less than 10^{24}, t_D is of the order of 1 sec. Still an observable displacement of the ion cloud due to polarization is not expected, since only displacements of the order of 10 km are detectable. This is in agreement with the most accurate triangulation data on the releases reported herein.

Another steady source of polarization is provided by gravity acting on the ions. The density of the polarization current j_g is given by

$$j_g = nec \ \frac{m_{Ba} g \cos \theta}{eB}$$

where

g   acceleration due to gravity

θ inclination of magnetic-field line with respect to local horizontal

The total gravity-induced polarization current I_g is expressed

$$I_g = \frac{m_{Ba} N c g \cos \theta}{\pi R^2 B}$$

Equating I_g and the conduction current I_c (which is the product of Σ_P and E_p) yields an estimate of the drift velocity transverse to $\vec{B}$ as

22

$$v_g \approx \frac{m_{Ba} c^2 Ng \cos \theta}{B^2 \pi R^2 \Sigma_P} \tag{11}$$

With $\theta = 67^{\circ}$ and the values previously indicated for the other parameters, $v_g = 44$ cm-sec^{-1}. This velocity is unobservably small.

Thus, it is concluded that the ions are trapped on the lines of force where they originate and that any motions transverse to $\vec{B}$ have to be attributed to an external electric field or, after sedimentation to lower levels, to an interaction with the neutral atmosphere.

Mapping of the Magnetic Field

The ion cloud spreads along the magnetic field while the center of mass is falling toward the earth (see fig. V-7). As expected, the length is growing with about the same speed as the diameter of the neutral cloud (see fig. V-1). However, there is a significant high-velocity tail in the initial distribution of the ions. On the most sensitive recordings (from a television camera) the upper end of the cloud was located at an altitude of 1150 km after 750 sec when the majority of the ions had already fallen to altitudes below 400 km. This would be possible only if the initial velocity component parallel to $\vec{B}$ of those ions comprising the high-velocity tail was 2.8 km/sec, a velocity corresponding to a kinetic energy of 5.8 eV, or an excess of 4.7 eV over the kinetic energy of the average neutral atom ($v_O = 1.2$ km/sec).

Although it is possible that such high velocities were produced in the initial expansion, the observed density distribution of the neutral cloud, which was well fitted at its bright parts by equation (3), leads to extremely low predictions for the number of particles having a velocity of 2.8 km/sec. Therefore, it may be speculated that the high-velocity tail of the ion distribution was a result of the energy fed into the plasma cloud by the photoelectrons. Most of the ionization was apparently achieved from the metastable states by solar ultraviolet radiation of less than 3300 Å. However, a significant portion of the ionizing photons had more than the minimum energy. Therefore, the electron gas which neutralized the ion cloud is expected to have a rather high pressure. As the ions are coupled to the electrons via electric polarization fields, they can be accelerated. Since collisions are already rare, a broad high-energy tail of the ion distribution would be expected.

The ion cloud reached its maximum extension after about 400 sec. At this time the altitude-latitude and altitude-longitude distributions were as plotted in figures V-8 and V-9, respectively. Since the observation sites were located along the Atlantic coast, more or less parallel to the magnetic meridian planes, errors in declination are much

23

higher than the errors in inclination. The average magnetic declination over the segment of field line illuminated by the cloud and derived by triangulation from the most widely separated sites, Coquina Beach and Wallops Island, was $9.2^O \pm 2.3^O$ W. The value from spherical harmonic expansion of the geomagnetic field by the method of reference V-8 is 11°. The magnetic inclination θ is a function of latitude. Inclinations obtained from triangulation of the ion cloud at different altitudes are compared with a theoretical prediction (computed by use of ref. V-8) in figure V-10.

On the whole, agreement of the measured position of the ion cloud with the theoretical field lines is quite reasonable. However, the triangulation of the ion cloud is by far too imprecise to provide a means of checking critically the field models based on surface data.

Sedimentation of the Ions

When the ions fell below 500 km, collisions with the neutral component of the atmosphere, predominantly with oxygen atoms, became significant. At about 350 km the ions were in thermal equilibrium with the atmosphere. The subsequent decrease in altitude was a sedimentation process. The length of the ion cloud was determined by the time difference between those particles arriving earliest and latest and the atmospheric scale height. The observed length was approximately 100 km when the cloud's center was below 300 km.

In order to calculate the slowing down and sedimentation, the particles have been treated from the point of view of the Langevin equation without considering the stochastic forces. Only the component of gravity g along the field lines and an average frictional force, expressed by a collision frequency ν_{in} which is a function of velocity and height, have been included to give

$$\frac{dV_{||}}{dt} = g(h) \sin \theta - \nu_{in}(v,h)v \tag{12}$$

If the index 1 designates the atmospheric particles and index 2 designates the particles under consideration, ν_{in} can be approximated by the method of reference V-2 as

$$\nu_{in} = \frac{m_1}{m_1 + m_2} \pi \sigma^2 n_1(h) \phi(v) \tag{13}$$

where

m_1 mass of atmospheric particles

m_2 mass of ionized particles

24

$\pi\sigma^2$ collisional cross section (σ is radius of total collisional cross section)

$n_1(h)$ number density of atmospheric particles

$$\phi(v) = v_c \qquad (v < v_c)$$

$$\phi(v) = v \qquad (v > v_c)$$

with the characteristic velocity given as

$$v_c = \sqrt{\frac{128kT_1}{9\pi m_1}} \tag{14}$$

and

k   Boltzmann constant

T_1 ambient absolute temperature

From the diffusion of barium clouds below 230 km, it has been shown in reference V-2 that $\sigma = 4.6$ Å of which about 3 Å are attributable to the radius of the rather large barium atom. The cross section of the barium ion should be only slightly smaller.

The solid curve in figure V-7 shows the theoretical variation with time of the altitude of the average particle, starting with zero velocity at an altitude of 930 km in an atmosphere where $\nu_{in} = 2.26 \times 10^{11} h^{-5}$ where h is in km. This choice of ν_{in} provides the best fit to the data points. Figure V-11 presents a comparison of this distribution with the values of ν_{in} derived from atmospheric model 6 of reference V-9 for 0900 hours, which seems to apply best to the conditions of the experiment. For the interaction of Ba^+ and atomic oxygen, $\sigma = 4.0$ Å was assumed; and for Ba^+ and molecular nitrogen, $\sigma = 4.6$ Å was assumed. The two curves are rather close. The theoretical atmospheric density, however, seems to be on the low side at altitudes above 250 km.

More precise statements are possible only if the diffusion is included in the treatment of particle motion; however, it is quite apparent that experiments such as this one provide a sensitive means of deriving the atmospheric density profile above 200 km. In an earlier release (ref. V-10) at an altitude of 2000 km over the Sahara, similar data were obtained. Unfortunately, most of the sedimentation phase was missed, since the experiment was carried out at sunset when the shadow limit was rising above 300 km.

25

Electric Fields

After the high-altitude cloud settled to levels below 300 km, it was readily observable for another 20 minutes. During this period a westerly drift of the cloud transverse to the magnetic field, with a small northerly component, was easily discernible. The cloud then appeared striated in the direction of $\vec{B}$ as is quite common to all the low-altitude ion clouds. On some films the striations give the impression that the cloud had relatively sharp edges transverse to $\vec{B}$. The locations of the apparent northern and southern edges at the 250-km level are plotted in figure V-12. The relatively high scatter of the data results from the great distance of the cloud from the observer relative to the short triangulation baseline. The motion corresponds to a mean transverse velocity of 23.1 m/sec or a nearly northward directed transverse electric field of 1.26 mV/m as shown in the following sketch:

N

E

$\vec{V}_\perp$

$\vec{E}_\perp$

1.26 mV/m

23.1 m/sec

Plane perpendicular to $\vec{B}$
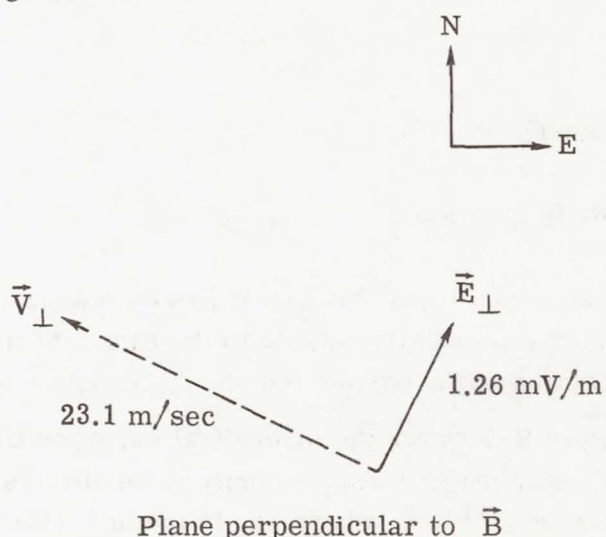
One day later, in the experiment with the Nike-Tomahawk, the transverse drifts of the three ion clouds were of the same magnitude (about 25 m/sec), but the direction was nearly southerly with a small westerly component, corresponding to a nearly westward directed electric field.

These results are in good agreement with those from other midlatitude experiments (see ref. V-11) in that, during sunrise, the direction of $\vec{E}_\perp$ is overwhelmingly in the northwest sector and its magnitude is of the order of a few mV/m. If the average quiet-day current system were driven by an electric field, its direction during morning hours at these latitudes should be confined to the southeast sector, clearly opposite to the observations. This result was interpreted as an indication that the ionospheric current at these locations is driven by the dynamo field in the E-layer and that the observed $\vec{E}_\perp$ is an electric polarization field due to the finite resistance of the ionospheric current circuit (refs. V-11 and V-12).

The fact that the striations of the ion cloud appeared only after its lower end had reached altitudes well below 300 km is quite consistent with an interpretation of the striations given in reference V-13 as being caused by a density-gradient instability which is driven by electric polarization fields generated by the flow of the Pedersen current. If the cause for the striations is to be sought in the existence of the ion cloud, they would be expected to appear only if a considerable fraction of the ions has reached levels where the transverse mobility of the ions is no longer negligible. Below 300 km the striations have appeared in virtually all experiments where the brightness of the clouds was sufficiently high. Because of the high conductivity parallel to $\vec{B}$, the striations have considerable extension toward greater altitudes. Therefore, sufficient conditions exist for the appearance of the instability in the lower part of the cloud. The upper part has to follow rigidly.

Determination of the inclination of the striations gave values close to 69° which is what would be expected from figure V-10. The value of the declination deviated appreciably from the theoretical value because of the large triangulation errors.

27

APPENDIX

SYMBOLS

a   distance from neutral cloud center to line of sight

$\vec{B}$ magnetic-field vector

c   velocity of light

$\vec{E}$ electric-field vector

E_p electric polarization field within cloud

e   electronic charge

f   oscillator strength

f(v)   velocity distribution function

g   acceleration due to gravity

h   altitude

I_c conduction current in ionospheric E-layer

I_D total polarization current associated with cloud deceleration

I_g total polarization current associated with gravity

j_D density of polarization current associated with cloud deceleration

j_g density of polarization current associated with gravity

k   Boltzmann constant

m_{Ba} mass of barium ion

m_e mass of electron

28

APPENDIX

N   total number of particles within cloud

$\tilde{N}$ number of particles per unit area along line of sight

n   particle density within cloud

R   effective radius of ion cloud

r   distance from neutral cloud center

r_c radius of neutral cloud corresponding to transition to free collisionless expansion

s   maximum particle separation for spectral-line overlap

t   time subsequent to release

t_D time to decelerate

$V_{||}$ velocity component of cloud parallel to field lines

$V_{\perp}$ transverse drift of cloud

v   particle velocity

v_c characteristic particle velocity involved in expression for particle collisions (eq. (14))

v_g transverse drift velocity of cloud due to pull of gravity

v_0 mean radial expansion velocity of neutral cloud

v_t mean thermal velocity of particles

γ natural spectral-line width

η parameter appearing in velocity distribution function

θ inclination of magnetic-field line with respect to local horizontal

APPENDIX

κ	absorption coefficient per unit volume
λ	wavelength
ν_{in}	collision frequency between ions and neutrals
ρ	mass density of cloud
Σ_P	height-integrated Pedersen conductivity
σ_{A-B}	radius of collisional cross section between species A and B
τ	optical thickness

REFERENCES

V-1. Haerendel, G.; Lüst, R.; and Rieger, E.: Motion of Artificial Ion Clouds in the Upper Atmosphere. Planetary Space Sci., vol. 15, no. 1, Jan. 1967, pp. 1-18.

V-2. Rösler, Gernot: Diffusion künstlicher Metalldampfwolken in der oberen Atmosphäre. Thesis, Univ. of Munich, 1968.

V-3. Shklovskii, I. S.: An Artificial Comet as a Method for Optical Tracking of Cosmic Rockets. Artificial Earth Satellites, Vol. 4, L. V. Kurnosova, ed., Plenum Press, Inc., 1961, pp. 445-465.

V-4. Smilga, W.: Zur Expansion künstlicher, neutraler Metalldampfwolken in der Hochatmosphäre. Z. Naturforsch., Bd. 23a, Heft 3, Mar. 1968, pp. 417-423.

V-5. Haser, L.: Use of Artificial Barium Clouds to Study Magnetic and Electric Fields in the Atmosphere. Aurora and Airglow, Billy M. McCormac, ed., Reinhold Pub. Corp., c.1967, pp. 391-403.

V-6. Drapatz, S.: Untersuchung der Spektren von Metalldampfwolken in der Hochatmosphäre. MPI-PAE/Extraterr. 13/67, Max-Planck-Institut Phys. Astrophys., Nov. 1967.

V-7. Zinn, John; Hoerlin, Herman; and Petschek, Albert G.: The Motion of Bomb Debris Following the Starfish Test. Radiation Trapped in the Earth's Magnetic Field, Billy M. McCormac, ed., Gordon & Breach, Science Publ., Inc., 1966, pp. 671-692.

V-8. Cain, Joseph C.; Hendricks, Shirley; Daniels, Walter E.; and Jensen, Duane C.: Computation of the Main Geomagnetic Field From Spherical Harmonic Expansions. Data Users' Note NSSDC 68-11, NASA Goddard Space Flight Center, May 1968, pp. 41-42.

V-9. COSPAR Working Group IV, compilers: CIRA 1965. North-Holland Pub. Co. (Amsterdam), 1965.

V-10. Rieger, E.; Neuss, H.; Lüst, R.; Meyer, B.; Haser, L.; Loidl, H.; Stöcker, J.; and Haerendel, G.: High Altitude Releases of Barium Vapour Using a Rubis Rocket. Ann. Géophys., vol. 26, no. 4, 1970, pp. 845-852.

V-11. Haerendel, G.; and Lüst, R.: Electric Fields in the Upper Atmosphere. Earth's Particles and Fields, Billy M. McCormac, ed., Reinhold Book Corp., c.1968, pp. 271-285.

V-12. Haerendel, G.; Lüst, R.; and Rieger, E.: Ionospheric Electric Fields at Midlatitudes During Twilight. Trans., Amer. Geophys. Union (Geomagn. Aeronomy Abstr.), vol. 48, no. 1, Mar. 1967, pp. 66-67.

V-13. Völk, Heinrich J.; and Haerendel, Gerhard: Striations in Ionospheric Ion Clouds —
        Part I.   MPI-PAE/Extraterr. 50, Max-Planck-Institut Phys. Astrophys., Aug.
        1970.

100 km
⊢———————⊣
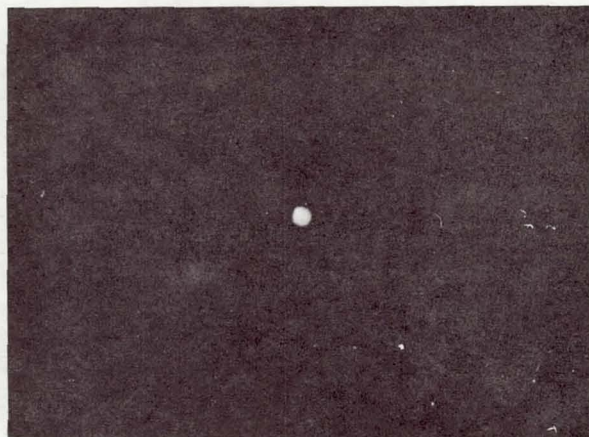
t = 3 sec

Δt = 2 sec

Filter at 5540 Å

t = time after
release, sec

Δt = exposure
duration, sec
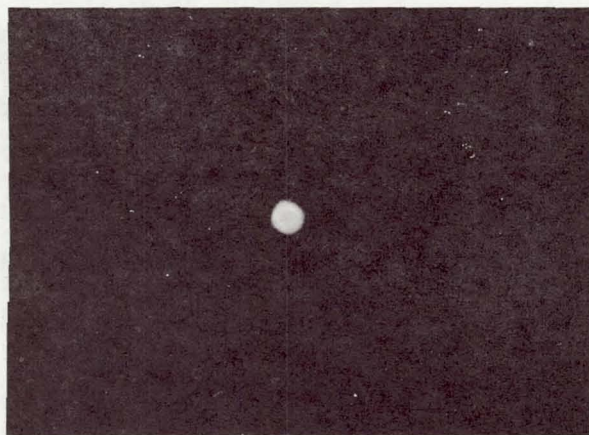
t = 6.5 sec

Δt = 3 sec

Filter at 5540 Å

t = 10.5 sec

Δt = 3 sec

Filter at 5540 Å

Figure V-1.- Photographs of cloud evolution taken with Robot cameras at Coquina Beach, North Carolina.

33
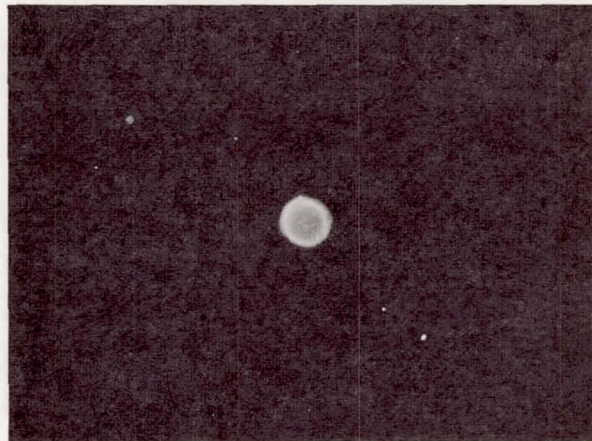
100 km

t = 21 sec
Δt = 0.5 sec

Without filter

t = time after
    release, sec

Δt = exposure
    duration, sec
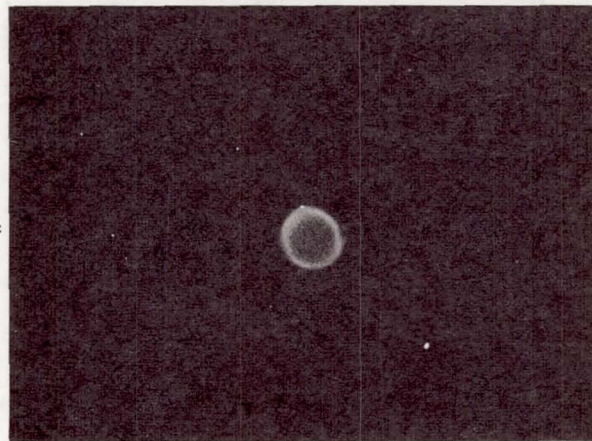
t = 27 sec
Δt = 0.5 sec
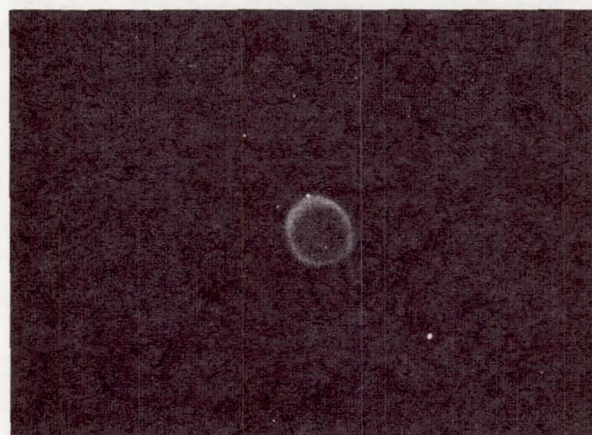
Without filter

t = 31 sec
Δt = 0.5 sec

Without filter

Figure V-1.- Continued.

34

t = 75 sec
Δt = 27 sec

Filter at 4580 Å

t = time after
    release, sec

Δt = exposure
     duration, sec

t = 112 sec
Δt = 8 sec

Without filter

t = 162 sec
Δt = 8 sec

Without filter

Figure V-1.- Concluded.
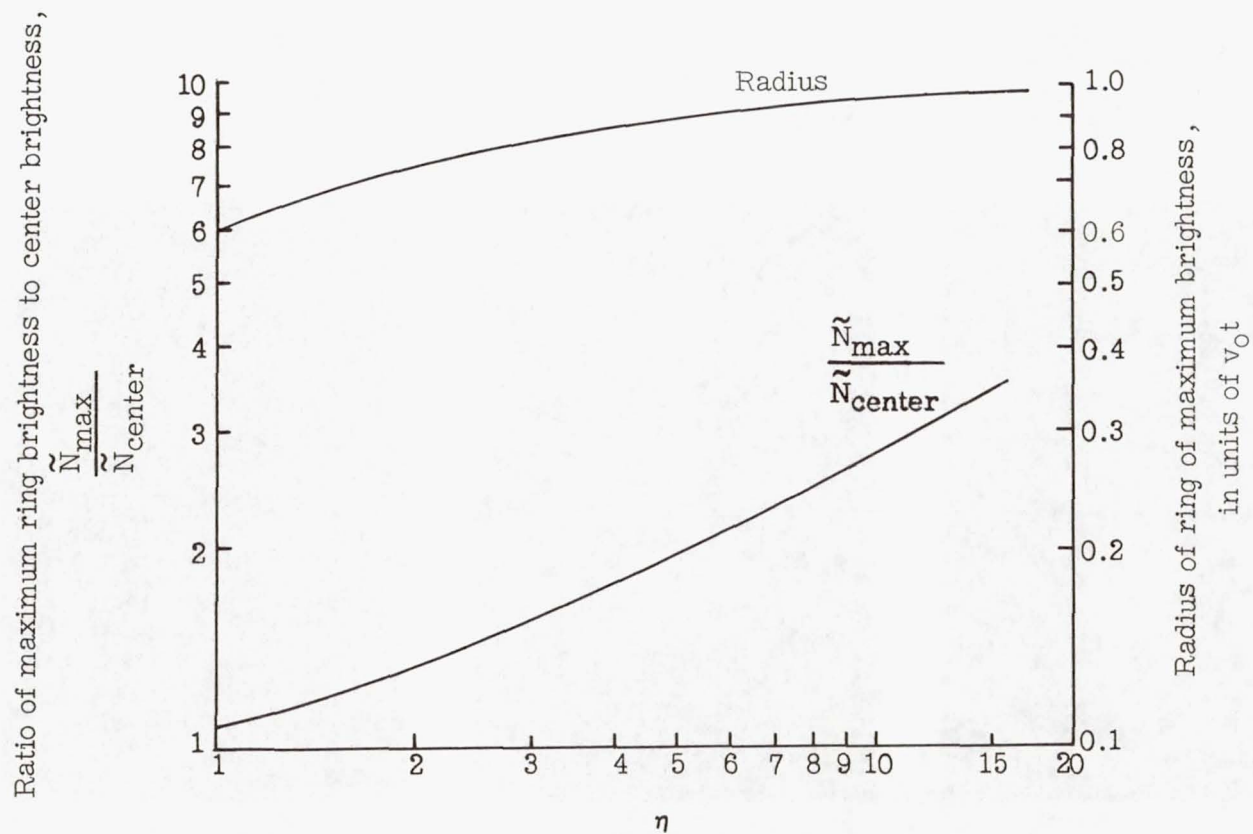
Figure V-2.- Brightness distribution of neutral barium cloud.

36
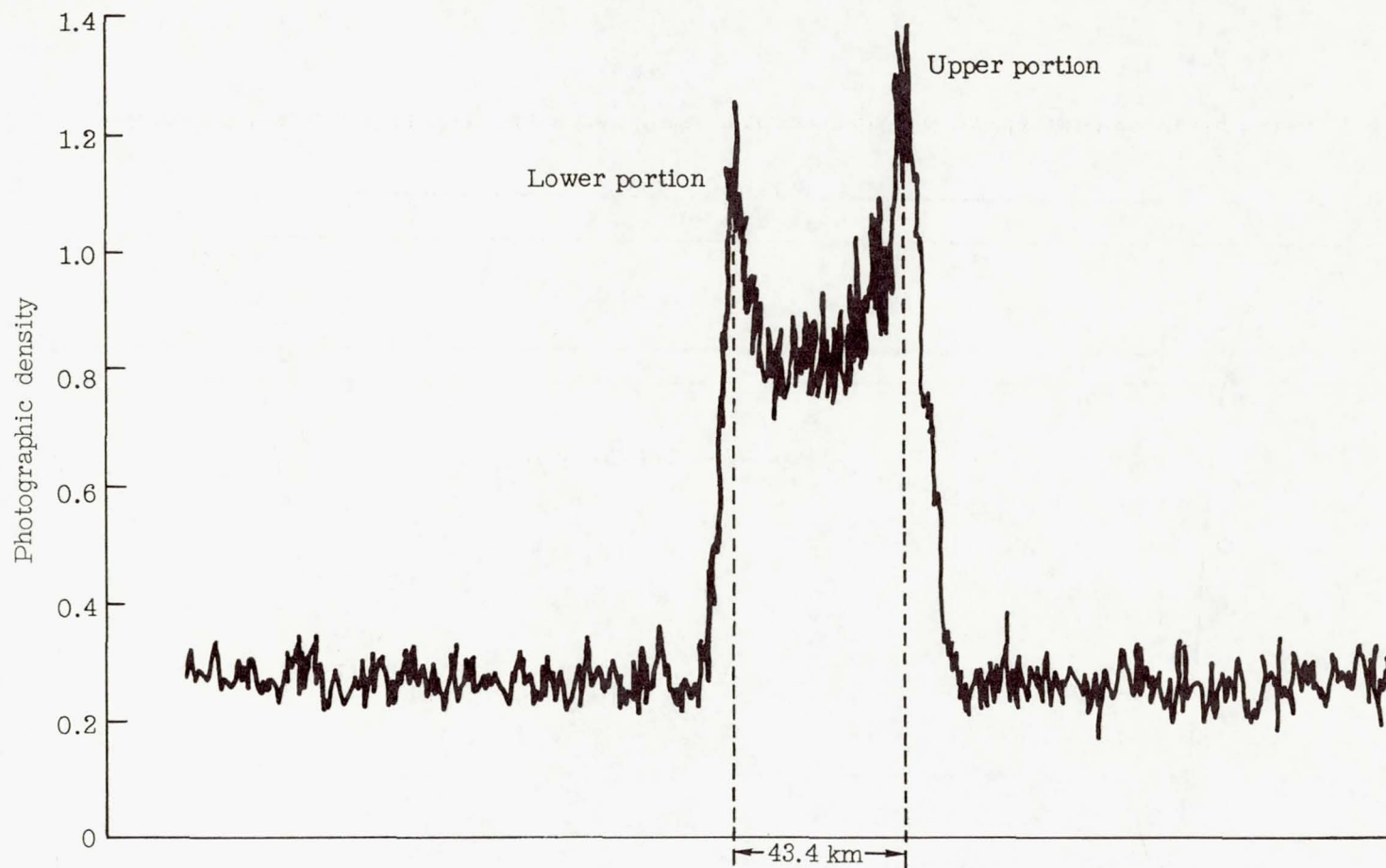
Figure V-3.- Densitometer trace of photographic image of neutral cloud. (Fourth photograph in sequence shown in fig. V-1, 21 seconds after release.)
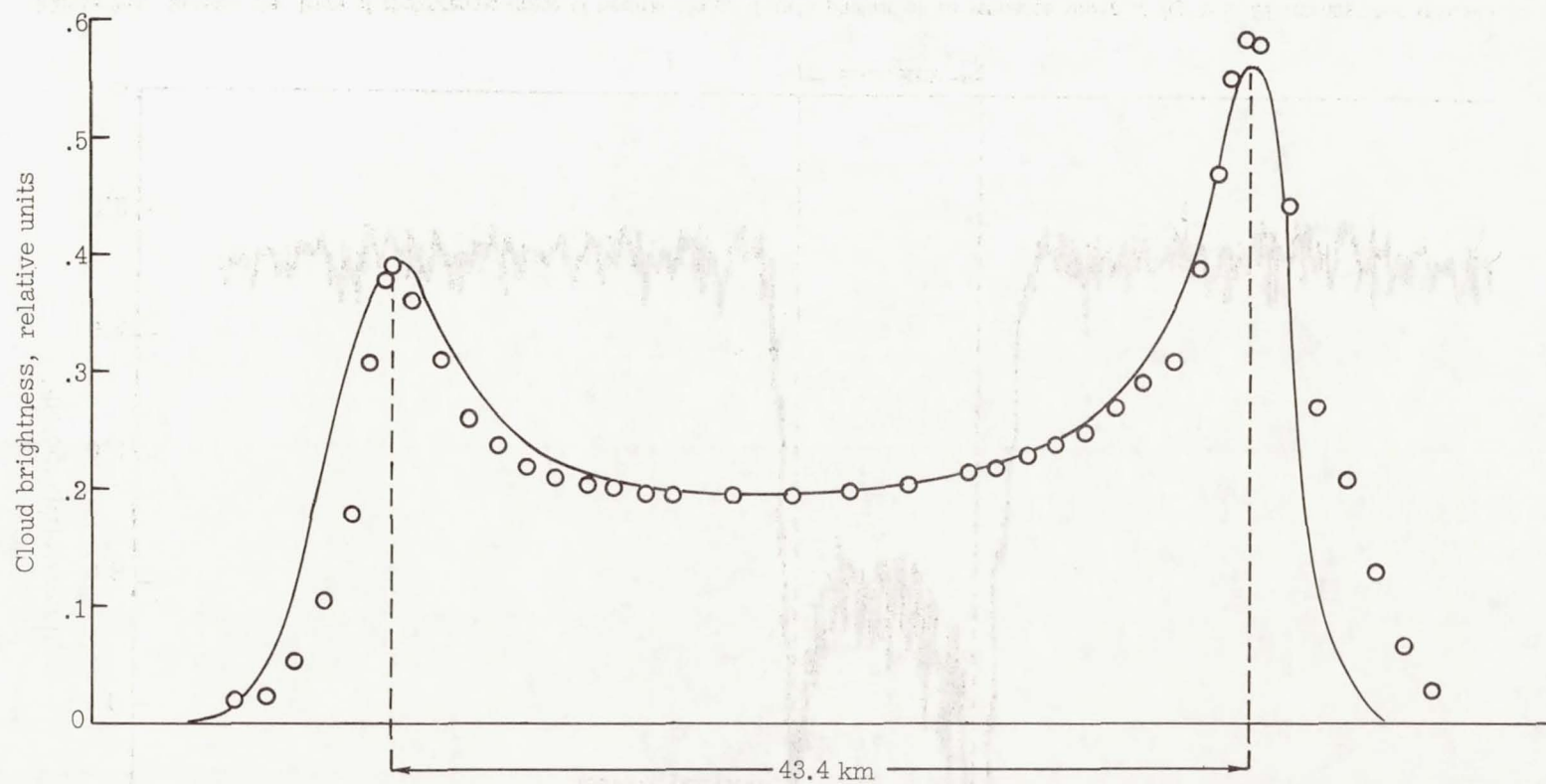
Figure V-4.- Comparison of theoretical and experimental radial brightness distribution of neutral cloud (21 seconds after release).
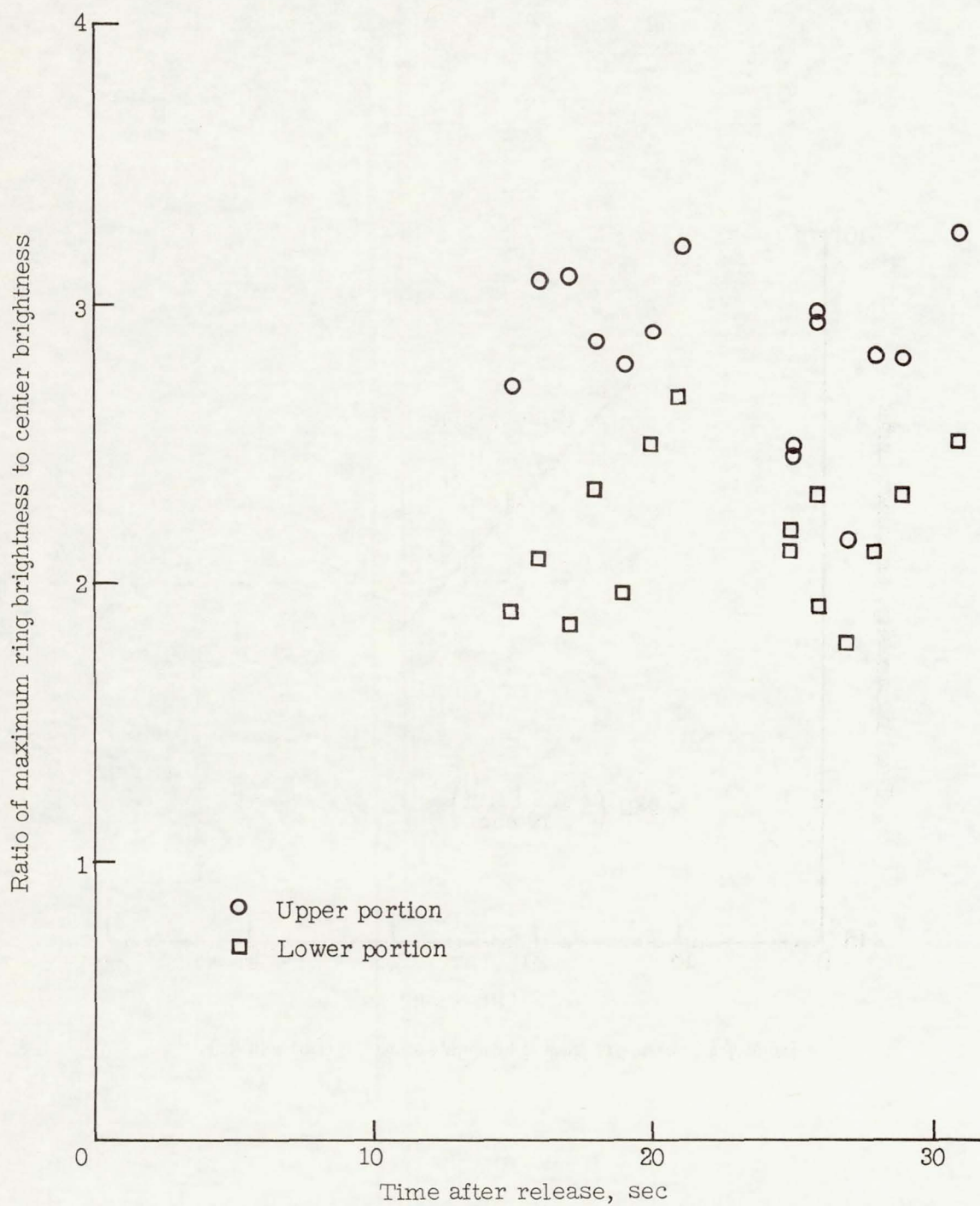
Figure V-5.- Measured value of ratio of maximum ring brightness to center brightness as function of time.
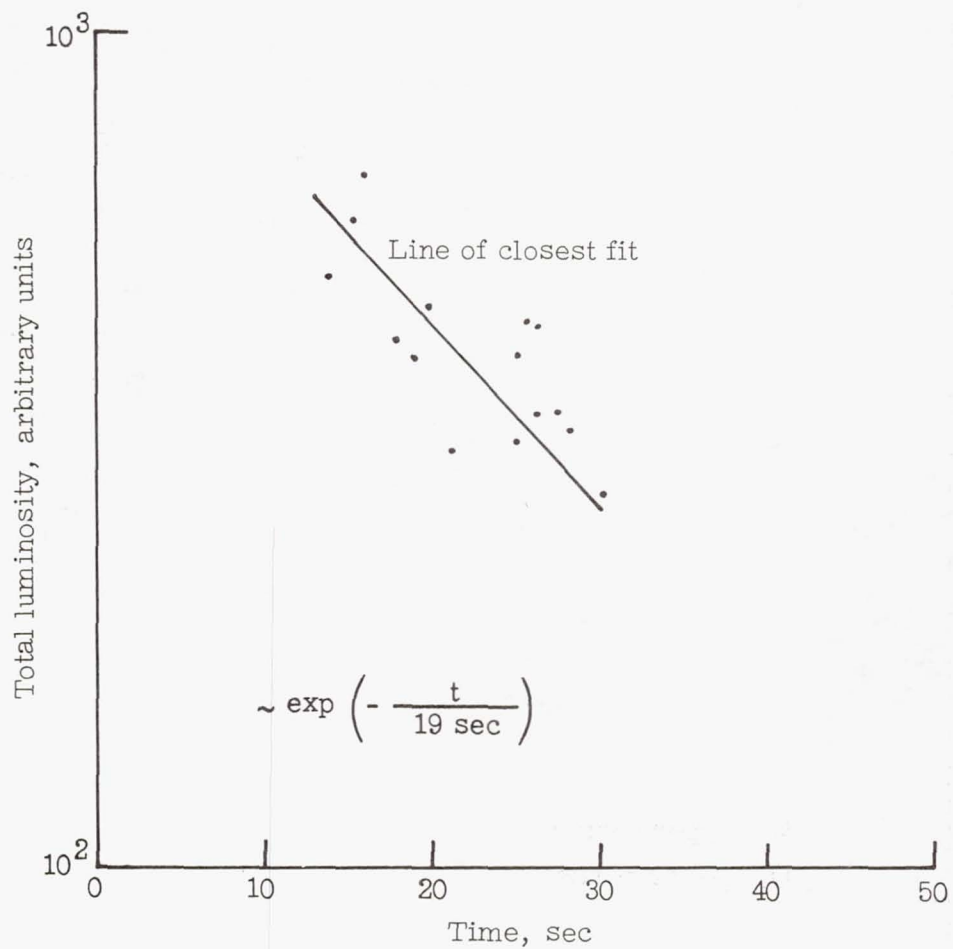
Figure V-6.- Measure of decay of luminosity of neutral cloud with time.
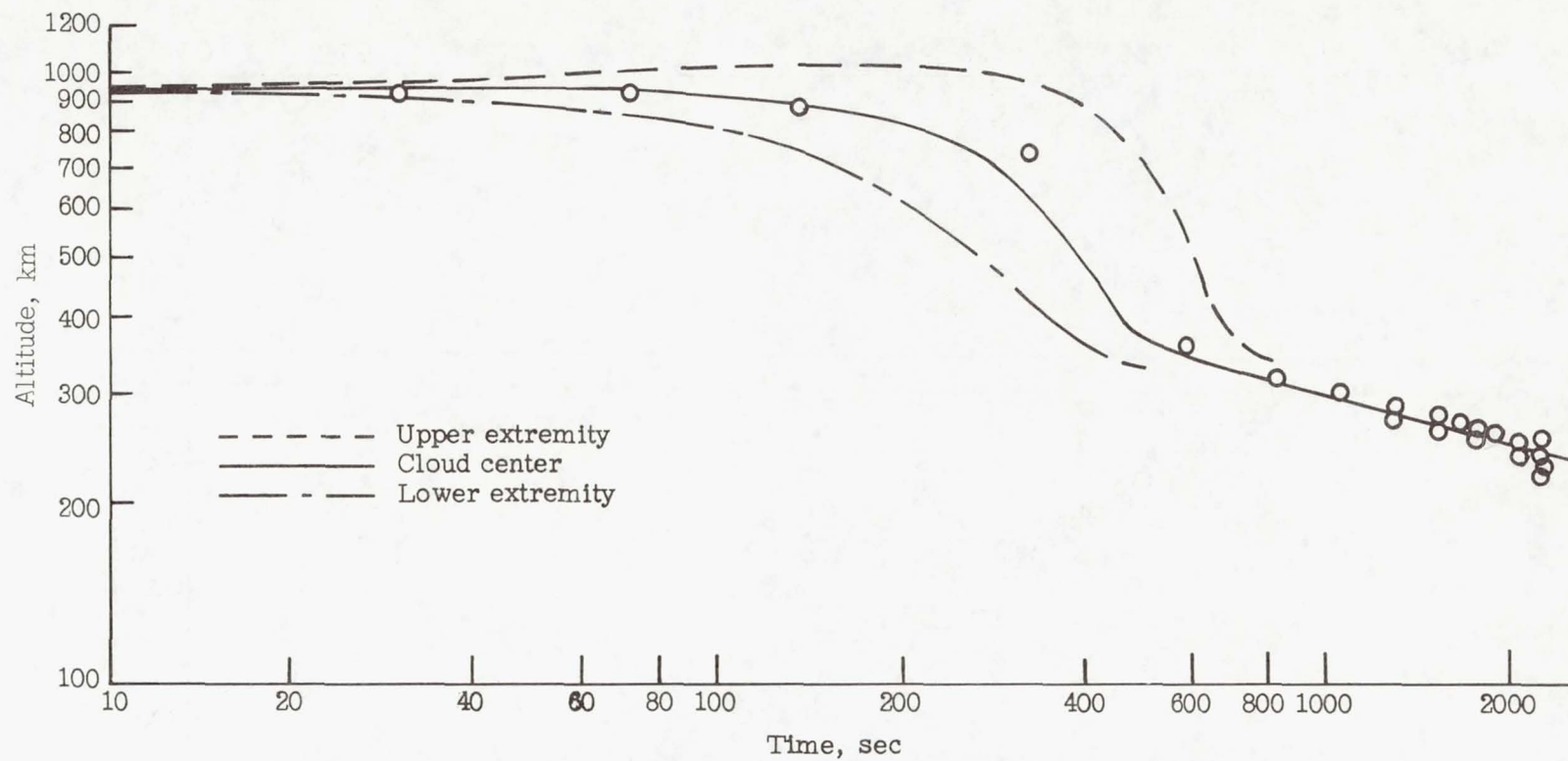
Figure V-7.- Variation of altitude of center and extremities of ion cloud with time.
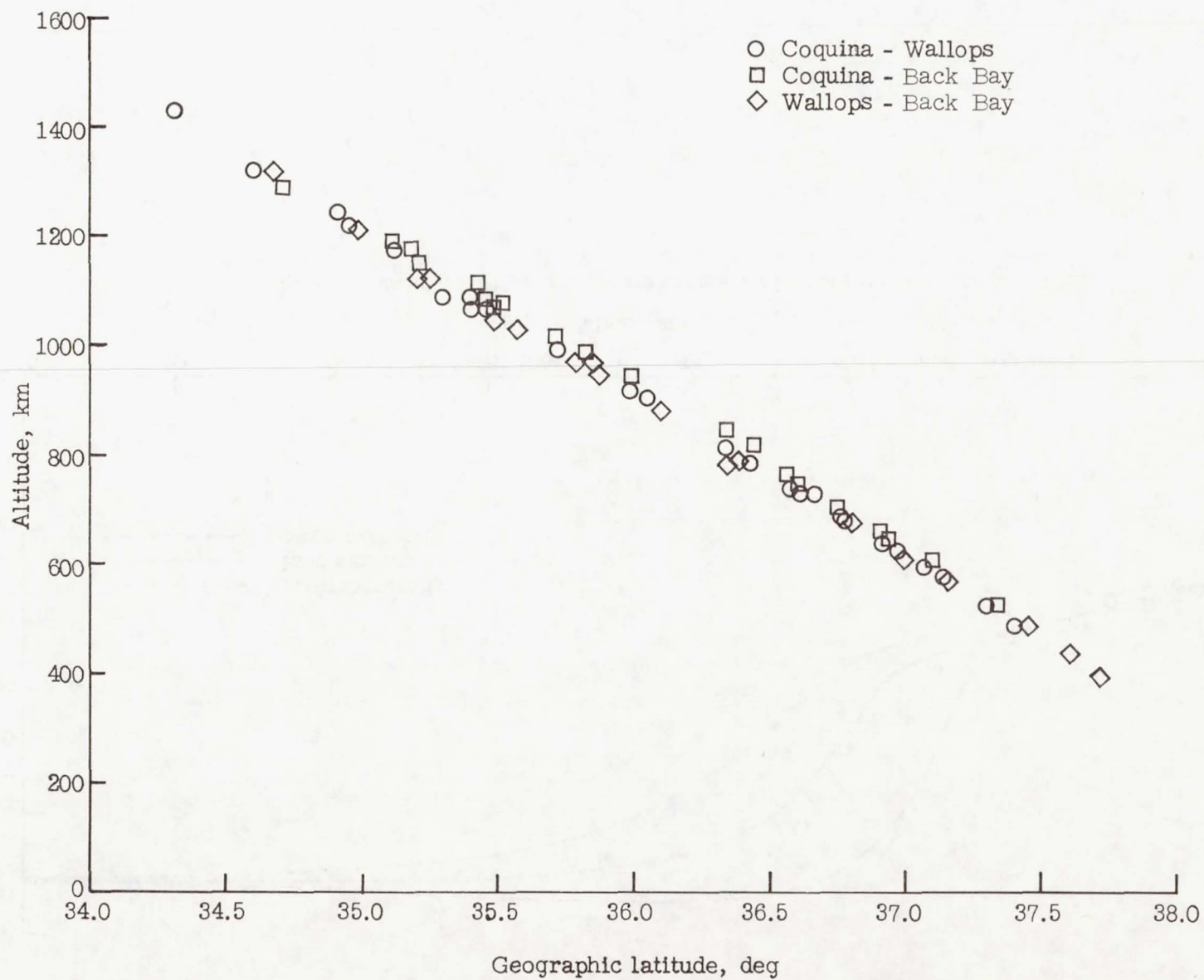
Figure V-8.- Variation of altitude of cloud center line with latitude (400 seconds after release).
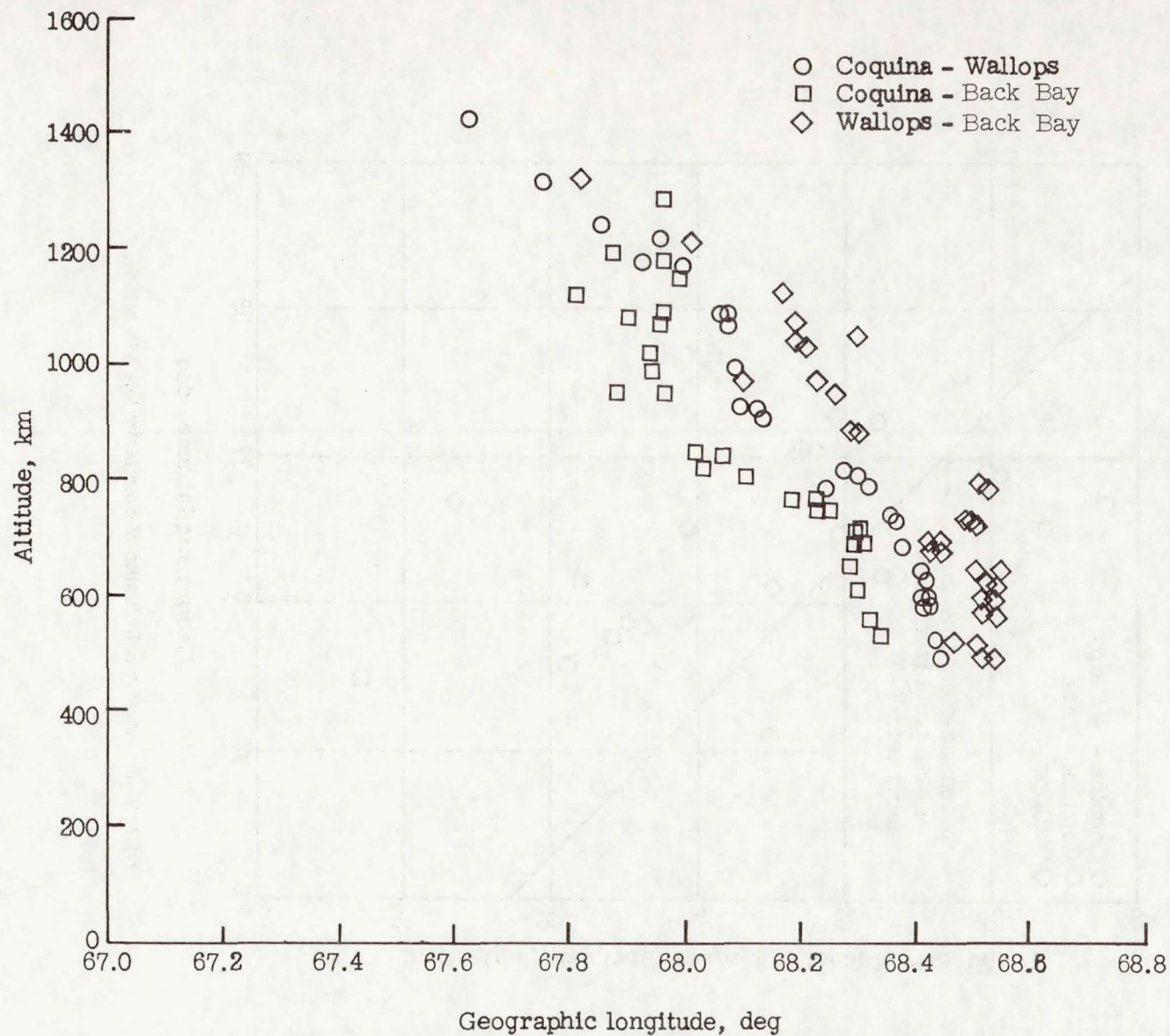
Figure V-9.- Variation of altitude of cloud center line with longitude (400 seconds after release).
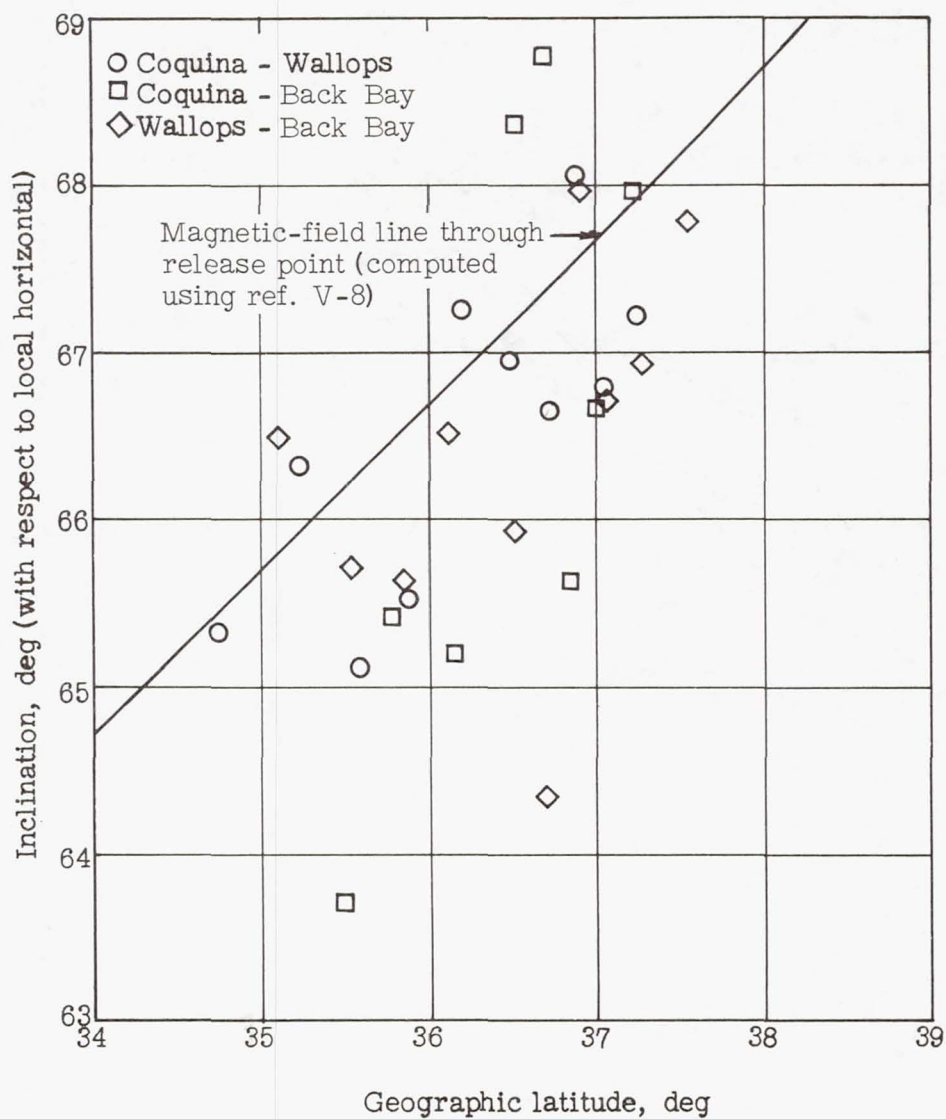
Figure V-10.- Variation of inclination of cloud center line with latitude.
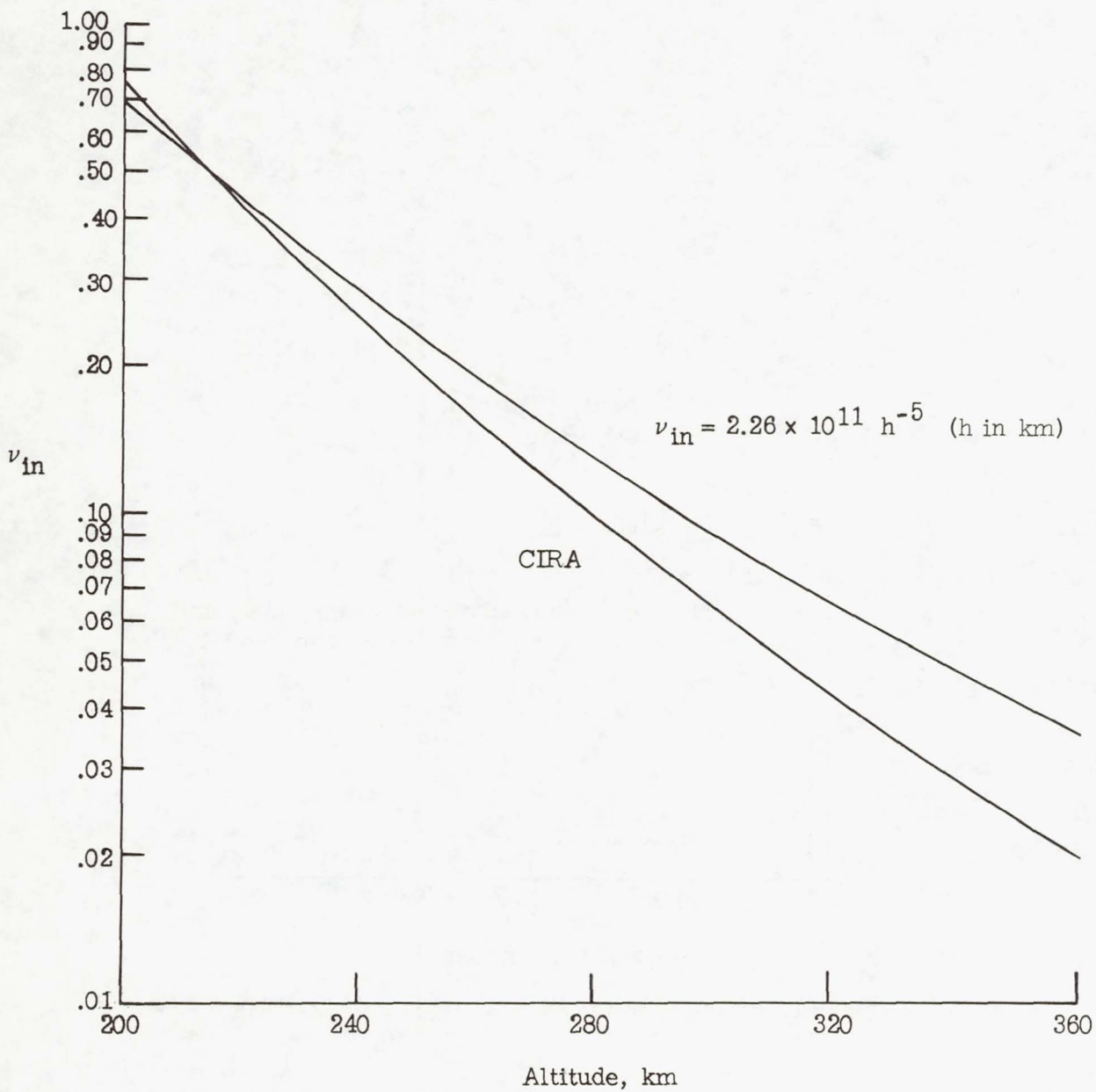
Figure V-11.- Ion neutral collision frequency as function of altitude.

The graph shows ν_{in} on the vertical axis (logarithmic scale from .01 to 1.00) versus Altitude, km on the horizontal axis (from 200 to 360).

$$\nu_{in} = 2.26 \times 10^{11} \ h^{-5} \quad (h \text{ in km})$$

CIRA
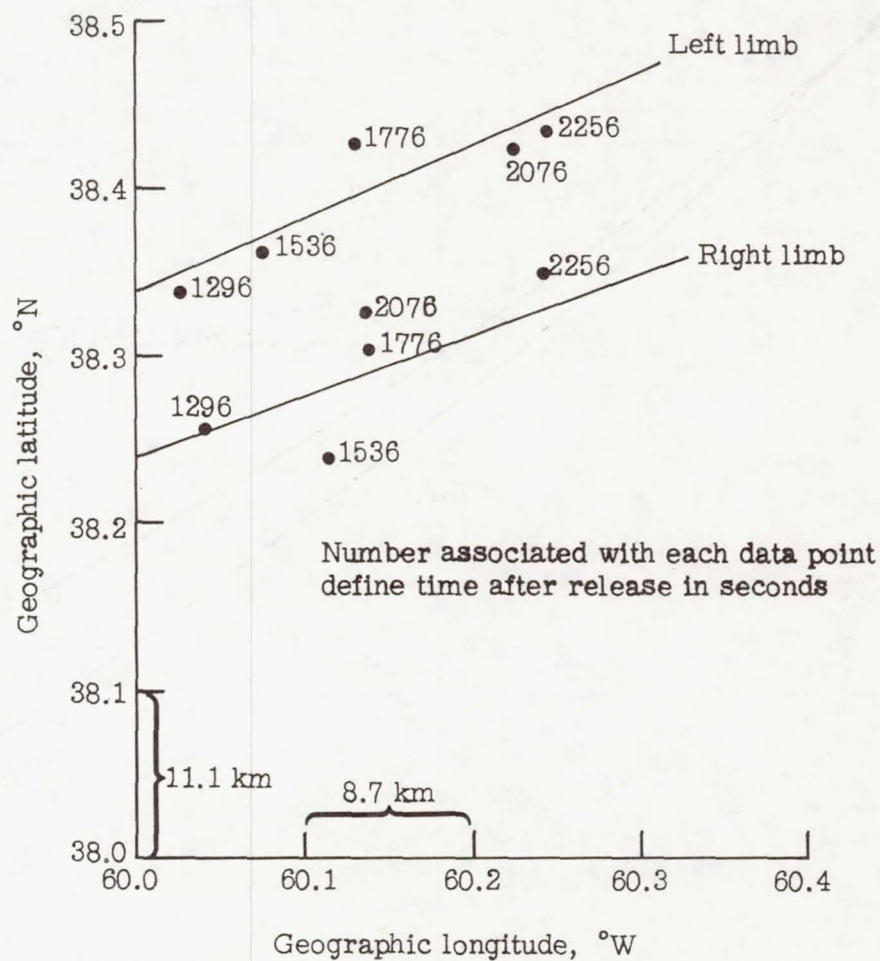
Figure V-12.- Geographic coordinates of northern and southern edges of cloud at altitude of 250 km.

VI. SPECTROPHOTOMETER MEASUREMENTS

By K. A. Dick
Institute for Cooperative Research,
The Johns Hopkins University

INTRODUCTION

The barium releases on September 24, 1966, were observed from a site at The Johns Hopkins University (39.4^O N, 76.6^O W). No observations of the releases on September 25 were made. The emission spectra of the releases were recorded in the wavelength region from 3490 Å to 6490 Å by using a 0.5-meter Ebert spectrophotometer. Nineteen spectral features were recorded and have been identified as four lines of singly ionized barium Ba II; 14 lines of neutral barium Ba I; and the resonance line of neutral strontium Sr I, an impurity in the release.

INSTRUMENTATION

The 0.5-meter Ebert spectrophotometer used was similar to those flown in airglow and aurora rocket experiments and described in reference VI-1. A photograph of the instrument is shown as figure VI-1. The instrument employed a grating with 1200 grooves per mm with an Electro-Mechanical Research Model 541-E photomultiplier tube as the detector. The spectral region from $\lambda = 3490$ Å to $\lambda = 6490$ Å was scanned every 15 seconds, where λ is wavelength. The signal was recorded directly on a Mark 280 Brush recorder at two stages of amplification and simultaneously on a Model 8100 Honeywell tape recorder. In order to stay within the response-time limitations of the recording apparatus, it was not possible to use a slit width less than 1 mm, thus resolution was restricted to approximately 16 Å. The spectral sensitivity of the instrument was determined by using a standard lamp with a known spectral emission profile. This sensitivity was used in estimating the relative intensities of the lines observed. The intensity scale is arbitrary.

DATA OBTAINED

A list of the lines observed is presented as table VI-I. The wavelengths given are from reference VI-2. The classifications of the Ba I lines are from reference VI-3; those of Ba II and Sr I are calculated from the energy levels of reference VI-4. Partial energy-level diagrams of Ba I and Ba II are shown as figures VI-2 and VI-3, respectively.

The only lines recorded for more than two scans from the first release were three Ba II lines, the Ba I resonance line at 5535 Å, and the Sr I resonance line. Eight other lines were recorded for one or two scans. Table VI-II gives the intensities of the lines for each of the scans during which they were recorded after the first release.

Table VI-III gives the intensities of the lines observed after the second release. Figure VI-4 shows the intensities of the Ba I resonance line and three of the typical non-resonance Ba I lines as a function of time after the second release. Figure VI-5 shows the time variation of four lines: the Ba I resonance line, 5535 Å; the Sr I resonance line, 4607 Å; an average of the Ba II lines, 4554 Å and 4934 Å, which terminate with the ground state 6s ^{2}S; and an average of the Ba II lines, 5853 Å and 6141 Å, which terminate with the metastable 5d ^{2}D.

The accuracy of the intensities is considered to be about ±1 unit below 25 units. Above 25 units, the inaccuracy will be greater (of the order of 10 percent) due to an asymmetry of recorded line shape introduced in the stronger lines by a mismatching of impedances between the signal amplifier and the tape recorder. The times given in tables VI-II and VI-III are accurate to ±1 second.

No prominent features other than those listed have been seen on records from the Brush recorder. If any weak features such as bands of BaO are present, it might be possible to process the tape on a computer to superimpose successive scans and increase the signal-to-noise ratio enough to make such features observable. Computer time and facilities have not yet permitted such an examination, but it is hoped that the tape will be subjected to such a procedure in the future.

DISCUSSION OF DATA OBTAINED FROM SECOND RELEASE

The variation of the relative intensities of the observed lines is due to two general effects. The first is the change in relative abundance of Ba I and Ba II due to ionization of the Ba I. The second is the change of the total number of particles of each type in the field of view of the spectrophotometer due to the changing geometry of the clouds. (The instrument was kept in a fixed position while observing each cloud.)

In the following discussion, data from the second release is considered. For this release, the area in the field of view at the position of the cloud was approximately 3.2 km vertical by 56 km horizontal.

If it were assumed that the geometries of the expanding spherical shells of Ba I and Sr I were the same, then the ratio of the intensities of lines from the two species would yield the ionization rate of the barium. For example, if the intensities I_I of Ba I and I_{Sr} of Sr I are expressed as functions of t, the time after release

$$I_I(t) = K_I f(t) \beta N_o e^{-\alpha t} \tag{1}$$

$$I_{Sr}(t) = K_{Sr} f(t) N_{Sr} \tag{2}$$

and the relative intensity I_{rel} as a function of t is

$$I_{rel}(t) = \frac{I_I(t)}{I_{Sr}(t)} = K_{rel} e^{-\alpha t} \tag{3}$$

where

$f(t)$ common geometrical variation of neutral clouds

K_I measure of emission cross section of Ba I

K_{Sr} measure of emission cross section of Sr I

K_{rel} relative emission cross section

N_{Sr} number of Sr I atoms

α measure of ionization rate of Ba I subsequent to release

βN_o number of Ba I atoms remaining after initial ionization

Figure VI-6 shows I_{rel} as a function of t, where $I_I(t)$ is the intensity of the $\lambda = 5535$ Å resonance line $\left(\text{until } I_I(t) \text{ becomes so small as to be relatively inaccurate}\right)$. The form of the graph suggests a relation of the type given by equation (3) between times of approximately 85 and 145 seconds after release and yields a value for α of 1/38 $\sec^{-1}$. The variation prior to $t \approx 80$ sec could be accounted for if the cloud was optically thick to $\lambda = 5535$ Å at that time. From figure VI-5, it would appear that the ionized cloud may have been optically thick to the lines of Ba II ($\lambda = 4554$ Å and $\lambda = 4934$ Å) terminating at the ground state $^2S_{1/2}$ prior to $t \approx 170$ sec.

Further reduction of the data is made difficult by limitations of the apparatus used. Since the instrument was designed for use on extended sources such as aurorae, no azimuth-elevation mount was available which would give accurate readouts of look angles used. Hence, the instrument was visually aimed at the center of each release and was

left there throughout the observing times. It would therefore be difficult to relate Ba II intensities to a specific portion of the ionized cloud or to separate spatial from temporal variations in that cloud.

SUMMARY OF RESULTS

The use of a spectrophotometer has proven useful but is probably limited to survey work, for example, the establishment of spectral features present in chemical releases. Its usefulness might be enhanced if it were set on an azimuth-elevation mount with information-output capabilities.

In order to provide more extensive and detailed ground support, the use of photometers would appear to offer more promise. Wide-angle photometers filtered for specific wavelengths would yield quantitative intensity information which should be valuable in establishing yield of the various barium-release systems contemplated for future use and in measuring temporal variations in total intensities. Narrow-angle photometers could be used to advantage in mapping spatial variations of emitting particles. This would be especially useful when photometers set on the same spectral line are operated from widely separated sites. Such photometers could be centered on the point of release and preprogramed to scan a given pattern about the release point. The capability for continuous automatic output of look-angle information along with photometric information would be necessary for later reduction of the acquired data.

REFERENCES

VI-1. Fastie, William C.: Instrumentation for Far-Ultraviolet Rocket Spectrophotometry. J. Quant. Spectry. Radiat. Transfer, vol. 3, no. 4, Oct./Dec. 1963, pp. 507-518.

VI-2. Hodgman, Charles D.; Weast, Robert C.; and Selby, Samuel M., eds.: Handbook of Chemistry and Physics. Thirty-eighth ed., Chem. Rubber Pub. Co., 1956-1957.

VI-3. Russell, Henry Norris; and Moore, Charlotte E.: The First Spectrum of Barium, Ba I. J. Res. Nat. Bur. Stand., vol. 55, no. 6, Dec. 1955, pp. 299-306.

VI-4. Moore, Charlotte E.: Atomic Energy Levels. Vol. III – 42Mo-57La and 72Hf-89Ac. NBS Circ. 467, U.S. Dep. Com., May 1, 1958.

TABLE VI-I.- LINES OBSERVED

Source	Wavelength, Å	Classification
Ba I	3501.1	$6s^2\,^1S_0$ - $6p'\,^1P_1^o$
Ba I	3993.4	$5d\,^3D_3$ - $4f\,^3F_4^o$
Ba I	4283.1	$5d\,^1D_2$ - $4f\,^1F_3^o$
Ba II	4554.0	$6s\,^2S_{1/2}$ - $6p\,^2P_{3/2}^o$
Sr I	4607.3	$5s^2\,^1S_0$ - $5p\,^1P_1^o$
Ba I	4726.4	$5d\,^1D_2$ - $7p\,^1P_1^o$
Ba II	4934.1	$6s\,^2S_{1/2}$ - $6p\,^2P_{1/2}^o$
Ba I	5535.6	$6s^2\,^1S_0$ - $6p\,^1P_1^o$
Ba I	5826.3	$5d\,^1D_2$ - $6p'\,^1P_1^o$
Ba II	5853.7	$5d\,^2D_{3/2}$ - $6p\,^2P_{3/2}^o$
Ba I	5971.7	$5d\,^3D_2$ - $6p'\,^3P_2^o$
Ba I	5997.1	$5d\,^3D_1$ - $6p'\,^3P_1^o$
Ba I	6019.5	$5d\,^3D_1$ - $6p'\,^3P_0^o$
Ba I	6063.1	$5d\,^3D_2$ - $6p'\,^3P_1^o$
Ba I	6110.8	$5d\,^3D_3$ - $6p'\,^3P_2^o$
Ba II	6141.7	$5d\,^2D_{5/2}$ - $6p\,^2P_{3/2}^o$
Ba I	6341.7	$5d\,^3D_2$ - $6p'\,^3D_3^o$
Ba I	6450.8	$5d\,^3D_1$ - $6p'\,^3D_2^o$
Ba I	6482.9	$5d\,^1D_2$ - $6p'\,^1F_3^o$

TABLE VI-II.- INTENSITIES OF LINES OBSERVED
AFTER FIRST RELEASE

Source	Wavelength, Å	Intensities of lines recorded during scan commencing at time, sec after release –									
		16	31	46	61	76	91	106	121	136	151
Ba I	4283	9.0									
Ba II	4554	93	72	43.4	29.3	21.0	15.5	12.6	8.6	7.6	6.3
Sr I	4607	240	79	39.7	24.0		12.3	9.6	5.3	3.5	5.9
Ba I	4726	7.3									
Ba II	4934	75	47	27.2	24.0	12.8	12.2	11.7	11.2	8.5	5.6
Ba I	5535	650	127	40.9	22.6	9.9	6.6	6.6	6.6	4.8	3.9
Ba I	5826	27.1	4.9								
Ba I	5971	8.5	2.8								
Ba I	6019	17.8									
Ba I	6063	20.7									
Ba I	6110	28.4	6.4								
Ba II	6141	43.5	33.5	14.2	14.2	13.6	9.0	10.0	8.1	7.0	8.0
Ba I	6450	42.5									

TABLE VI-III.- INTENSITIES OF LINES OBSERVED AFTER SECOND RELEASE

Source	Wavelength, Å	Intensities of lines recorded during scan commencing at time, sec after release —																	
		5	20	35	50	65	80	95	110	125	140	155	170	185	200	215	230	245
Ba I	3501		[a]25	[a]10	[a]5													
Ba I	3993		12.8	2.6														
Ba I	4283		3.6	1.3	0.4													
Ba II	4554		31.6	28.5	26.6	27.2	27.2	24.1	24.4	25.0	23.4	24.7	22.8	21.5	20.6	20.6	17.7	17.1
Sr I	4607		32.4	30.0	28.8	26.8	26.5	21.2	19.4	17.6	16.2	10.6	9.4	5.9	6.6	3.2	2.6	1.8
Ba I	4726		4.6	1.6	1.1													
Ba II	4934		24.9	25.3	24.9	24.4	22.9	23.2	20.6	20.0	19.1	18.2	17.4	17.1	17.6	14.7	14.1	13.8
Ba I	5535	33.3	30.3	29.7	26.7	21.5	14.5	8.2	4.8	2.4	1.8	1.2	1.5	1.5	0.9	0.9	0.9	
Ba I	5826	26.5	12.9	5.1	3.7	1.5												
Ba II	5853	[a]6	[a]4	[a]5	4.3	3.1	2.0	2.3	3.1	2.0	2.3	2.3	2.0	1.6	2.0	2.0	1.6	1.6
Ba I	5971	23.5	9.7	2.5	0.8													
Ba I	5997	30.2	8.6	4.3	1.4													
Ba I	6019	35.4	11.1	4.0	0.9													
Ba I	6063	33.3	16.2	6.9	2.8	0.9	0.5											
Ba I	6110	43.3	26.0	9.6	2.9	1.9	1.4											
Ba II	6141	28.0	26.5	23.0	19.5	15.0	17.0	13.5	12.0	12.5	12.0	10.0	7.5	8.0	9.0	7.5	6.0	8.0
Ba I	6341	26.1	7.2	2.9														
Ba I	6450	23.8	7.1	3.2														
Ba I	6482	23.1	6.7	1.9														

[a]Less accurate values.

TABLE VI-III.- INTENSITIES OF LINES OBSERVED AFTER SECOND RELEASE – Concluded

Source	Wavelength, Å	Intensities of lines recorded during scan commencing at time, sec after release –																						
		260	275	290	305	320	335	350	365	380	395	410	425	440	455	470	485	500	515	530	545	560	575
Ba I	3501																						
Ba I	3993																						
Ba I	4283																						
Ba II	4554	10.8	15.5	13.9	19.9	13.6	13.3	12.7	12.0	10.4	9.5	9.2	8.2	7.9	6.6	6.3	6.3	5.4	5.1	4.4	4.4	3.8	3.5
Sr I	4607	1.8	1.8	0.9	0.6	0.6	0.4	0.4	0.6	0.6													
Ba I	4726																						
Ba II	4934	13.5	11.2	12.1	10.6	10.3	9.4	8.8	8.2	7.4	7.9	6.8	5.6	5.0	4.4	5.0	4.7	3.2	4.1	3.5	3.2	2.6	2.4
Ba I	5535																						
Ba I	5826																						
Ba II	5853	1.6	1.6	1.6	1.6	1.6	1.6	1.2	1.2	1.2													
Ba I	5971																						
Ba I	5997																						
Ba I	6019																						
Ba I	6063																						
Ba I	6110																						
Ba II	6141	6.5	5.5	5.5	5.0	5.5	4.0	4.0	3.5	4.0	4.5	4.0	3.0	3.0	3.0	3.0	2.0	2.5	2.0	2.0	2.0	2.0	1.0
Ba I	6341																						
Ba I	6450																						
Ba I	6482																						

L-71-535

Figure VI-1.- 0.5-meter Ebert spectrophotometer.

Figure VI-2.- Partial energy-level diagram of Ba I.
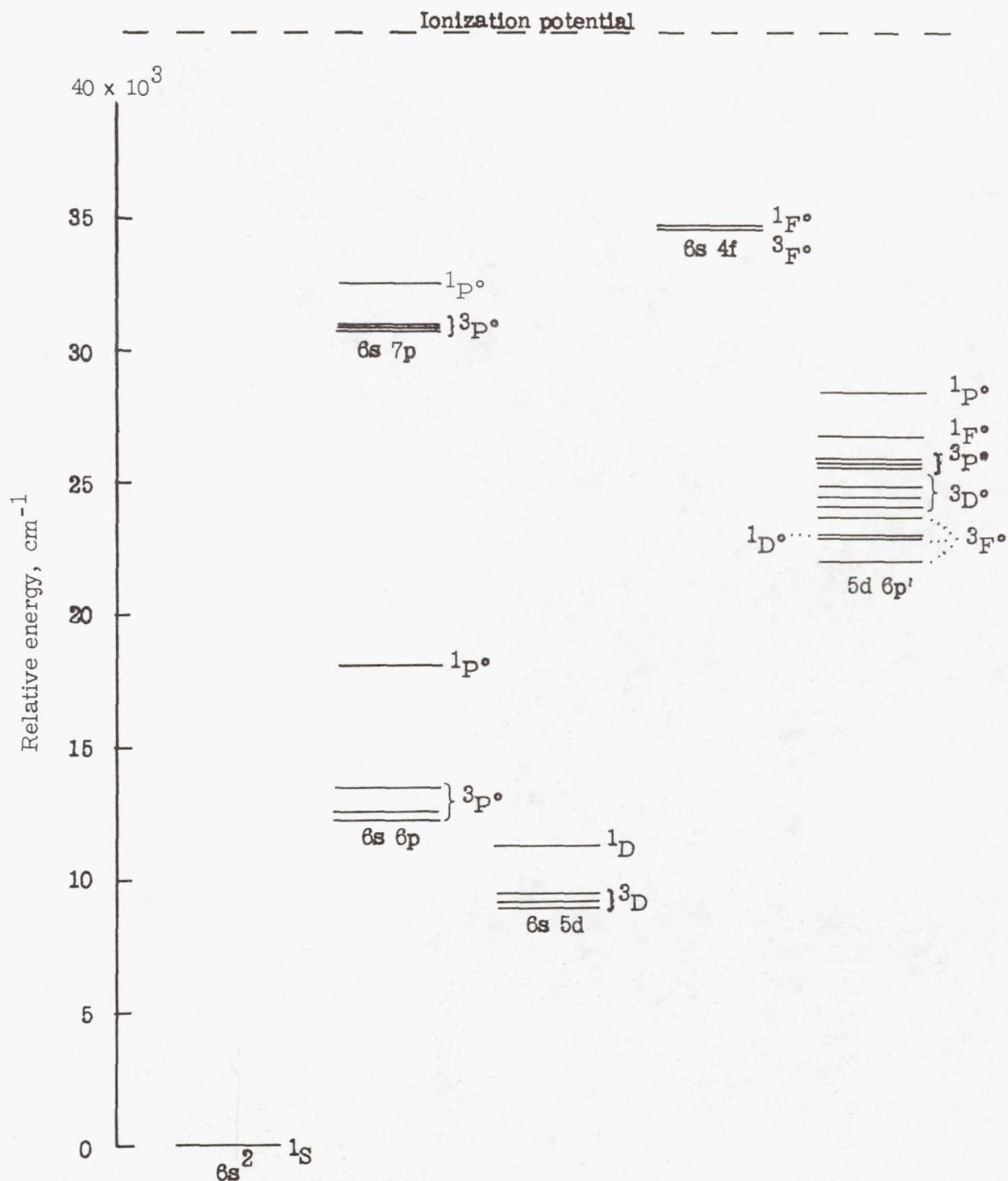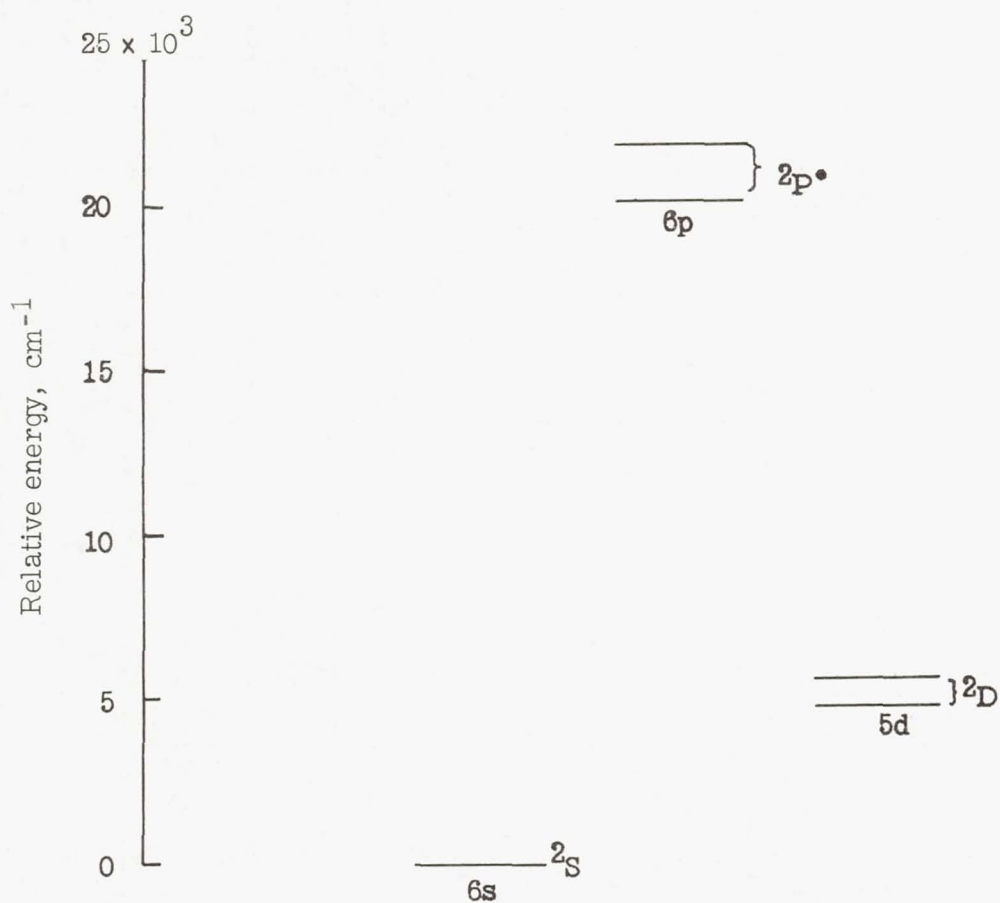
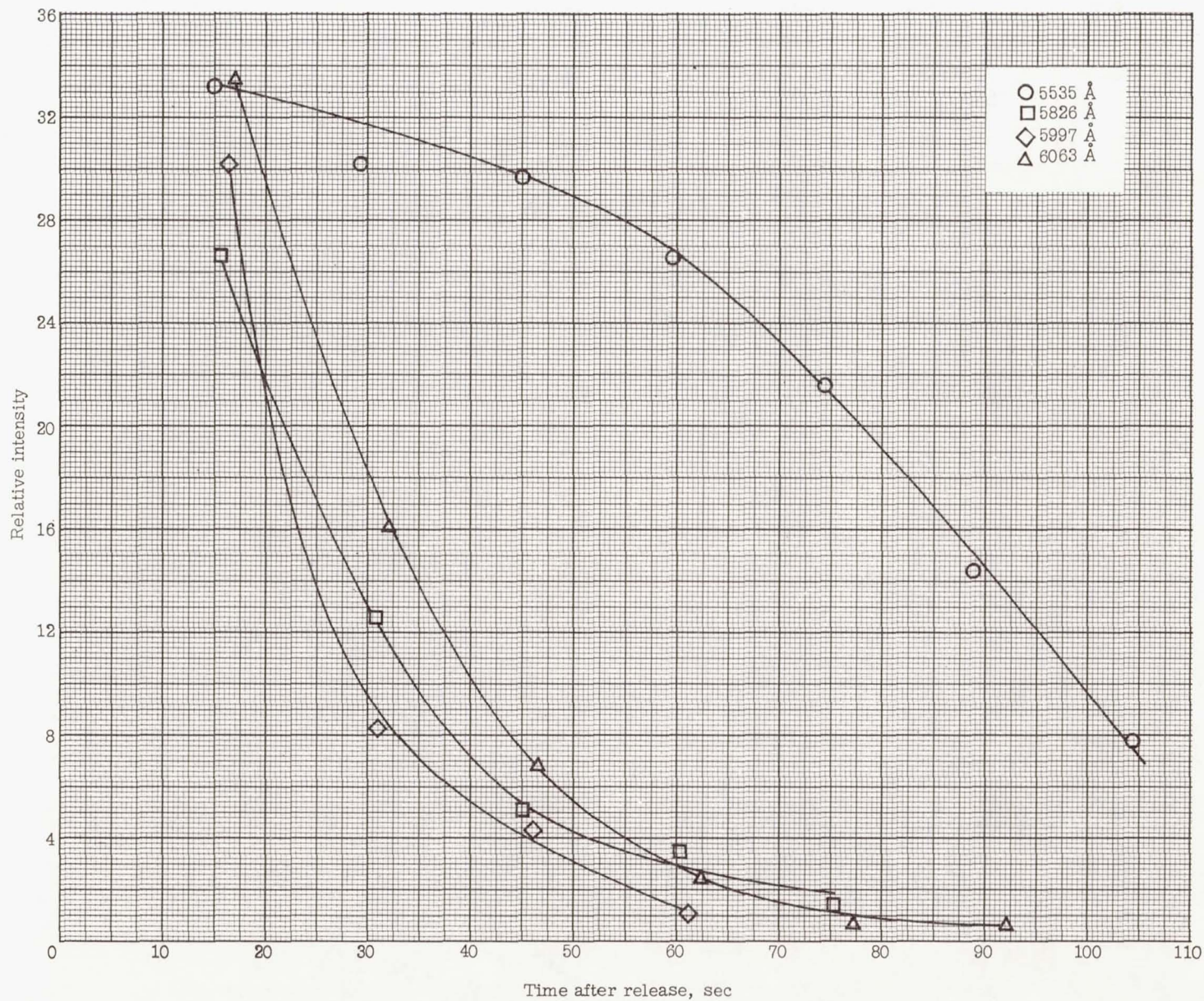Figure VI-3.- Partial energy-level diagram of Ba II.

Figure VI-4.- Time variation of intensity of four Ba I lines from second release.
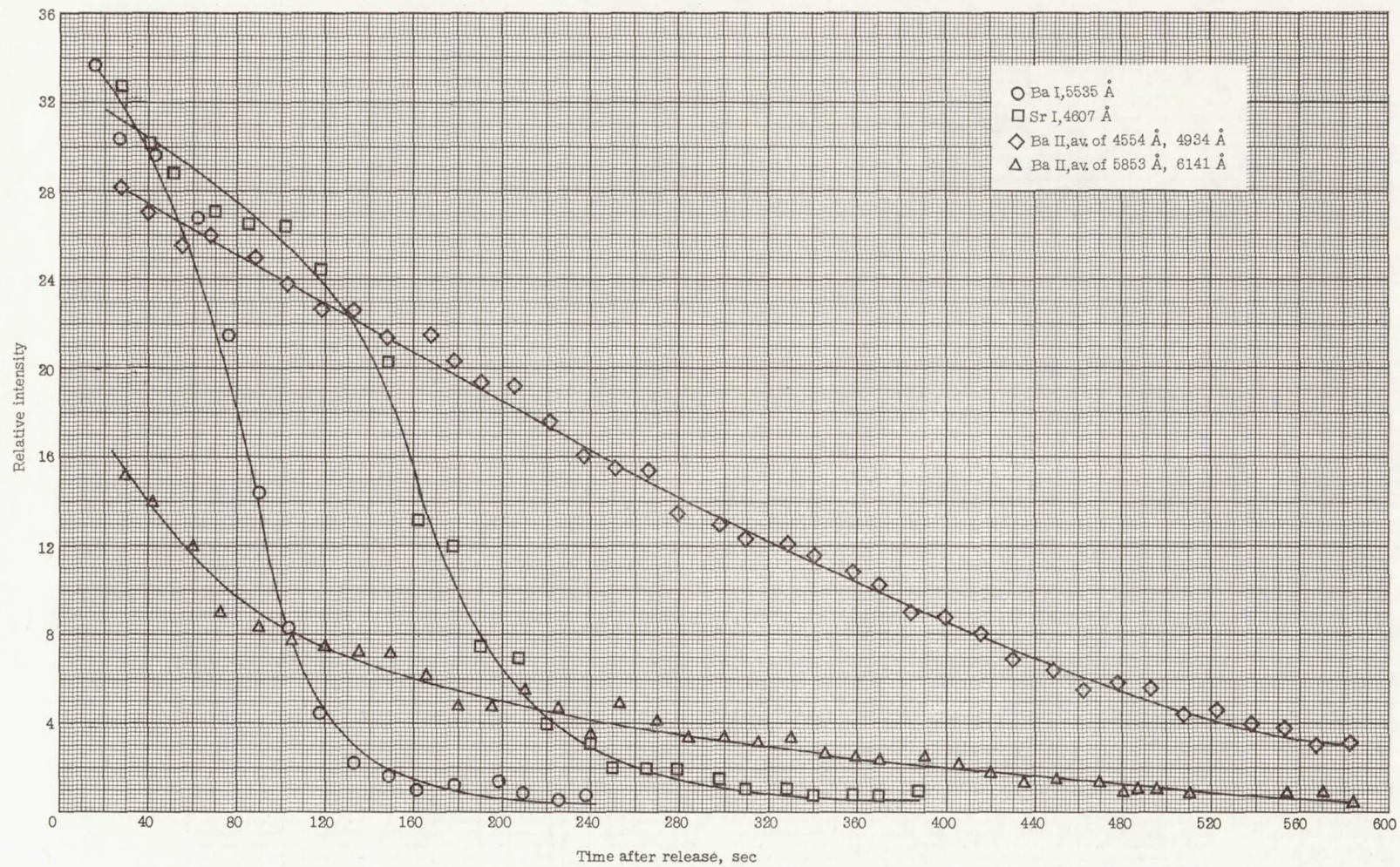
Figure VI-5.- Time variation of Ba I and Sr I resonance lines and two averages of Ba II lines from second release.
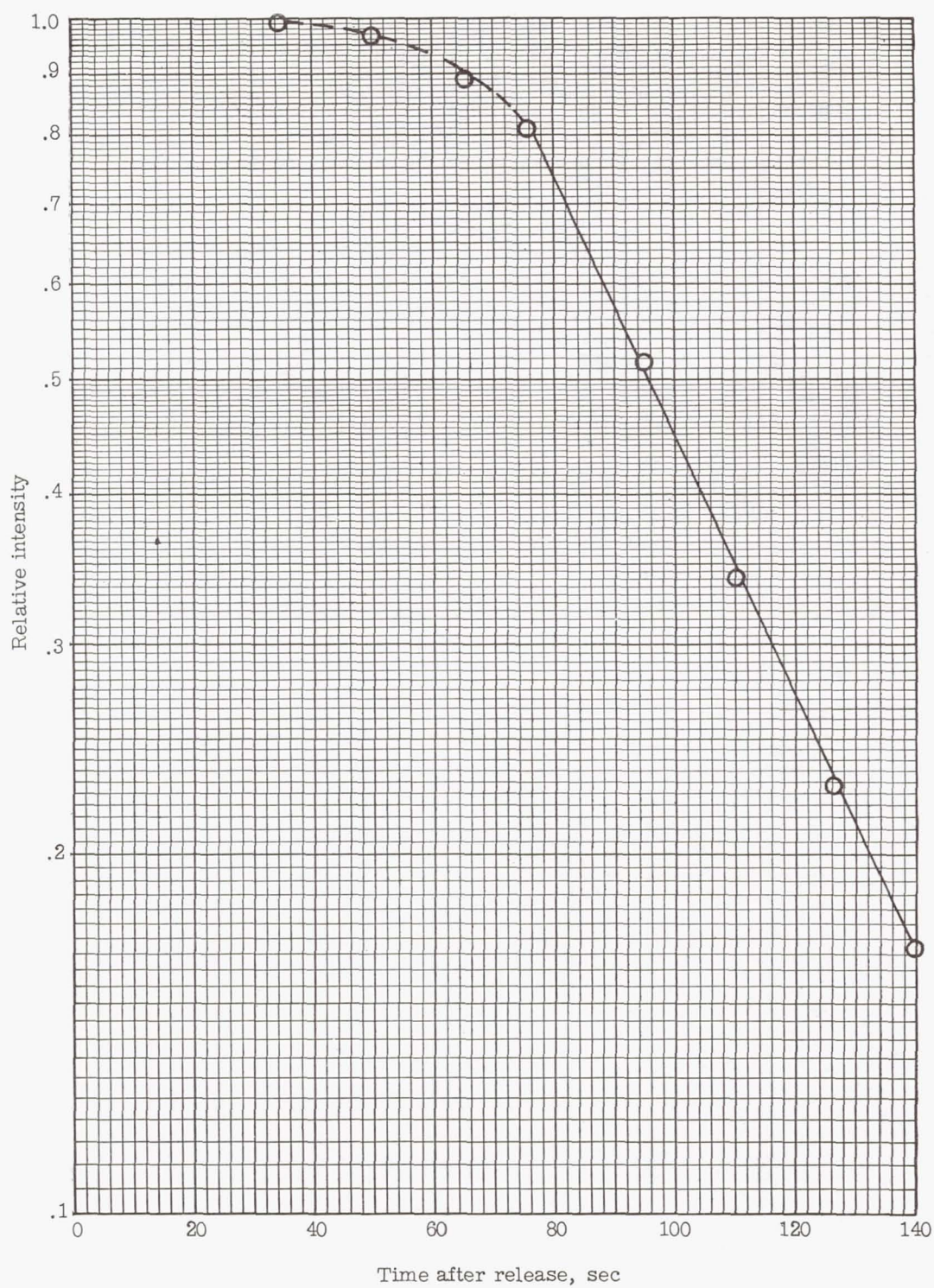
Figure VI-6.- Time variation of intensity of Ba I resonance line relative to Sr I resonance line from second release.

VII.   PHOTOMETRY OF BARIUM ION CLOUDS

By E. R. Manring
Department of Physics,
North Carolina State University

INTRODUCTION

Photometry of the barium ion emission at 4554 Å for the five clouds generated on September 24 and 25, 1966, is reported from observations made from Coquina Beach, North Carolina.   This work was undertaken to determine ionization efficiency of the pay-loads used and photon scattering rate from ionized barium.   For design purposes it is desirable to know each of these parameters independently since photometric measure-ments involve the product of these two quantities.   Estimates of the scattering rate are used to evaluate ionization efficiency.   Preliminary estimates of ionization efficiency have been made and are reported herein.

The scattering rate per ion is taken as equal to the absorption rate per ion since collisional deactivation at the ambient pressure is believed to be negligible.   This rate is also a product of two quantities.   One of these involves the oscillator strength of the transition and the other, the incident solar flux at 4554 Å.   Calibration details are included to permit a reevaluation of the data should more information on these basic parameters become available.   For some types of experimental planning and evaluation, the photo-metric quantities reported herein are all that are needed, and the relative values of scattering rate and ionization efficiency are less important.

INSTRUMENTATION AND EXPERIMENTAL TECHNIQUE

The photometer utilized employed an interference filter 4 inches (101.6 mm) in diameter, of about 16 Å half-width centered at 4554 Å; an objective lens; a field stop to define the angular field; a birefringent filter; and a photomultiplier detector.   The optical characteristics of a similar photometer are described in reference VII-1; a schematic diagram appears in sketch 1.

The birefringent filter employed two quartz elements having a combined length of about 50 mm.   This filter produces a channeled curve when transmission is plotted against wavelength.   The rotation of the polarizer causes the transmission function to scan in wavelength as this polarizer is rotated.
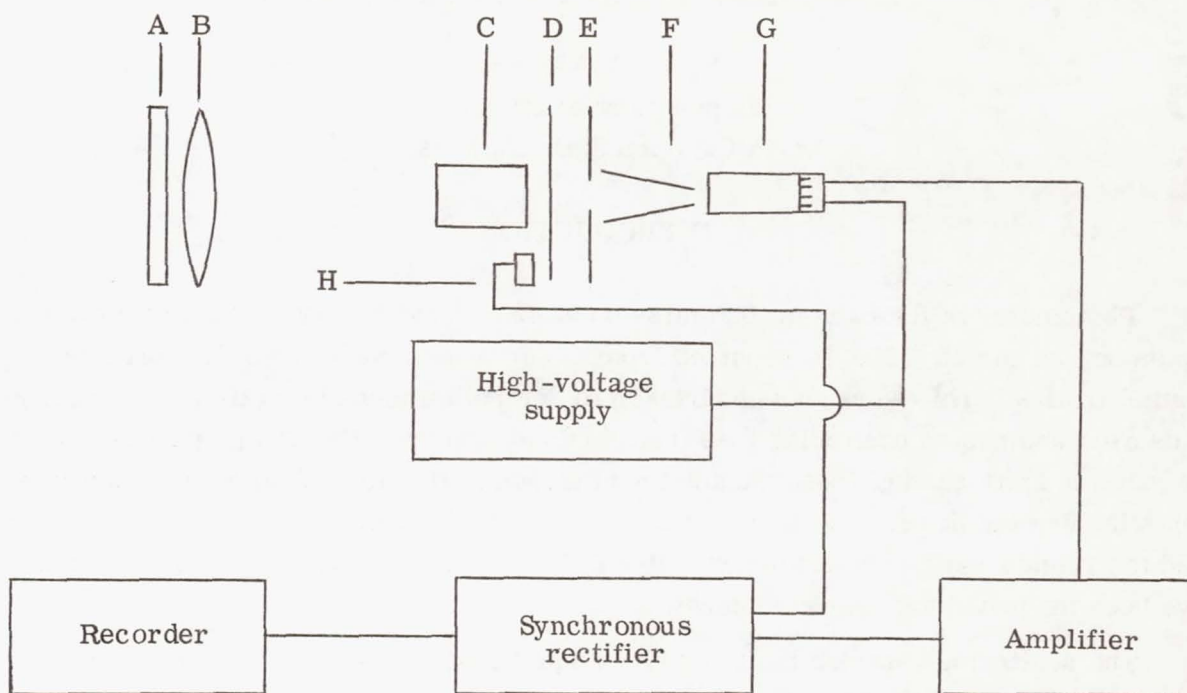
A   Interference filter, 4-in. (101.6 mm) diameter

B   Objective lens, 4-in. (101.6 mm) diameter, 11-in. (27.94 cm) focal length

C   Quartz elements of the birefringent filter

D   Rotating polarizer

E   Field stop, 7.7° full-field angle

F   Light funnel

G   Photomultiplier

H   Reference generator keyed to rotating polarizer

Sketch 1.

The transmission for the birefringent filter T_B can be expressed as

$$T_B = T_{max}\left[\frac{\cos\left(\frac{2\pi\lambda}{\Delta\lambda} + 2\omega t\right) + 1}{2}\right]$$

where

λ wavelength, Å

62

$\Delta\lambda$ characteristic of filter, about 4 Å in region of 4500 Å

ω angular velocity of rotating polarizer

t   time

T_{max} maximum transmission

The total transmission of the photometer T is given by $T = T(\lambda)T_B$, where $T(\lambda)$ is the transmission of all other components and is dominated by the interference filter.

For light due to continuum $I(\lambda)$ falling into the instrument, the light flux ϕ at the cathode is

$$\phi = \int_0^\infty I(\lambda)T(\lambda)T_B \, d\lambda$$

This quantity is essentially independent of t if $I(\lambda)$ and $T(\lambda)$ do not have marked discontinuities compared to $\Delta\lambda$. On the other hand, a line emission produces a modulated flux at the cathode of angular frequency 2ω. For a particular voltage applied to the photomultiplier detector, the output current is proportional to the light incident upon the cathode. The output current may be separated into ac and dc components of which the ac component is proportional to line emission present upon the detector cathode.

The integral in the preceding equation was described as essentially independent of t for typical values of $I(\lambda)$ and $T(\lambda)$. It does contribute, in practice, a slight ac component to the detector output. For continuum starlight and for scattered sunlight during the twilight interval of the ionized cloud observations the contribution due to such extraneous modulation was negligible compared to the 4554 Å line emission measured and reported. The instrument limit of observation was set by the ability of the observer to detect the 4554 Å cloud visually and subsequently to point the photometer.

The photomultiplier was followed by an operational amplifier for impedance transformation, a synchronous rectifier, and a chart recorder. The gain of the photomultiplier tube was determined by the voltage supplied to it and was adjustable in discrete 100-volt steps. The synchronous rectifier received the ac component from the photomultiplier operational amplifier as well as a reference signal from the rotating polarizer associated with the birefringent filter. The rectified output of this unit is proportional to the ac input and the cosine of the phase angle between this signal and the reference voltage. The phase angle was, in all cases, set to zero by proper adjustment utilizing a line source of barium 4554 Å radiation.

The entire instrument — optics, electronics, and recording components — was calibrated by using the Sun as a source. A clear day following the entry of clear polar air was used and measurements were performed near local noon. Since the instrument does not respond to continuum nor the sunlight, a mechanical chopper operating at a frequency near that produced by the polarizer was used. This chopper was in front of all optics, that is, between the interference filter and the Sun. The photometer field angle was much greater than that of the Sun. With the instrument pointed at the Sun, the following condition prevailed:

$$D_s = A_s T_s T_{nd} \int_0^\infty T_i(\lambda)\, \psi_s(\lambda)\, d\lambda\; T_{I,s} G_s$$

where

D_s recorder deflection when pointed at Sun

A_s aperture area used with Sun, 0.297 cm^2

T_s transmission of atmosphere at time of calibration

T_{nd} transmission of neutral-density filter to reduce light at cathode, 1/1160

$T_i(\lambda)$ transmission of interference filters and birefringent filter as function of wavelength, $T_i(4554 \text{ Å}) = 1$

$\psi_s(\lambda)$ solar flux at surface of earth per unit wavelength interval

$T_{I,s}$ overall transmission of optics at 4554 Å, filters excluded

G_s combined gain of photomultiplier and electronics during calibration

The integral $\int_0^\infty T_i(\lambda)\, \psi_s(\lambda)\, d\lambda$ was evaluated from the measured characteristics of the interference filter and birefringent filter for an average polarizer position (the polaroid was rotated during calibration run to assure an average) and from published values of $\psi_s(\lambda)$. Outside of the Fraunhofer dip, $\psi_s(\lambda)$ was taken as 5×10^{13} photons/cm^2/Å/sec. Reference VII-2 was used to account for the wavelength dependence of $\psi_s(\lambda)$. The interference filter half-power points were very nearly 8 Å each side of 4554 Å, but channeling of the birefringent filter effectively reduced the width by one-half.

For observations of the barium clouds a half-field angle of 3.37^O was used. This wide angle was employed to include as much of the cloud as possible within the field of view. Wider field angles were not employed because of the characteristics of the interference filter with larger incidence angles. The recorder deflection with the photometer pointed at a barium cloud is given by

$$D_c = A_c T_c T_{I,c} G_c \left(\frac{K I_c}{4 \pi R^2} \right)$$

where

D_c recorder deflection when pointed at cloud

A_c aperture used, 55.3 cm^2

T_c transmission of atmosphere

$T_{I,c}$ transmission of instrument at 4554 Å

G_c gain of photomultiplier and electronics

K fraction of cloud within photometer's field of view

I_c intensity from cloud, photons/sec

R range, cm

Recorder deflections can, therefore, be interpreted directly in terms of cloud intensity if the following conditions exist:

(1) $T_{I,c} = T_{I,s}$ as expected

(2) $T_s = T_c$, which is a best estimate since both observations and calibration were performed under very clear skies at comparable zenith angles

(3) G_c and G_s have the relative values indicated by attenuator controls which is certainly expected, since every attempt was made to assure linearity

The resulting expression for I_c in photons/sec is

$$I_c = \frac{D_c 4 \pi R^2 \times 8.20 \times 10^9}{K G_c}$$

65

or for ϕ in photons at earth/cm^2/second is

$$\phi = \frac{I_c}{4\pi R^2} = \frac{D_c \times 8.20 \times 10^9}{KG_c}$$

where D_c and R are in centimeters.

The photometer was mounted on a post with motion in the azimuth and zenith directions. Each motion was coupled to a potentiometer battery arrangement and the outputs were fed to a second channel of the recorder through a motor-driven commutator. These position indicators were calibrated in the field. Relative azimuth and zenith angles could be read to within a degree or so (over a range of perhaps 15°), but their absolute value could not be determined within 4° or 5°.

DATA ACQUISITION AND REDUCTION

Data were taken in the field by pointing the photometer at a specific portion of the cloud with open sights alined with the photometer's optical axis. One observer pointed and a second examined the pen recording and adjusted gain if necessary. When a satisfactory gain was assured the first observer checked his pointing, then pressed a button which actuated a side pen on the recorder to indicate the time that proper pointing was obtained. The first observer also verbally transmitted pointing information which the second observer wrote on the chart as well as the gain settings used. Pointing positions were selected along the visual line occupied by the barium ions and included points above the top, at the top, through the middle portion, at the bottom, and below the bottom of the cloud. No indication of the instrument's field of view had been built into the sight arrangements. After reducing the data it was apparent that many more observations were taken than were necessary due to the rather large field angle of the photometer. Time was recorded occasionally along the chart, and the synchronous drive allowed interpolation.

Field filling factors K[1] were determined from a set of negatives from a 4554 Å filtered, K-24 camera from Coquina Beach supplemented with longer exposure negatives from an unfiltered 35-mm camera operated at Coquina Beach. By using Castor, Pollux, and Jupiter, azimuth and zenith positions were established for the upper and lower points of the cloud as it appeared in the photographic image for the Javelin second release. In

---

[1]The field filling factor K is defined as measured flux divided by total flux. Estimates of K were made by determining cloud positions from photographs through a 4554 Å filter (making due allowance for brightness variation), mapping this information on a plane perpendicular to the photometer's optical axis, and noting the fraction of the cloud within the photometer's field of view.

some cases the photometer's field of view was larger than the cloud. This condition prevailed during the first 40 or so seconds after release. Some 1500 seconds after release the length was again comparable to the field of view. At no time was the cloud longer than about 4 times the field angle (K = 1/4).

RESULTS

The values given in table VII-I for the Javelin second release during the period from 296 seconds to 736 seconds are subject to the greatest uncertainty in view of the small values of the field filling factor K. Previous experiments gave every expectation that the ionization process will be essentially complete and the ionized cloud itself will be optically thin after the lapse of about 1 minute. In order to arrive at an estimate of ionization efficiency it was decided to use a peak value for the photon flux of 1.7×10^6 photons/cm^2/sec, which is the value measured at 58 seconds after release. In the first minute of cloud expansion, the cloud center is subject to so little displacement that one can safely take as the mean range from Coquina Beach the value corresponding to the release itself, 1100 km. Then if a value of atmospheric transmissions is taken as 0.7, which corresponds to a wavelength of 4554 Å and an elevation of about 50°, the number of photons per second would be $\dfrac{(1.7 \times 10^6)4\pi(1100 \times 10^5)^2}{0.7}$ or 3.7×10^{23}. By taking an excitation factor at 4554 Å of 0.655 photons/ion/sec, the number of barium ions formed would be $\dfrac{3.7 \times 10^{23}}{0.655}$ or 5.65×10^{23}. The value 0.655 is based on an assumed oscillator strength of 0.66, a mean solar spectral flux in proximity of 4554 Å of 262 ergs-cm^{-2}-sec^{-1}-Å^{-1}, and a residual-line strength of the Fraunhofer absorption line of 9 percent. Thus, the mass of ionized barium formed is 128 grams and the overall yield of payload, which is the mass of the ionized barium cloud divided by the total mass of the chemical mixture, would be $\dfrac{128}{12\ 000}$ or 1.06 percent.

REFERENCES

VII-1. Dunn, R. B.; and Manring, E. R.: Recording Night Sky Photometer of High Spectral Purity. J. Opt. Soc. Amer., vol. 46, no. 8, Aug. 1956, pp. 572-577.

VII-2. Minnaert, M.; Mulders, G. F. W.; and Houtgast, J.: Photometric Atlas of the Solar Spectrum. D. Schnabel, Amsterdam, 1940.

TABLE VII-I.- PHOTON FLUX AT 4554 Å FROM IONIZED CLOUDS

AS A FUNCTION OF TIME

Release	Time from release, sec	Measured flux, photons/cm^2/sec	Field filling factor, K	Total flux, photons/cm^2/sec
Javelin				
First	53	7.1×10^5	1	7.1×10^5
	1083	2.3	Uncertain	2.3/K
	1521	2.7	Uncertain	2.7/K
Second	31	1.4×10^6	1	1.4×10^6
	58	1.7	1	1.7
	111	1.3	.8	1.6
	296	.6	.3	1.9
	421	.7	.35	2.1
	736	.8	.4	2.0
	1306	1.8	.8	2.2
	1786	1.9	1	1.9
	2356	1.7	1	1.7
	2756	1.5	[a]1	1.5
Nike-Tomahawk				
First	28	5.7×10^5	1	5.7×10^5
	178	6.4	1	6.4
Second	30	9.0×10^6	1	9.0×10^6
	135	9.7	1	9.7
Third	31	18×10^6	1	18×10^6
	151	29	1	29

[a]Probably 1, pointing uncertain.

VIII. NASA OPTICAL INSTRUMENTATION

By Kenneth H. Crumbly
NASA Langley Research Center

OPTICAL-SITE LOCATION

The Langley Research Center in conjunction with the NASA Wallops Station operated six different sites for each mission. These sites along with their latitude and longitude are given in table VIII-I. A map showing the locations of these sites, with the exception of Bermuda, is shown as figure II-4. At Wallops Station two locations were used, one near the SPANDAR radar and designated "(S)" in the table, and the other at the north end of Wallops Island and designated "(N)" in the table. Cameras were placed at both of these sites for both missions.

TABLE VIII-I.- LOCATION OF OPTICAL SITES

Site	Latitude, ^{O}N	Longitude, ^{O}W
Back Bay, Va.	36.676	75.916
Bermuda, U.K.	32.346	64.652
Coquina Beach, N.C.	35.846	75.565
Eastville, Va.	37.350	75.900
Wallops Island, Va. (N)	37.867	75.451
Wallops Island, Va. (S)	37.856	75.512

OPTICAL INSTRUMENTATION PLAN AT EACH SITE

The optical instrumentation plan at each site is summarized as follows:

Back Bay — The plan for data coverage from Back Bay called for triangulation data, filter data, and medium-resolution photographs. At this site the following cameras were used:

One BC-4 camera (Serial 259)

Two modified K-24 cameras

One modified K-24 camera with filter, 4554 Å

One modified K-24 camera with filter, 5535 Å

One K-24 camera with filter, 4554 Å

One K-24 camera with filter, 5535 Å

Bermuda — The data coverage from Bermuda called for triangulation data to be used in conjunction with any of the mainland sites which were similarly equipped. Therefore, two of the modified K-24 cameras without filters were placed on the island.

Coquina Beach — The data coverage from Coquina Beach called for triangulation data, filter data, and medium-resolution photographs. At this site the following cameras were used:

> One BC-4 camera (Serial 272)
>
> Two modified K-24 cameras
>
> One modified K-24 camera with filter, 4454 Å
>
> One modified K-24 camera with filter, 5535 Å
>
> One PE 610 camera

Eastville — The data coverage from Eastville called for short-duration exposure, medium-resolution photographs. At this site a Smithsonian Astrophysical Observatory Super-Schmidt camera was used.

Wallops Island — The data coverage from Wallops Island called for triangulation data, medium-resolution photographs — both long duration and short duration. The cameras were placed at two different locations. At the SPANDAR radar site were the Super-Schmidt and two modified K-24 cameras without filters. At the north camera site were one BC-4 (Serial 273) and two PE 1220 cameras.

DESCRIPTION OF CAMERAS

The cameras which were used for these missions are modified Air Force aerial cameras, precision ballistic cameras, and special purpose cameras. A general description of these cameras and filters is as follows:

Description

BC-4	A precision metric camera of focal length 304 mm; f/2.6; uses a glass plate 190 mm × 210 mm × 6.4 mm; has an external capping shutter and an internal, between-the-lens, rotating shutter; has lighted fiducial marks and a clock capable of being exposed on the film plate; field of view in azimuth is 34° and in elevation is 38°.

Description

K-24
Originally an Air Force aerial camera of nominal focal length 178 mm; f/2.5; uses a roll film 5 inches (127 mm) wide in a magazine holding up to 56 feet (17 m) of film; has a focal-plane shutter. Exposure time is determined by the width of the slit in the shutter curtain; shutter and film advance can be accomplished either manually or electrically by remote control; nonlighted fiducial marks are inscribed on a glass film platen; approximate field of view in azimuth and elevation is 39°.

Modified K-24
A basic K-24 camera modified to add special features as follows:

a. Programer – Equipped with a mechanical programer using mylar tape to take a series of variable-duration exposures at specific time intervals; added a camera data box and lighted fiducials.

b. Filters – Equipped with an interference filter placed before the objective lens to admit only light in a certain bandwidth.

PE 610
Originally an Air Force aerial camera of nominal focal length 610 mm; f/3.5; uses a glass plate 457 mm × 457 mm × 6.4 mm; has neither internal nor external shutter; has neither time nor fiducial marks; field of view is approximately 41° in azimuth and elevation.

PE 1220
A camera similar to the PE 610 of nominal focal length 1220 mm; f/6.3; uses a glass plate 203.4 mm × 254.0 mm × 1.6 mm; has neither an internal nor an external shutter; has neither time nor fiducial marks; approximate field of view is 5°30' in azimuth and 12° in elevation.

Super-Schmidt
A high-speed, wide-field camera of focal length 203.2 mm; f/0.85; uses a molded film, hemisphere shaped, approximately a 200-mm radius of curvature; angular field of view is approximately 55°. These cameras are permanently mounted at Wallops and Eastville, Virginia, on equatorial mounts.

Filters
a. Optical interference with a peak wavelength of 5535 Å, 1/2 bandwidth 45 Å; 1/10 bandwidth 75 Å, transmission ≈ 70 percent.

b. Identical to the filter just described except that the peak wavelength is 4554 Å.

OBSERVATIONAL CONDITIONS

In general, the observational conditions were good for both missions, although not excellent. Mission requirements were that the sites at Wallops Island and Coquina Beach should be clear (since this provided a good baseline for triangulation). In the early part of the launch window the site at Back Bay was consulted for any local variations that would be a detriment to the collection of data. Also, the site at Bermuda would not be in a favorable geographical position if the launch occurred just before dawn. Weather conditions delayed both launches until the latter part of the September launch window. This delay forced an early morning launch, and, as a result, the Bermuda site obtained no useful data on either the Javelin or the Nike-Tomahawk launch.

Javelin

The Javelin was launched September 24, 1966. All sites, with the exception of Back Bay, were reporting good seeing conditions. The site at Back Bay had some cumulus clouds low and to the northeast. This site did encounter some cloud movement across the field of view of the cameras after the release. The data collected from this site had some time periods in which part of the ionized cloud was obscured.

Nike-Tomahawk

The Nike-Tomahawk was launched September 25, 1966. Again, the seeing conditions were good. Shortly before launch time the Wallops sites reported the advent of clouds moving into the area and after consultation with Back Bay personnel, who reported clear weather, the decision was made to launch the rocket. As a result, the data from Wallops Island covers only the first few minutes of the release. Afterwards, except for brief breaks in the cloud cover, this site could only see the vague outline of the cloud. The decision to launch was influenced by the fact that this was the last day of the September launch window.

DATA OBTAINED

Table VIII-II summarizes the data collected during the several releases. The absence of certain data and the fact that only partial data were obtained at some sites may be noted by reading the preceding section on observational conditions. Also, there were some mechanical failures at different locations which caused the data collected to be deficient in some way. For example, some of the K-24 cameras had a data box containing an interval counter, a clock, and a nameplate with the site location. If the counter

or clock did not work properly then the data contained on this film is called partial. In planning the experiment, some redundancy was introduced, especially in the triangulation cameras, to offset possible camera malfunction.

TABLE VIII-II.- DATA COLLECTED FOR JAVELIN

AND NIKE-TOMAHAWK LAUNCHES

[Langley Support]

Site	Camera[a]					
	Modified K-24 triangulation	K-24 with filter, 4554 Å	K-24 with filter, 5535 Å	BC-4	Super- Schmidt	PE 610, PE 1220
Javelin						
Back Bay	++	++	++	++		
Bermuda	0					
Coquina Beach	++	++	0	0		0
Eastville					++	
Wallops Island (N)				++		0
Wallops Island (S)	++				++	
Nike-Tomahawk						
Back Bay	+	++	++	++		
Bermuda	0					
Coquina Beach	++	++	++	++		++
Eastville						
Wallops Island (N)				0		0
Wallops Island (S)	0				+	

[a]Data quality:

   ++   Good

    +   Partial

    0   None

Page intentionally left blank

IX. TRIANGULATION

By C. G. Justus, A. Woodrum, and W. B. Moseley
School of Aerospace Engineering,
Georgia Institute of Technology

INTRODUCTION

In this report the results of the triangulation studies of the barium releases of September 24 and 25, 1966, are discussed. Data presented include position of the neutral clouds, position and motion of the Javelin ionized cloud, and radial growth of the neutral clouds. The position data include slant ranges from the camera sites.

DATA-REDUCTION METHODS

Star backgrounds are used to determine camera focal length, azimuth, elevation, and tilt. The procedures used for this purpose are presented in reference IX-1. A list of computed camera focal length and azimuth, elevation, and tilt angles is presented as table IX-I. Computerized triangulation techniques are used to calculate positions of the center of the neutral clouds and points on the center line of the ionized clouds. These techniques are discussed in reference IX-2.

Accurate times for the exposures are needed for computing camera look angles and for determining time differences for use in the calculation of cloud motion. All times are given with respect to the launch time of the rockets. The Javelin launch time was 9 hours 13 minutes UT on September 24 and the Nike-Tomahawk launch time was 9 hours 51 minutes UT on September 25. Times associated with the position data correspond to the midpoint of the exposure time for the film frames which were used to compute the cloud position.

In order to compute trail positions (such as for the stretched-out ionized clouds) it was necessary to mark and number dots along the center line of the trail image on two or more synchronized frames from different sites. These points are at arbitrary locations along the trail, and a given point number will not necessarily correspond from site to site or time to time with the same altitude or location in space. Thus a set of positions can be calculated for each site which is used, and the calculated position data will apply only to the points as marked on the film from that site. The position-data output includes height, geographic (or geodetic) latitude and longitude of the points, as well as the slant range (direct straight-line distance) from the site to the point on the cloud. (The reference ellipsoid used in determining geographic latitudes is discussed in ref. IX-2.)

The position data from each site may be interpolated to any set of convenient altitudes, and these interpolated position data may be averaged to give a mean position curve for the cloud at each time. At each interpolation altitude, the time rate of change of the north-south position component and east-west position component may be used to determine the northward and eastward motion. Motions are considered positive if directed toward the north or east.

POSITION DATA

Table IX-II gives the computed position data for the neutral cloud release positions for the three Nike-Tomahawk releases and for the two Javelin releases. Possible errors are about 0.5 km in the height and slant ranges and 0.002^O in the latitude and longitude for the first Nike-Tomahawk release and the first Javelin release. For the other releases the errors were about 10 km and 0.05^O. The large possible errors are due to the large fuzzy cloud images which had to be used in calculating cloud center-point position. The positions of Nike-Tomahawk neutral clouds from the second and third releases did not vary significantly during their lifetimes, and the positions shown are an average over all times that those clouds were observed. The 10-km position error represents an rms deviation of all the position data for these two releases.

Table IX-III gives the computed positions of the ionized cloud from the Javelin first release for 716 sec and 936 sec after release since these were the times for which photographs were adequate for data reduction. For these times positions are given of the points as numbered[1] on the film from exposures taken at Wallops Island (S) and Back Bay, Virginia. (See fig. II-4 for location of tracking sites.)

Tables IX-IV(a), (b), and (c) show the computed positions for the ionized cloud from the Javelin second release, as viewed from Wallops (S), Back Bay, and Coquina Beach, respectively.

INTERPOLATED POSITION DATA AND IONIZED CLOUD MOTION

Table IX-V shows the computed average interpolated position data for the ionized cloud from the Javelin second release. From these tabulated data,[2] figures IX-1 and IX-2 have been prepared showing the center line of the second ion cloud as a function of time, in the form of plots of altitude against northern latitude and western longitude, respectively.

---

[1]The numbering of points as they appear in tables IX-III and IX-IV is arbitrary and was used only in data reduction. Thus, there is no correlation between points correspondingly numbered at the same time, but taken at different sites.
[2]The data corresponding to a time of 1450 sec are taken from tables IX-IV(a) and (c).

Cloud horizontal motions may be determined by computing the rate of change of position of the interpolated data at each of the interpolation altitudes. Table IX-VI and figure IX-3 show the computed horizontal motion of the ionized clouds from both of the Javelin releases. Since both releases were in the same general area, it is likely that they were subject to the same drift motions and, hence, it was believed justified to incorporate both sets of data in the same plot. Probable errors are about 5 m/sec for the motion of the first release. The position data show that the ionized clouds are stretched along the magnetic-field lines but seem to have a predominantly westward horizontal motion.

Figure IX-4 is a graph of the altitudes corresponding to the upper and lower extremities[3] of the ionized cloud from the second Javelin release as a function of time. The two lines drawn through the extremities of the ionized cloud intersect at the release point (951 km altitude, 564 sec after launch). The upward growth is not as rapid as the downward growth. However, at long times after release, most of the visible material has concentrated at the lower altitudes near 200 km. Since figure IX-4 shows that no visible ionized material fell below 200 km, this may be the altitude region at which strong coupling exists between the motions of the neutral and ionized constituents.

Table IX-VII and figures IX-5 and IX-6 show the growth data for the neutral clouds. A good approximation to the actual diameter D_C of the cloud can be obtained from the relation $D_C = \frac{dR}{f}$ where d is the measured cloud diameter on the film, R is the range (from the position tables), and f is the focal length from table IX-I. The second release from the Javelin is the only one which exhibits a near-constant growth rate (≈ 2 km/sec). The other clouds exhibit time-varying growth rates similar to the parabolic growth curves (ref. IX-2) for molecular diffusion. If it is assumed that the Nike-Tomahawk neutral clouds expanded at a rate such that $D_C^2 = 16Dt$,[4] where D is the molecular diffusion coefficient and t is the time after release, then $D \approx 3 \times 10^5$ m^2/sec for the first release and $D \approx 1.6 \times 10^6$ m^2/sec for the second and third releases.

The error bars in figures IX-5 and IX-6 indicate the variability of diameter measurements from different sites. The scatter of the data points is due to variability introduced by different exposure times, changing sky background, and other parameters.

---

[3]The identification of the cloud extremities from which the cloud positions are computed is subjective since the image of the cloud decreases into the background density of the film.

[4]This relation is used under the assumption that the standard deviation σ of the cloud distribution increases as $\sigma^2 = 4Dt$ and that the observed cloud diameter is approximately 2σ.

REFERENCES

IX-1. Justus, C. G.; Edwards, H. D.; and Fuller, R. N.: A Method Employing Star Backgrounds for Improving the Accuracy of the Location of Clouds or Objects in Space. Photogram. Eng., vol. XXX, no. 4, July 1964, pp. 594-607.

IX-2. Justus, C. G.; Edwards, H. D.; and Fuller, R. N.: Analysis Techniques for Determining Mass Motions in the Upper Atmosphere From Chemical Releases. AFCRL-64-187, U.S. Air Force, Jan. 1964. (Available from DDC as AD 435 678.)

TABLE IX-I.- COMPUTED CAMERA FOCAL LENGTH AND

CENTER-OF-FRAME ORIENTATION

| Release | Release time, sec after launch | Camera | | Center-of-frame data | | | |
		Location	Focal length, cm	Time interval valid, sec (a)	Azimuth angle, $^{\circ}$E of N	Elevation angle, deg	Tilt angle, deg (b)
				Javelin			
First	224	Wallops Island (S)	18.17	221 to 240 637 to 1160 2014	89.01 102.48 85.92	51.74 51.86 31.72	+0.30 +.31 +.23
Second	564	Back Bay	18.16	637 to 1160	^{c}81	^{c}46	+4.4
		Coquina Beach	18.19	637 to 1160 2014	76.41 60.55	48.95 22.97	+3.16 +1.89
				Nike-Tomahawk			
First	138	Wallops Island (S)	18.17	175 to 556	135.43	65.95	+0.80
Second	205	Back Bay	18.18	175 to 556	80.27	60.84	+3.69
Third	339	Coquina Beach	18.12	175 to 196 230 to 267 350 to 556	33.87 26.66 57.58	49.56 59.93 60.26	-1.19 -2.62 +1.33

^{a}Time measured from launch.

^{b}Positive tilt angle corresponds to clockwise relation.

^{c}Fiducial marks did not show up, hence center of frame could not be given more accurately.

TABLE IX-II.- COMPUTED RELEASE-POSITION DATA

Position component	Javelin		Nike-Tomahawk		
	Release		Release		
	First	Second	First	Second	Third
Height, km	515.8	951	218.6	277	264
Latitude, ^{O}N	37.299	35.81	37.432	37.16	36.71
Longitude, ^{O}W	72.722	67.09	75.043	74.81	74.38
Range to Wallops Island (S), km	579.7	1270	227.8	299	316
Range to Back Bay, km	598.7	1280	286.1	300	301
Range to Coquina Beach, km	(a)	1280	252.1	316	294

[a]No data on Javelin first release were obtained at Coquina Beach.

TABLE IX-III.- COMPUTED POSITIONS OF SELECTED POINTS

ON IONIZED CLOUD CENTER LINE FOR

JAVELIN FIRST RELEASE

Time after release, sec	Point	Height, km	Latitude, ^{o}N	Longitude, ^{o}W	Range, km
(a) Wallops Island (S) site					
716	52	377	37.74	73.32	426
	53	394	37.68	73.31	443
936	51	343	37.85	73.50	388
	52	364	37.78	73.47	408
	53	380	37.72	73.47	423
(b) Back Bay site					
716	50	361	37.77	73.34	448
	51	378	37.73	73.32	462
	52	393	37.68	73.31	474
936	50	334	37.89	73.49	423
	51	344	37.84	73.50	429
	52	361	37.79	73.47	443
	53	372	37.74	73.49	450
	54	389	37.69	73.46	464
	55	407	37.65	73.43	479

TABLE IX-IV.- COMPUTED POSITIONS OF SELECTED POINTS ON IONIZED CLOUD CENTER LINE FOR JAVELIN SECOND RELEASE

(a) Wallops Island (S) site

Time after release, sec	Point	Height, km	Latitude, °N	Longitude, °W	Range, km
73	1	730	36.70	68.14	1014
	2	756	36.61	68.12	1036
	3	785	36.50	68.12	1061
	4	824	36.37	68.10	1095
	5	882	36.20	68.06	1151
	6	930	36.05	67.97	1195
	7	982	35.87	67.94	1244
	8	1025	35.69	67.95	1284
176	2	643	36.92	68.39	929
	3	686	36.80	68.30	969
	4	732	36.66	68.25	1009
	5	788	36.50	68.14	1062
	6	816	36.35	68.23	1082
	7	849	36.20	68.30	1107
	8	912	36.03	68.16	1171
	9	997	35.77	67.98	1256
	10	1048	35.55	68.05	1301
251	1	603	37.07	68.34	902
	2	638	36.97	68.31	930
	3	676	36.83	68.31	960
	4	706	36.71	68.34	982
	5	726	36.60	68.42	995
	6	766	36.48	68.36	1032
	7	815	36.33	68.27	1079
	8	874	36.14	68.23	1133
	9	932	35.94	68.16	1189
	10	971	35.76	68.25	1221
	11	1096	35.45	67.86	1354

TABLE IX-IV.- COMPUTED POSITIONS OF SELECTED POINTS ON IONIZED

CLOUD CENTER LINE FOR JAVELIN SECOND RELEASE – Continued

(a) Wallops Island (S) site – Concluded

Time after release, sec	Point	Height, km	Latitude, °N	Longitude, °W	Range, km
376	1	451	37.56	68.57	778
	2	479	37.47	68.56	797
	3	513	37.36	68.53	823
	4	554	37.25	68.41	860
	5	577	37.14	68.49	871
	6	615	37.01	68.45	903
	7	646	36.89	68.46	927
	8	688	36.76	68.42	963
	9	740	36.59	68.33	1011
	10	798	36.42	68.22	1067
	11	847	36.23	68.23	1109
	12	900	36.04	68.22	1157
	13	987	35.78	68.06	1244
	14	1049	35.55	68.08	1300
	15	1124	35.29	68.05	1373
596	3	437	37.50	68.96	741
	4	469	37.41	68.85	770
	5	515	37.31	68.64	816
	6	548	37.18	68.64	840
	7	584	37.06	68.61	869
	8	630	36.93	68.51	911
	9	657	36.81	68.55	930
	10	709	36.66	68.42	981
	11	755	36.51	68.35	1023
	12	798	36.34	68.37	1059
	13	839	36.21	68.36	1095
	14	888	36.01	68.37	1139
	15	952	35.80	68.29	1202
	16	1028	35.54	68.23	1274
	17	1119	35.25	68.13	1365
	18	1229	34.89	68.02	1476
	19	1298	34.61	68.04	1544
1450	5	216	38.23	69.45	584
	6	232	38.19	69.41	594
	7	246	38.14	69.42	598
	8	261	38.08	69.42	605
	9	278	38.02	69.41	614
	10	300	37.97	69.33	632
	11	323	37.90	69.27	649

TABLE IX-IV.- COMPUTED POSITIONS OF SELECTED POINTS ON IONIZED

CLOUD CENTER LINE FOR JAVELIN SECOND RELEASE — Continued

(b) Back Bay site

Time after release, sec	Point	Height, km	Latitude, ^{o}N	Longitude, ^{o}W	Range, km
73	2	762	36.58	68.15	1059
	3	804	36.44	68.10	1094
	4	851	36.29	68.05	1135
	5	899	36.14	68.02	1177
	6	947	35.98	68.00	1218
	8	1057	35.60	67.88	1321
	9	1104	35.44	67.84	1365
176	1	612	37.04	68.33	936
	2	642	36.93	68.40	952
	3	685	36.81	68.30	990
	4	729	36.68	68.24	1028
	5	776	36.53	68.16	1069
	6	814	36.36	68.22	1095
	7	864	36.19	68.22	1136
	8	950	35.98	67.96	1223
	9	982	35.79	68.07	1244
	10	1035	35.59	68.06	1292
251	4	631	36.98	68.34	949
	5	675	36.83	68.33	981
	6	716	36.68	68.33	1012
	7	761	36.50	68.36	1045
	8	819	36.31	68.28	1096
	9	896	36.10	68.14	1167
	10	951	35.88	68.12	1216
	11	1014	35.68	68.07	1272

TABLE IX-IV.- COMPUTED POSITIONS OF SELECTED POINTS ON IONIZED

CLOUD CENTER LINE FOR JAVELIN SECOND RELEASE – Continued

(b) Back Bay site – Concluded

Time after release, sec	Point	Height, km	Latitude, $^{\circ}$N	Longitude, $^{\circ}$W	Range, km
376	6	479	37.47	68.56	835
	7	513	37.33	68.57	855
	8	553	37.22	68.51	884
	9	593	37.10	68.46	914
	10	645	36.93	68.40	955
	11	698	36.76	68.33	999
	12	751	36.57	68.28	1042
	13	819	36.36	68.18	1102
	14	868	36.19	68.18	1141
	15	944	35.97	68.01	1215
	16	1008	35.73	67.99	1271
	17	1078	35.52	67.95	1335
	18	1155	35.28	68.86	1409
	19	1217	35.04	67.81	1469
596	4	439	37.49	68.96	781
	5	471	37.40	68.84	808
	6	506	37.33	68.69	840
	7	538	37.22	68.60	867
	8	565	37.12	68.65	881
	9	601	37.01	68.57	911
	10	635	36.90	68.55	937
	11	680	36.74	68.49	973
	12	726	36.60	68.40	1014
	13	779	36.42	68.35	1058
	14	821	36.26	68.28	1091
	15	851	36.14	68.41	1114
	16	910	35.94	68.33	1168
	17	962	35.77	68.30	1215
	18	1017	35.57	68.25	1266
	19	1076	35.38	68.19	1322
	20	1136	35.19	68.12	1380
	21	1203	34.97	68.05	1445
	22	1253	34.76	68.11	1490
	23	1344	34.46	68.00	1582

TABLE IX-IV.- COMPUTED POSITIONS OF SELECTED POINTS ON IONIZED

CLOUD CENTER LINE FOR JAVELIN SECOND RELEASE – Concluded

(c) Coquina Beach site

Time after release, sec	Point	Height, km	Latitude, °N	Longitude, °W	Range, km
176	1	669	36.85	68.32	963
	2	702	36.75	68.28	989
	3	739	36.65	68.21	1020
	4	790	36.49	68.14	1063
	5	821	36.33	68.23	1081
	6	870	36.18	68.17	1124
	7	926	36.02	68.05	1176
	8	980	35.81	68.06	1221
	9	1036	35.60	68.06	1269
251	1	618	37.01	68.37	925
	2	652	36.89	68.40	945
	3	693	36.76	68.32	980
	4	730	36.63	68.30	1007
	5	762	36.50	68.34	1029
	6	802	36.35	68.34	1060
	7	875	36.17	68.12	1130
	8	932	35.96	68.12	1177
	9	982	35.77	68.12	1219
	10	1061	35.54	67.96	1296
376	4	499	37.37	68.63	833
	5	530	37.28	68.59	853
	6	558	37.18	68.58	872
	7	600	37.08	68.41	911
	8	640	36.95	68.36	940
	9	685	36.82	68.28	977
	10	725	36.68	68.26	1007
	11	766	36.52	68.26	1037
	12	824	36.35	68.14	1089
	13	869	36.19	68.13	1125
	14	917	36.02	68.13	1165
	15	993	35.80	67.97	1237
	16	1054	35.59	67.94	1291
	17	1138	35.36	67.77	1374
	18	1197	35.11	67.80	1425
	19	1250	34.92	67.80	1473
1450	7	229	38.20	69.42	657
	8	241	38.15	69.42	660
	9	258	38.09	69.43	664
	10	275	38.03	69.41	670
	11	291	37.99	69.37	679
	12	312	37.94	69.29	693
	13	327	37.89	69.27	701

TABLE IX-V.- COMPUTED AVERAGE INTERPOLATED POSITION DATA FOR IONIZED CLOUD FROM JAVELIN SECOND RELEASE

Time after release, sec	Height, km	Latitude, °N	Longitude, °W
73	750	36.633	68.124
	800	36.451	68.111
	850	36.292	68.053
	900	36.137	68.015
	950	35.973	67.979
	1000	35.796	67.944
	1050	35.622	67.887
	1100	35.458	67.840
176	650	36.904	68.378
	700	36.759	68.282
	750	36.614	68.198
	800	36.431	68.175
	850	36.232	68.220
	900	36.086	68.134
	950	35.941	68.026
	1000	35.736	68.041
251	650	36.911	68.346
	700	36.736	68.323
	850	36.225	68.219
	900	36.085	68.126
	950	35.888	68.126
	1000	35.716	68.089
	1050	35.561	68.006
376	500	37.384	68.581
	550	37.231	68.507
	600	37.073	68.446
	650	36.896	68.425
	700	36.716	68.400
	750	36.573	68.285

TABLE IX-V.- COMPUTED AVERAGE INTERPOLATED POSITION DATA

FOR IONIZED CLOUD FROM JAVELIN SECOND RELEASE – Concluded

Time after release, sec	Height, km	Latitude, $^{\circ}$N	Longitude, $^{\circ}$W
376	800	36.418	68.203
	850	36.222	68.230
	900	36.061	68.176
	950	35.908	68.088
	1000	35.736	68.057
	1050	35.582	67.997
	1100	35.428	67.943
	1150	35.304	67.818
	1200	35.107	67.811
	1250	34.917	67.802
596	450	37.460	68.960
	500	37.318	68.739
	550	37.158	68.628
	600	37.018	68.551
	650	36.845	68.490
	700	36.688	68.442
	750	36.522	68.400
	800	36.358	68.364
	850	36.172	68.341
	900	35.992	68.309
	950	35.825	68.278
	1000	35.645	68.241
	1050	35.478	68.208
	1100	35.325	68.171
	1150	35.152	68.142
	1200	34.981	68.103
	1250	34.802	68.068
	1300	34.602	68.032
	1350	34.400	68.000

TABLE IX-VI.- COMPUTED HORIZONTAL MOTION OF IONIZED

CLOUDS FROM JAVELIN RELEASES

Height, km	Duration of observation, sec	Southward motion, m/sec	Westward motion, m/sec	Horizontal speed, m/sec	Heading, °E of N
First release					
360	220	-9 ± 5	63 ± 5	64	278
370	220	2 ± 5	66 ± 5	66	268
380	220	2 ± 5	66 ± 5	66	268
390	220	1 ± 5	63 ± 5	63	269
400	220	-4 ± 5	59 ± 5	59	274
Second release					
500	220	26 ± 6	61 ± 14	66	247
550	220	29 ± 12	53 ± 26	60	241
600	220	30 ± 5	49 ± 9	57	239
650	420	27 ± 4	48 ± 9	55	241
700	420	24 ± 2	48 ± 3	54	243
750	523	25 ± 2	49 ± 5	55	243
800	523	26 ± 2	50 ± 3	56	242
850	523	28 ± 4	52 ± 9	59	242
900	523	32 ± 4	54 ± 8	63	239
950	523	36 ± 5	57 ± 8	67	238
1000	523	40 ± 6	60 ± 8	72	236
1050	523	45 ± 13	66 ± 21	80	235
1100	523	50 ± 19	74 ± 30	89	236

TABLE IX-VII.- DIAMETER OF NEUTRAL CLOUDS

Javelin		Nike-Tomahawk					
Second release		First release		Second release		Third release	
Time after release, sec	Diameter, km	Time after release, sec	Diameter, km	Time after release, sec	Diameter, km	Time after release, sec	Diameter, km
19	45	3	6.3 ± 2.0	10	16.5 ± 2.8	29	33 ± 8
31	73 ± 5	18	11.6 ± 0.7	43	47.2 ± 0.6	34	39 ± 2
53	108 ± 20	51	15.2 ± 0.4	48	40.6 ± 4.4	42	42 ± 4
95	168 ± 18			76	44.8 ± 1.0	56	43 ± 8
				90	51.3 ± 1.1	89	52 ± 3
				103	56.9 ± 1.7	94	42 ± 5
				108	38.7 ± 0.3	102	49 ± 5
				123	44.0 ± 0.4	116	54 ± 5
				138	49.0 ± 4.2	149	48 ± 13
				163	64.3	154	47 ± 5
						162	54 ± 5
						176	57 ± 6
						209	58 ± 6
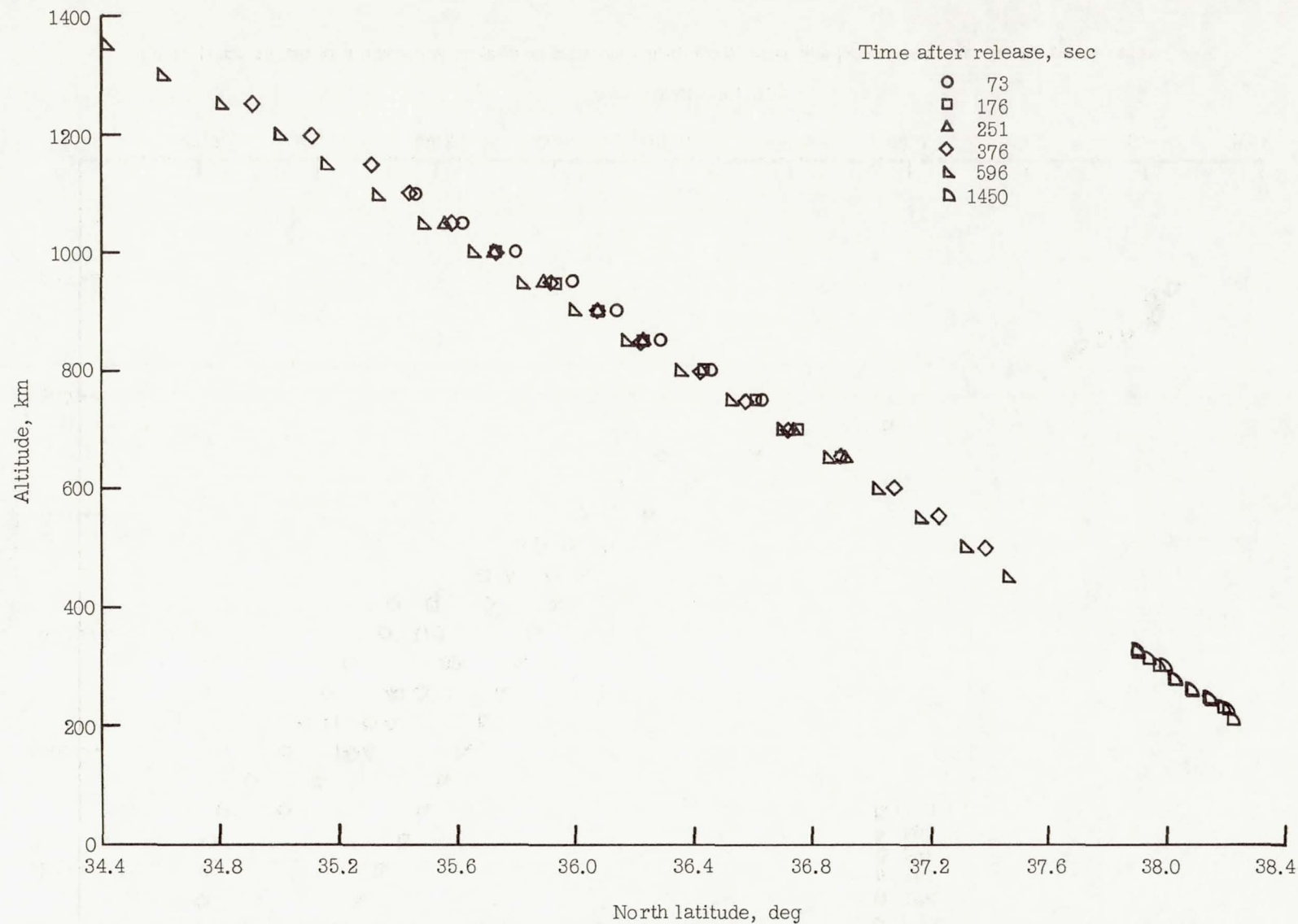
Figure IX-1.- Altitude as a function of latitude of points on ionized cloud center line for various times. Javelin second release.
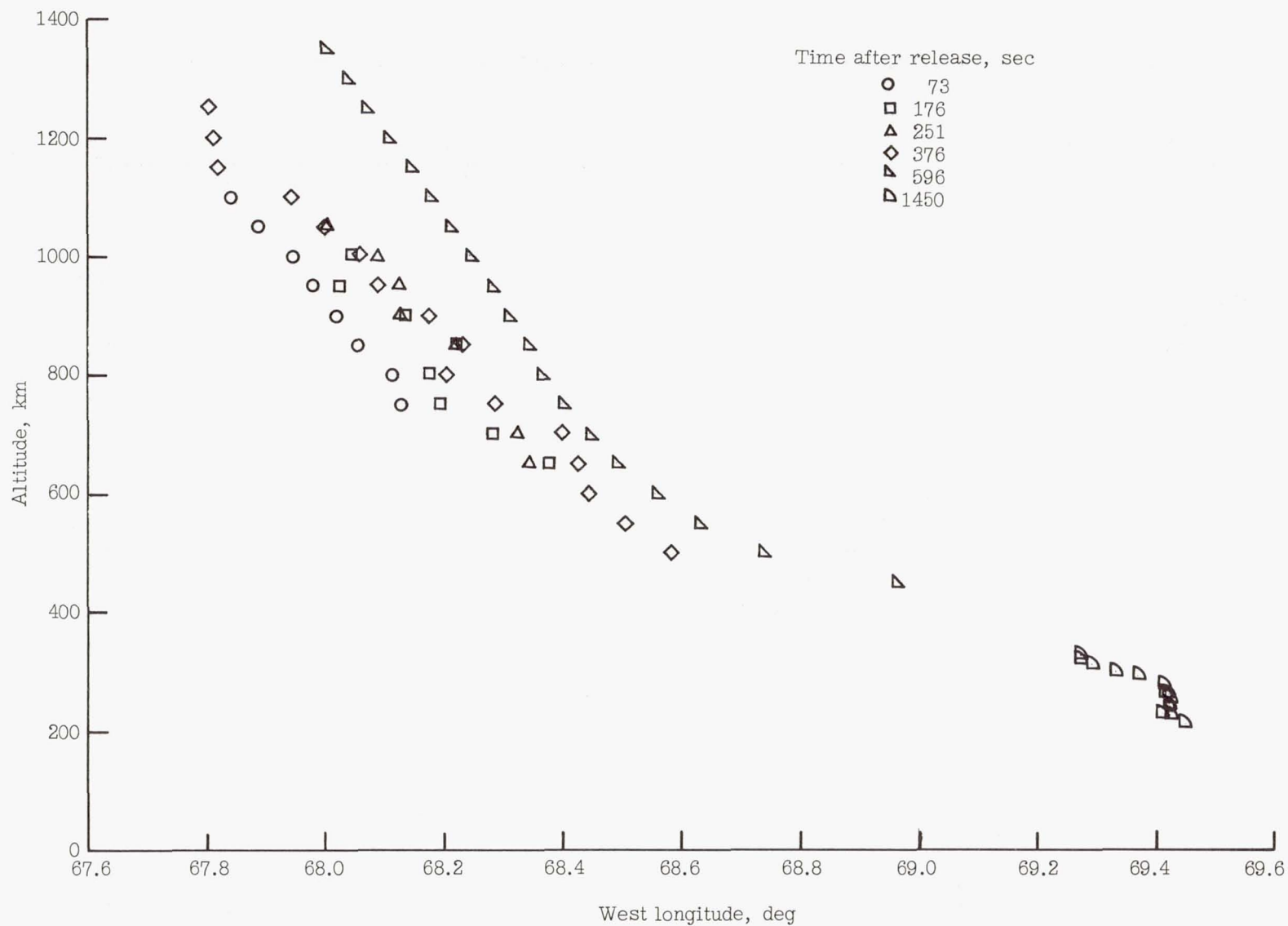
Figure IX-2.- Altitude as a function of longitude of points on ionized cloud center line for various times. Javelin second release.
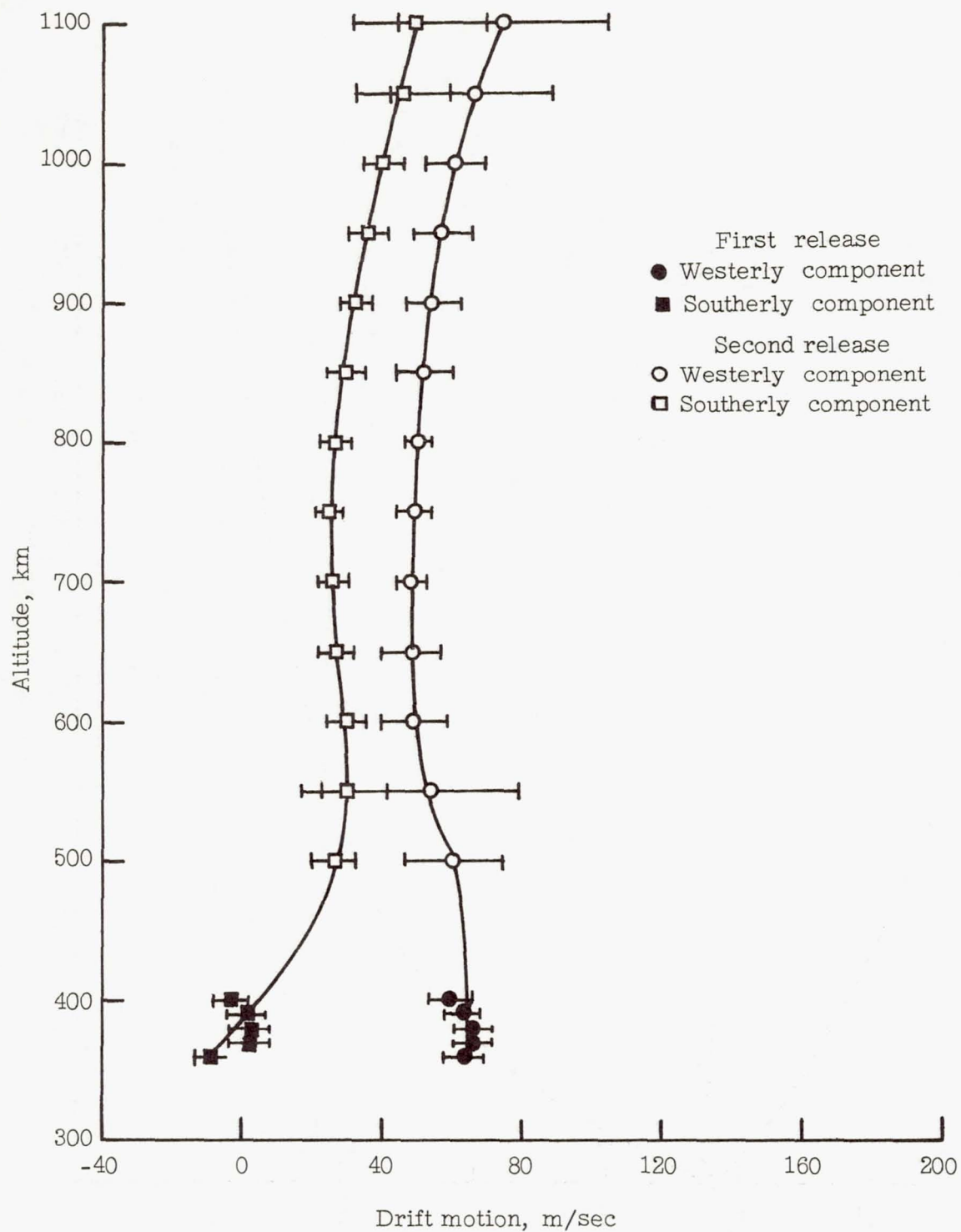
Figure IX-3.- Components of ionized cloud drift at various altitudes.
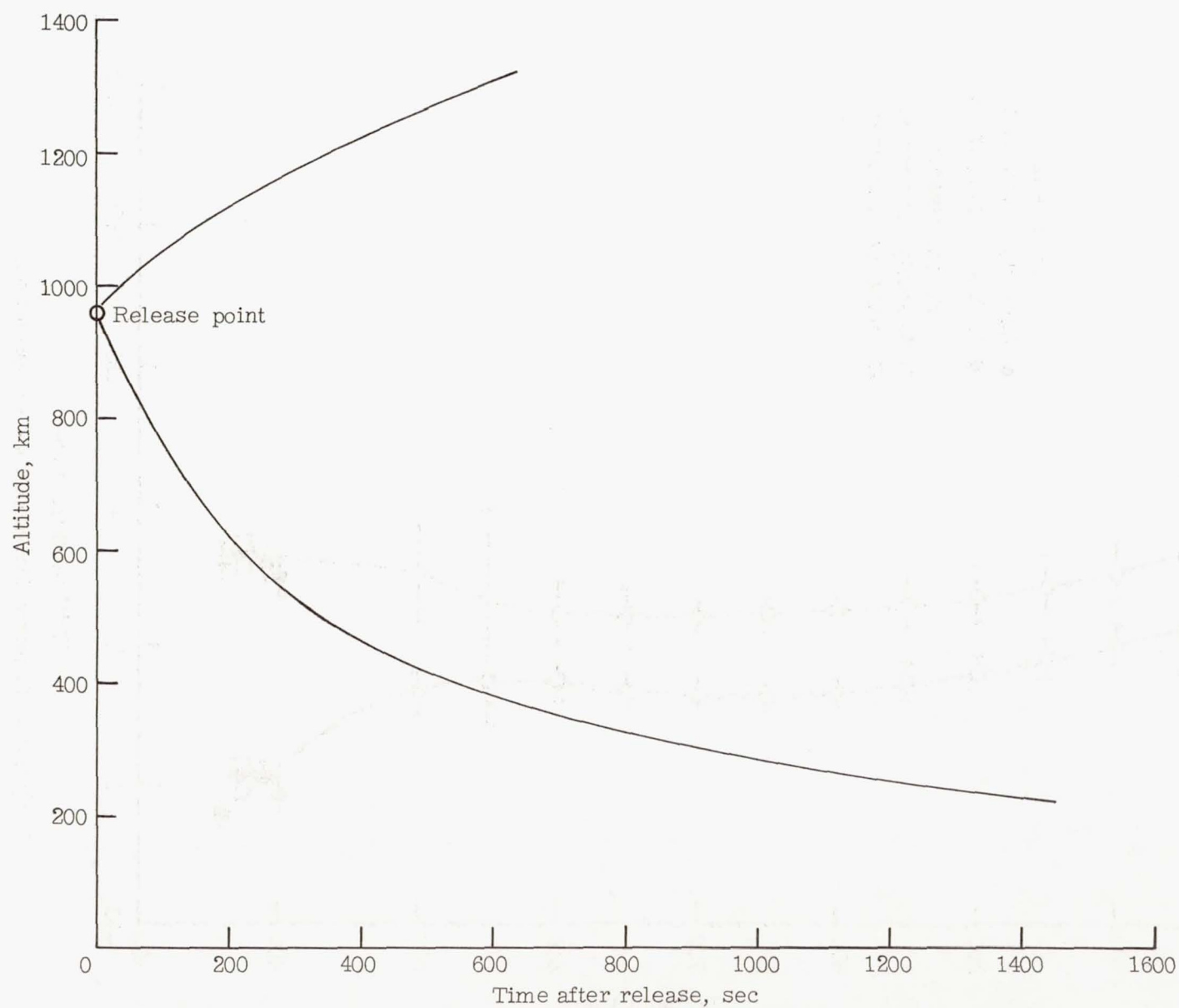
Figure IX-4.- Altitude of upper and lower extremities of ionized cloud as a function of time. Javelin second release.
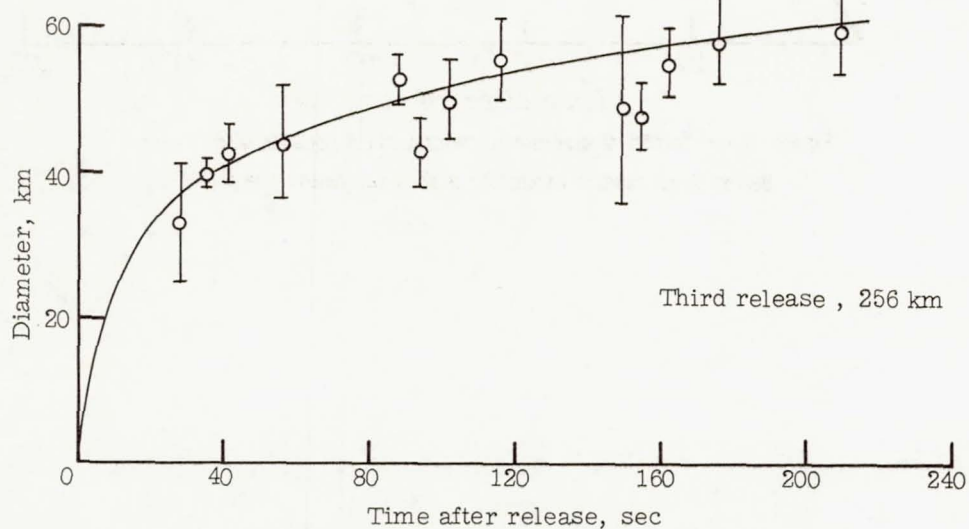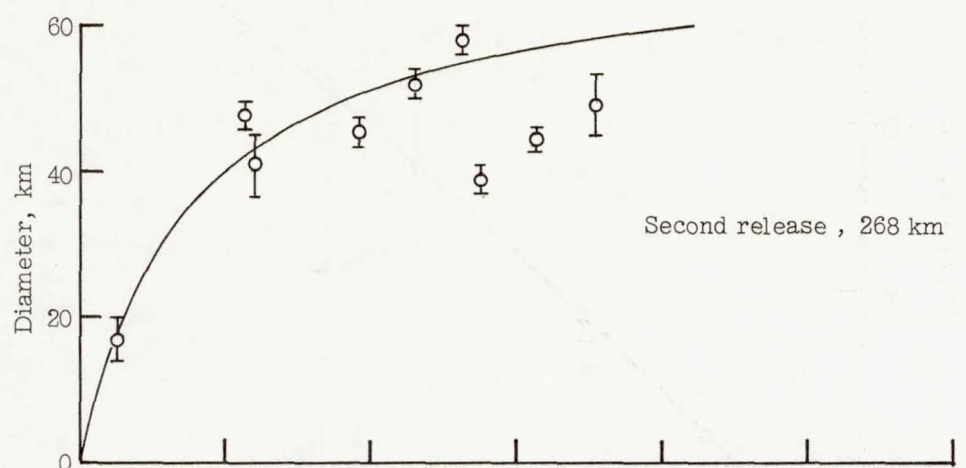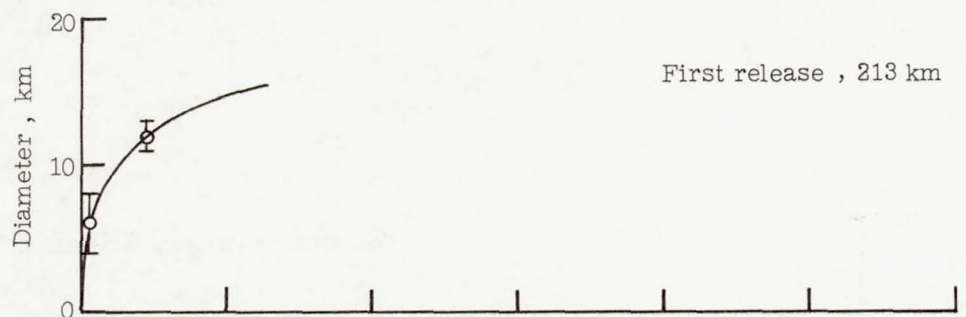
Figure IX-5.- Growth of diameter of neutral clouds released from Nike-Tomahawk.
Barred lines indicate variability of diameter measurements.

95
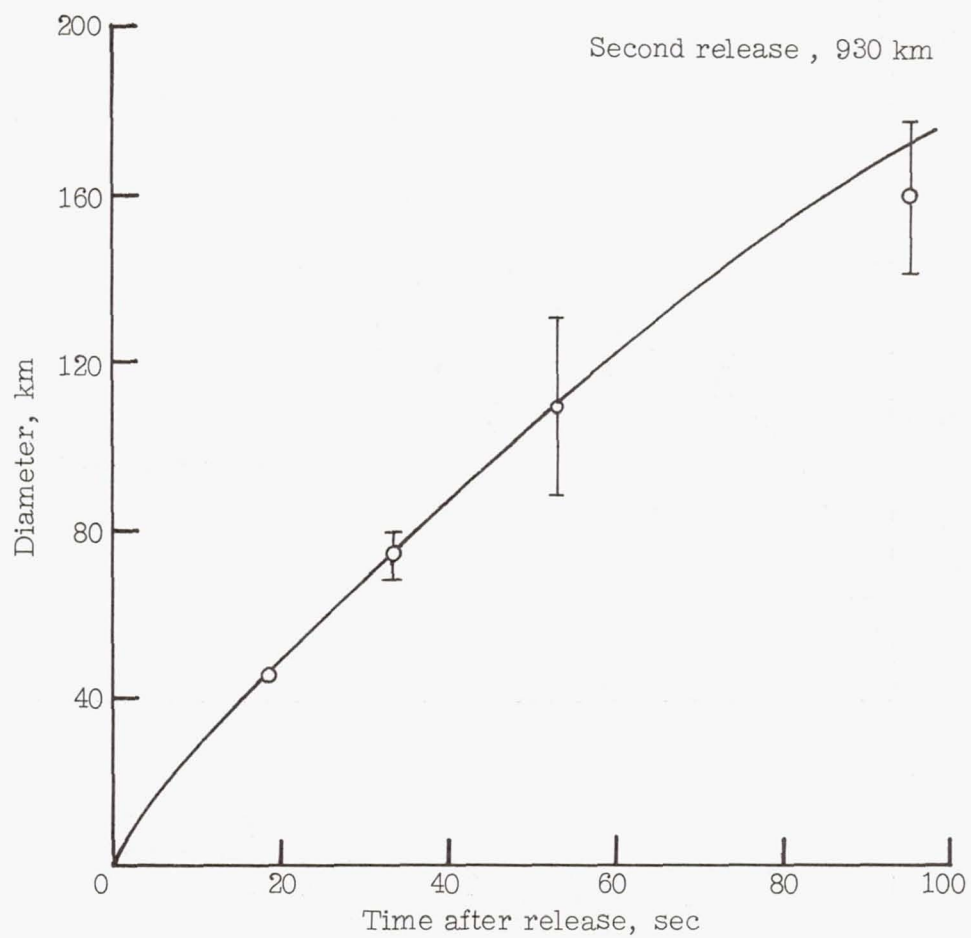
Figure IX-6.- Growth of diameter of neutral cloud released from Javelin.
Barred lines indicate variability of diameter measurements.

X. NASA ANALYSIS OF SECOND BARIUM RELEASE FROM JAVELIN

By David Adamson
NASA Langley Research Center

INTRODUCTION

Magnetometers carried onboard satellites and probes have added considerable knowledge of the topology of the earth's magnetic field and its distortion under the impact of the streaming solar wind.   There is, however, an almost complete lack of data on the nature of the electric fields permeating the magnetosphere. The technique of releasing ionized clouds in space and observing their drift motion does provide one way of making measurements of the electric fields and thus remedying this deficiency. In addition, observing the rate of growth of the lateral dimension of the cloud permits an estimate or a bound to be placed on the level of fluctuations in the magnetic field. In a very real sense the technique is simply an extension of that involving neutral cloud releases in the upper atmosphere as a means of obtaining data on atmospheric winds and turbulence.

In the present section data obtained from the release made from the Javelin at about 930 km is analyzed and discussed. Estimates are made of the electric-field distribution to about 1100 km and an upper bound established on the level of fluctuations in the field. In addition, a comparison has been made of cloud elongation and drift along the magnetic-field line with theoretical estimates.

SYMBOLS

B_o steady ambient magnetic-field strength

l_d distance from point of peak brightness to lower half-brightness point on longitudinal axis

l_u distance from point of peak brightness to upper half-brightness point on longitudinal axis

P parameter defining growth of cloud width with time

v particle velocity

v_A Alfvén wave speed

v_m mean radial velocity of particles

v_t mean thermal velocity of particles

w   cloud width

w_d, w_u lower and upper cloud width, respectively (see fig. X-10)

t   time

$\Phi_B(\omega)$ power spectral density of magnetic-field fluctuations as a function of angular frequency

EVOLUTION OF NEUTRAL AND IONIZED CLOUDS

In figures X-1(a) and X-1(b) selected frames taken with K-24 cameras (Wallops Island) and Super-Schmidt cameras (Wallops Island and Eastville) are mounted in time sequence. The photographs are so arranged that the center of each frame (indicated by marker on the base) corresponds to the effective time of the exposure (midpoint of exposure) as read off the horizontal time scale. In figure X-2 two photographs taken with a BC-4 camera from Wallops Island during the later phase of cloud development (23 min 25 sec and 26 min 55 sec) clearly exhibit cloud striations which appear at later times and to which allusion is made in the discussion which follows.

The second release was made from the Javelin at an altitude of 929 km. At such a high altitude collisions with particles of the ambient atmosphere are so infrequent it can safely be assumed that, so far as the motion and development of the neutral cloud is concerned, they will have no measurable effect. The center of mass of the neutral cloud formed at release moves, therefore, on a ballistic path. As it does so, it expands radially with a velocity of about 1.2 km/sec. Note the doughnutlike structure exhibited by the neutral cloud shown in frame 15 (K-24) and frame L14710 (Super-Schmidt) of figure X-1(a). This phenomenon has been observed previously when a neutral cloud has been released at altitudes sufficiently great that effects of particle collisions with surroundings can be ignored (ref. X-1). It is interesting to note that the neutral cloud is still discernible in a Super-Schmidt photograph (frame L14710) taken 3 min after release when the cloud has attained a diameter of about 425 km.

Within a short time after release the barium atoms become ionized. Thus, from photometric data presented in table VII-I over 60 percent of the total number of ions observed have already been formed in the first 30 sec. Indeed, in the subsection

"Analysis of Cloud Growth," in which cloud width is discussed, it seems possible to put an even lower bound on the rapidity of the initial phase of ionization. The individual ions, once formed, spiral along the magnetic-field lines and the ionized cloud becomes progressively more elongated with time.

At about 6 min after release there is a first indication of "flaring" at the lower extremity of the cloud at an altitude of about 350 km (frame L14711, fig. X-1(a)) and by 9 min this flaring has become quite pronounced (frame L14712, fig. X-1(a)). Such flaring is attributed to the partial arresting of the motion of the lower extremity of the elongated cloud by the atmosphere and the associated piling up of ions. As is to be expected, the flaring is predominantly on the underside of the cloud since it is in this direction that the neutral cloud, out of which the ions are formed, is moving following release; hence, more ions are deposited on the underside.

By 12 min after release there are noticeable structural changes in the lowermost part of the cloud (frames T7099 and T7100, fig. X-1(b)). Thus, the underside of the cloud has acquired a sharply defined boundary which appears to be a prolongation of the underside of the tail of the cloud which still extends a considerable distance along the field line. In the immediate proximity of this sharp edge there are a number of well-defined striations. (These striations are not clearly discernible in the photographs in fig. X-1 as a result of loss of detail due to photographic reduction.) Such structural features have been observed previously (refs. X-2 and X-3). There is also some degree of bulging on the upper side. The central stem of the cloud is still clearly discernible after 15 min (frame T7100, fig. X-1(b)) at which time it extends upward to an altitude exceeding 1000 km. After 20 min the number of striations has increased, thus as many as five can be counted on the photograph (frame 8, BC-4) in figure X-2 taken at 23 min 25 sec. Some minutes prior to loss of sight of the cloud against the brightening dawn background there is evidence of the combining of these several striations to form two longitudinal filaments of about equal diameter as shown in the photograph taken at 26 min 55 sec (frame 9, BC-4).

In figure X-3, the projections on the celestial sphere of the magnetic-field line through the release point (computed by using a 48-term spherical harmonic expansion of the earth's magnetic field[1]) as viewed from Wallops Island (SPANDAR site at which K-24 cameras were located) and Coquina Beach are drawn for September 24, 1966, $09^h 20^m$ and $09^h 50^m$ UT, the period during which most the optical data was obtained. On each trace, height markers have been placed at 100-km intervals up to 1200 km.

Using figure X-3 in conjunction with figure X-4, in which slant ranges from Wallops and from Coquina to points on the magnetic-field line are plotted as functions of altitude,

---

[1]The program, described in reference X-4, was provided by E. G. Stassinopoulos of the Laboratory of Theoretical Studies, NASA Goddard Space Flight Center.

enables one to make quick estimates of the position and size of structural features of interest appearing in any of the photographs in figures X-1(a), X-1(b), and X-2. It is to be emphasized, however, that such estimates must perforce be rough since no allowance has been made for cloud drift relative to earth.

TRIANGULATION DATA

Figures X-5 and X-6 are reproductions of figures IX-1 and IX-2 and define the shape of the ionized cloud center line in terms of altitude as a function of geographic latitude and longitude, respectively, at various times following release. The lines (not in figs. IX-1 and IX-2) show the form of the magnetic-field line through the point of release computed by using the Goddard program. Note that at early times the cloud center line closely parallels the calculated form of the field line although there is a slight displacement of the cloud center line to the east. This is believed to be due in part to the lapse in time between release and the completion of the initial phase of ionization and in part to the initial ionized cloud drift across the magnetic field prior to the shorting of the polarization charge through the ionosphere, as described subsequently.

Figure X-7 is a reproduction of figure IX-3 and shows the westerly and southerly velocity components of the points of intersection of the cloud center line with horizontal planes at various altitudes.[2] So far as the westerly component of drift is concerned, this is believed to be entirely attributable to the existence of a northerly component of the electric field which is plotted as a function of altitude in figure X-8. A corresponding curve pertaining to the southerly drift of the cloud has not been included since it is believed that this southerly drift may well be a manifestation of a vertical falling of the cloud arising through gravity-induced polarization fields within the cloud interior. Thus, in figure X-9 the cloud, for simplicity, is portrayed as having a rectangular cross section. The gravity component normal to the field line causes the ions to drift towards the one lateral face and the electrons towards the other. This polarization of charge results in the buildup of a westerly directed electric field within the cloud interior which, coupled with the earth's magnetic field, would impart a downward motion to the cloud. If the cloud were in a perfect vacuum it would indeed be expected to fall with the acceleration of gravity as discussed in reference X-5. Actually, the barium cloud is immersed in an ambient plasma, the electrons of which can move freely up and down magnetic-field lines. The accumulation of polarization charges on the lateral faces of the cloud will tend to be inhibited by the short circuiting provided by electrons drifting down the field lines on the west, across the top of the ionosphere, and up the field lines on the east (as indicated by the heavy arrows of fig. X-9).

---

[2]The lowermost points in this plot (i.e., 400 km and less) were obtained from the first release.

The conjecture that the apparent southerly drift is actually a fall under gravity receives some support from the fact that the drift in question vanishes at an altitude of slightly under 400 km where particle collisions begin to play a role. Such might be expected on the basis of this conjecture, since at these altitudes gravity begins to be opposed by equal and opposite buoyancy forces; on the other hand, if the southerly drift had indeed been the result of electric fields, there is no apparent reason why the drift velocity should fall to zero at this altitude.

ANALYSIS OF MOTION OF CLOUD ALONG MAGNETIC-FIELD LINE

Experimental

Six K-24 photographs covering the time interval from 148 to 597 sec after release were selected for use in analyzing the motion of the cloud along the magnetic-field line. Isodensitometer traces were made of each negative on a Joyce-Loebl microdensitometer with an isodensitometer attachment. A reproduction of one of the prints and the associated isodensitometer trace are shown as figure X-10. A description of the isodensitometer and its mode of operation is given in reference X-6. Suffice it to say that as the negative is scanned line by line, intervals between successive mode changes correspond to equal increments in film density; therefore, assuming a linear H-D curve, changes in scanning mode take place at equal increments in cloud brightness. If, then, contours are drawn through boundaries between successive mode changes, the contour lines will be isophotes with equal steps in brightness between them. The point marked P on the isodensitometer trace in figure X-10 clearly defines the point of maximum brightness. The location of the point of maximum brightness relative to the release point is plotted against time in figure X-11.

Theoretical

Theoretical calculations have been made of the motion of the individual particles along the magnetic-field line and their redistribution with time. It has been assumed that the barium ions will pursue their individual spiral paths, uninfluenced by neighboring particles (hence subject only to magnetic, gravitational, and centrifugal forces) on the ground that by the time the ionized cloud had formed, collisions would have ceased to play a role and charge neutrality would have been established. The details are presented in parts 1 and 2 of appendix A.

Two separate velocity distributions have been considered:

Model A — A Maxwellian velocity distribution is presupposed which corresponds to a mean thermal speed of 0.54 km/sec which, in turn, corresponds to a temperature of the chemical reaction of about 2400° K.

Model B — A Maxwellian velocity distribution is presupposed which corresponds to a mean thermal speed equal to about 1.25 km/sec — the mean speed of particles comprising the neutral cloud.

In both models the initial velocity of the mass center of the cloud along the field line has been taken as equal to that of the fourth stage of the Javelin rocket at the instant the release was initiated, that is, 0.34 km/sec.[3] No allowance has been made for field-line slippage, and the magnetic lines to which the cloud attaches are assumed to corotate with the earth.

Cloud brightness is proportional to the number of particles per unit area along the line of sight; thus, to compare the theoretical results with the brightness distribution along the center line of the cloud image on a photograph taken from a particular observation site, allowance for the obliquity of the line of sight relative to the cloud center line must be made. Such corrections have been made as described in part 3 of appendix A, and the results are presented in figures X-12(a) and X-12(b) for models A and B, respectively. In both figures the observation site is Wallops Island and brightness (in arbitrary units) has been plotted against position on cloud center line for times of 100, 200, 300, 400, and 500 sec. The drifts of the points of peak brightness as obtained from figures X-12(a) and X-12(b) are transferred to figure X-11.

Comparison Between Observation and Theory

From a comparison of the downward drift corresponding to model A (mean thermal speed of 0.54 km/sec) with that of model B (mean thermal speed of 1.25 km/sec) it is noted that the drift is significantly higher in model A. This is to be expected since the upward-directed magnetic force resulting from line convergence is energy dependent.

A comparison between observation and theory shows a disparity of surprising magnitude, theory predicting a much more rapid fall than was actually observed to take place. This is not to be attributed to neglect of westward slippage of field lines since allowance for this would have entailed a reduction in centrifugal force opposing gravity, hence a more rapid fall and an even greater discrepancy. Nor can it be attributed to the assumption of a Maxwellian velocity distribution since if the velocity distribution used had been of

the form $K \exp\left[-\left(\dfrac{v - v_m}{v_t}\right)^2\right]$ where v_m is the mean radial velocity of particles and

v_t is the mean thermal velocity of particles (which emerges from a study of velocity distribution within the neutral cloud), the net result would be a flatter longitudinal distribution of particles along the field line but with little effect on net drift. It is hard to escape the

---

[3] This value is probably somewhat high by virtue of the deceleration in the interval between release and attachment to the magnetic-field lines.

conclusion, therefore, that the difference arises either as a result of an electric-field component along the field lines or as the result of an interaction of the cloud with the ambient plasma. This conclusion is being subjected to further study.

ANALYSIS OF CLOUD GROWTH

The isodensitometer trace (fig. X-10) used in the analysis of cloud motion is also of use in the analysis of cloud growth. In figure X-10 the greater bulging of the elongated cloud on its underside, which is especially noticeable on the isodensitometer traces, is to be expected since the neutral cloud moves downward after release and the bulk of the ions is deposited on this side.

In the isodensitometer tracing of figure X-10 the contours defined by mode changes are, as mentioned previously, lines of constant local brightness or isophotes. The heavy line defines the median contour on which the brightness is half the maximum. It is convenient to discuss cloud growth in terms of the growth of this median contour. The cloud elongations downward and upward, l_d and l_u in figure X-10, correspond to the distances from the point of peak brightness to the lowermost and uppermost extremity of the longitudinal axis of the median contour, respectively. Upper and lower cloud widths are similarly defined in figure X-10.

The downward and upward elongations and the total cloud length are plotted in figure X-13 as functions of time. The initial overall rate of elongation is about 2.2 km/sec.

In figure X-14 similar plots are presented of cloud widths (upper, lower, and total) as functions of time. The point corresponding to lower cloud width is omitted for 148 sec since the photograph in question was taken without filters and the presence of the neutral cloud has produced considerable distortion of the isodensitometer contours on the lower side. The effective total cloud width remains roughly constant and equal to about 28 km over the time interval covered. If the mean transverse growth rate is assumed to be equal to that given by the initial rate of cloud elongation (i.e., 2.2 km/sec) the time characterizing the initial phase of ionization is 12.5 sec.

It is shown in appendix B that random fluctuations in the magnetic field would be expected to result in an increase of (Cloud width)^2 proportional to time, that is,

$$w^2(t) = w^2(0) + Pt \tag{1}$$

where the growth parameter P is

$$P = \frac{\pi v_A^2 \Phi_B(0)}{B_o^2}$$

and

w(t)   cloud width as function of time

v_A Alfvén wave speed, km/sec

B_o ambient magnetic-field strength, γ

$\Phi_B(0)$ power spectral density at zero frequency, γ^2 sec

In view of the large intrinsic scatter of the data it is hard to discern any increase in cloud width with time up to 500 sec. The two dash curves in figure X-14 correspond to values of the growth parameter P of 7×10^{-2} and 35×10^{-2} km^2/sec. Although one might be hesitant in concluding the growth parameter to be less than 7×10^{-2} km^2/sec, it is fairly evident that it is less than 35×10^{-2} km^2/sec. Accepting the latter value as an upper bound of the growth parameter and by using equation (1), one can arrive at an upper limit of 500 γ^2 sec on the value of the power spectrum of the magnetic-field fluctuations at zero frequency $\Phi_B(0)$, subject of course to the assumptions implicit in the analysis presented in appendix B.

At the time the releases were made from the Javelin there was only low to moderate geomagnetic activity. Thus, the 3-hour magnetic K-indices at Fort Belvoir, Virginia, for the periods 0600 to 0900 and 0900 to 1200 UT were 2 and 3, respectively.

SUMMARY OF RESULTS

Within the scatter of the data the westward drift of the ionized cloud appears to be fairly uniform between altitudes of 375 and 1100 km and equal to 60 km/sec. This would correspond to the existence of a northerly directed electric field of between 2 and 3 mV/m. In addition, the cloud was observed to drift in a southerly direction with a speed which varied with altitude. One is hesitant in ascribing this to a westerly directed electric field by virtue of its apparent variation with altitude. It is believed that this apparent southerly drift was actually associated with the fall of the cloud (in a direction perpendicular to the field lines) under gravity. Such an explanation would be consistent with the fact that this component of drift became zero at an altitude of about 390 km where buoyancy forces might be expected to become large enough to oppose the force of gravity.

Magnetic-field fluctuations promote the diffusion of particles transverse to the field lines and a resulting growth in cloud width. The large scatter of data on the variation of cloud width with time permits only a very loose upper bound of 500 γ^2 sec to be placed on the magnetic-field fluctuations.

The slow rate of fall of the cloud mass center is surprising in view of the steepness of the magnetic-field lines through the point of release. It could possibly have been due to interaction between the ionized cloud and the ambient plasma. At any rate, until this possibility has been eliminated, one is hesitant about interpreting this slow rate of fall as being due to an upward-directed electric-field component along the field line. This facet of cloud behavior is the subject of continued study.

APPENDIX A

VARIATION OF THE LONGITUDINAL BRIGHTNESS DISTRIBUTION WITH
TIME WHEN VIEWED FROM A SPECIFIED OBSERVATION POINT

The calculation of the variation of the longitudinal brightness distribution with time is considered in three parts. In part 1 the motion along the magnetic-field line of the center of gyration of a single spiraling particle is investigated. So far as its motion along the field line is concerned, the particle is assumed to be subject only to the force of gravity and a magnetic force resulting from convergence of magnetic-field lines. In part 2 an expression is derived for the density distribution of particles along the field line as a function of time. Finally, in part 3, allowance is made for the obliquity of the line of sight with respect to the cloud center line in computing the number of particles per unit area along the line of sight which, in turn, is proportional to the cloud brightness.

Part 1. Motion of a Single Particle

As mentioned in the introductory paragraph, it is assumed that a particle spiraling along a magnetic-field line in a time-independent field is subject only to gravitational and magnetic forces. Since the magnetic force at every instant acts in a direction perpendicular to the particle path, it does not contribute to any change in the energy content of the particle. Thus, the sum of the kinetic and potential energies of the particle remain constant, that is,

$$\frac{1}{2} m v^2 - \frac{G m M_{\oplus}}{R} = \frac{1}{2} m v_o^2 - \frac{G m M_{\oplus}}{R_o} \tag{A1}$$

where

G   universal gravitational constant

m   mass of particle

$M_{\oplus}$ mass of earth

R   distance from earth's center

v   velocity of particle

The subscript o identifies the values at the instant of release. Hence

$$v^2 = v_O^2 + \frac{2GM_\oplus}{R_O}\left(\frac{R_O}{R} - 1\right)$$

Introducing $g_O = \dfrac{GM_\oplus}{R_O^2}$ and resolving v into its velocity components perpendicular to and along the magnetic-field line v_r and v_s, respectively, yield

$$v_s^2 + v_r^2 = v_{s,O}^2 + v_{r,O}^2 + 2g_O R_O\left(\frac{R_O}{R} - 1\right) \tag{A2}$$

By virtue of the adiabatic invariance of the magnetic moment of the gyrating particle

$$\frac{v_r^2}{B} = \frac{v_{r,O}^2}{B_O}$$

Substituting this expression in equation (A2) gives

$$v_s^2 = v_{s,O}^2 + v_{r,O}^2\left(1 - \frac{B}{B_O}\right) + 2g_O R_O\left(\frac{R_O}{R} - 1\right) \tag{A3}$$

In the case of the Javelin release the motion of particles is over a relatively short segment of the magnetic-field line, and it therefore suffices to consider only first-order deviations from uniformity of the magnetic field.

Denoting the distance from the release point measured along the magnetic-field line by s (positive downward) gives

$$B = B_O + \left(\frac{dB}{ds}\right)_O s$$

$$R = R_O + \left(\frac{dR}{ds}\right)_O s$$

Substituting these expressions into equation (A3) and retaining terms up to first order in s result in

$$v_s^2 = v_{s,O}^2 - \left[\frac{v_{r,O}^2}{B_O}\left(\frac{dB}{ds}\right)_O + 2g_O\left(\frac{dR}{ds}\right)_O\right]s$$

Differentiating with respect to time yields

$$\frac{dv_s}{dt} = -\frac{1}{2}\left[\frac{v_{r,O}^2}{B_O}\left(\frac{dB}{ds}\right)_O + 2g_O\left(\frac{dR}{ds}\right)_O\right]$$

Integrating twice with respect to time

$$s = v_{s,o}t + \frac{1}{2}\left[g_o \sin \theta_o - \frac{v_{r,o}^2}{2B_o}\left(\frac{dB}{ds}\right)_o\right]t^2 \tag{A4}$$

where θ_o is the inclination of the magnetic-field line with respect to the local horizontal at the release point as illustrated in sketch A1.
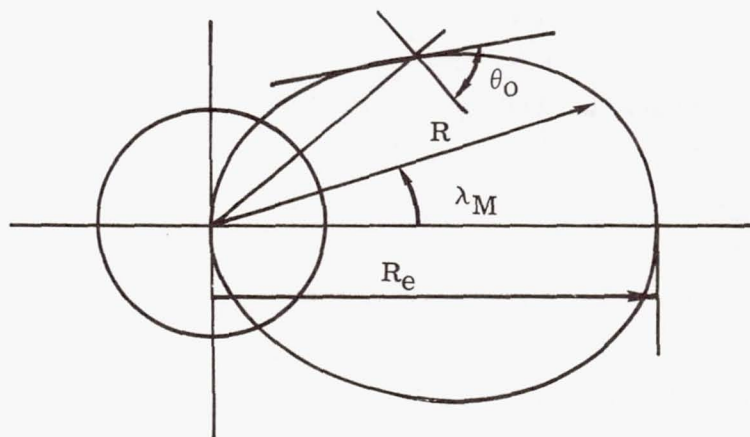
Sketch A1

The interpretation of equation (A4) is obvious; thus $g_o \sin \theta_o$ is the gravity force per unit mass along the magnetic-field line in the downward direction and

$$\frac{v_{r,o}^2}{2B_o}\left(\frac{dB}{ds}\right)_o$$

is the longitudinal magnetic force per unit mass resulting from magnetic-line convergence. (A minus sign indicates that the force is directed upward.)

By assuming the earth's field to be a dipole field, it can be shown that the polar equation of the magnetic-field line is given by

$$R = R_e \cos^2\lambda_M \tag{A5}$$

where R_e is the distance from the earth's center to the point at which the field line pierces the magnetic equatorial plane, and

$$B = B_e \frac{\left(1 + 3 \sin^2\lambda_M\right)^{1/2}}{\cos^6\lambda_M} \tag{A6}$$

From equations (A5) and (A6) it follows that

$$\sin \theta_O = \frac{2 \sin \lambda_{M,o}}{\left(1 + 3 \sin^2\lambda_{M,o}\right)^{1/2}}$$

and

$$\frac{1}{B_O}\left(\frac{dB}{ds}\right)_O = \frac{3 \sin \lambda_{M,o}\left(3 + 5 \sin^2\lambda_{M,o}\right)}{R_e \cos^2\lambda_{M,o}\left(1 + 3 \sin^2\lambda_{M,o}\right)^{3/2}}$$

Those particles which arrive at a point distance s from the release point at time t are the ones whose initial velocity components $v_{r,o}$ and $v_{s,o}$ fall on the parabola (labeled s in sketch A2) defined by equation (A4).
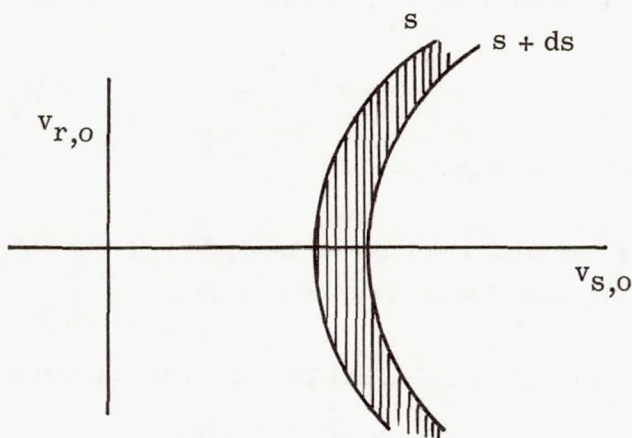
Sketch A2 (Hodograph plot corresponding to time t)

The following symbols are used in part 1 of this appendix:

B   ambient magnetic-field strength

G   universal gravitational constant

g   acceleration due to gravity

$M_\oplus$ mass of earth

m   mass of particle

R   distance from earth's center

s   distance from release point, measured along field line, positive downward

t   time

v   particle velocity

v_r particle velocity component perpendicular to field lines

v_s particle velocity component along field lines

λ_M magnetic latitude

θ inclination of magnetic-field line with respect to local horizontal

Subscripts:

o   conditions at point of release

e   conditions at point at which magnetic-field line through point of release
           pierces magnetic equatorial plane

Part 2. Calculation of Longitudinal Density Distribution of Barium Ions
as a Function of Time

The barium ions form out of the neutral cloud which, immediately after release, is moving with essentially the same velocity as the rocket. Denote the velocity components of the drift motion along and perpendicular to the magnetic-field lines by U_s and U_r, respectively. Superimposed on this drift motion the thermal velocities of the ions are assumed to conform to a Maxwellian distribution. In the velocity space depicted in sketch A3 the velocity distribution is a spherically symmetric Maxwellian cloud centered on point O', the extremity of the drift vector.
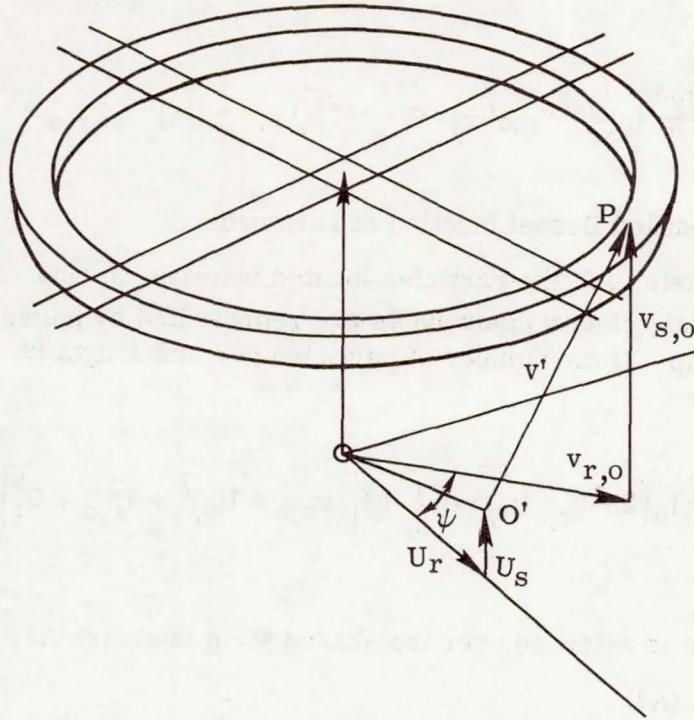
Sketch A3

If the total number of ions is denoted by N, then the density of ions at point P is given by

$$\frac{N\beta^3}{\pi^{3/2}} \exp\left(-\beta^2 v'^2\right)$$

where

$$v'^2 = \left(v_{s,o} - U_s\right)^2 + \left(v_{r,o}^2 + U_r^2 - 2v_{r,o}U_r \cos \psi\right)$$

and

$$\beta = \sqrt{\frac{m}{2kT}}$$

By integrating over ψ the following expression is obtained for the number of particles in the velocity range from $\left(v_{r,o}, v_{s,o}\right)$ to $\left(v_{r,o} + dv_{r,o}, v_{s,o} + dv_{s,o}\right)$, that is, those particles whose representative points fall within the annular ring shown in sketch A3:

$$\frac{N\beta^3}{\pi^{3/2}} \exp\left\{-\beta^2\left[(v_{s,o} - U_s)^2 + v_{r,o}^2 + U_r^2\right]\right\}v_{r,o}\, dv_{r,o}\, dv_{s,o} \int_0^{2\pi} \exp\left(2\beta^2 v_{r,o}U_r \cos\psi\right)d\psi$$

$$= \frac{2N\beta^3}{\pi^{1/2}} I_0\left(2\beta^2 v_{r,o}U_r\right)\exp\left\{-\beta^2\left[(v_{s,o} - U_s)^2 + v_{r,o}^2 + U_r^2\right]\right\}v_{r,o}\, dv_{r,o}\, dv_{s,o}$$

where I_0 is the modified Bessel function of zero order.

Reverting to sketch A2, the particles located between s and $s + ds$ at instant t are those whose initial velocity components are represented by points lying within the shaded parabolic strip. If the number of particles per unit length is $n(s,t)$, then

$$n(s,t)ds = \frac{2N\beta^3}{\pi^{1/2}} \int\int I_0\left(2\beta^2 v_{r,o}U_r\right)\exp\left\{-\beta^2\left[(v_{s,o} - U_s)^2 + v_{r,o}^2 + U_r^2\right]\right\}v_{r,o}\, dv_{r,o}\, dv_{s,o}$$

$$\text{(A7)}$$

where the integration is extended over the shaded strip in sketch A2.

From equation (A4)

$$\left(\frac{\partial v_{s,o}}{\partial s}\right)_{v_{r,o}} = \frac{1}{t}$$

Hence, equation (A7) can be written in the form

$$n(s,t) = \frac{2N\beta^3}{\pi^{1/2}t} \int I_0\left(2\beta^2 v_{r,o}U_r\right)\exp\left\{-\beta^2\left[(v_{s,o} - U_s)^2 + v_{r,o}^2 + U_r^2\right]\right\}v_{r,o}\, dv_{r,o} \qquad \text{(A8)}$$

where

$$v_{s,o} - U_s = \frac{s}{t} - U_s - \frac{1}{2}\left[g_0 \sin\theta_0 - \frac{v_{r,o}^2}{2B_0}\left(\frac{dB}{ds}\right)_0\right]t$$

The following symbols are used in part 2 of this appendix:

g   acceleration due to gravity

I_0 modified Bessel function of zero order

k   Boltzmann constant

APPENDIX A

m   mass of particle

N   total number of ions

n   number of particles per unit length of field line

s   distance from release point, measured along field line

T   temperature of ions

t   time

U_r initial component of drift motion perpendicular to field lines

U_s initial component of drift motion along field lines

v' velocity of particle relative to drifting neutral cloud, represented by $O'P$ in sketch A3

v_r particle velocity component perpendicular to field lines

v_s particle velocity component along field lines

$\beta = \sqrt{\dfrac{m}{2kT}}$

ψ angle defined in sketch A3

Subscript:

o   conditions at point of release

Part 3. Longitudinal Distribution of Brightness as Viewed From a Specified Observation Point

The brightness of an optically thin cloud is proportional to the number of particles per unit area along the line of sight. If then the cloud is viewed obliquely, it appears brighter than if it were viewed transversely. In computing the variation of cloud brightness along its length due allowance must be made for this.

APPENDIX A

The earth-centered dipole which best approximates the earth's magnetic field is one having its axis slanted 12° from the earth's axis of rotation, with the north magnetic pole lying on the meridian 69° west of Greenwich. This dipole model has been adopted for the present calculations and is illustrated in sketch A4 for which
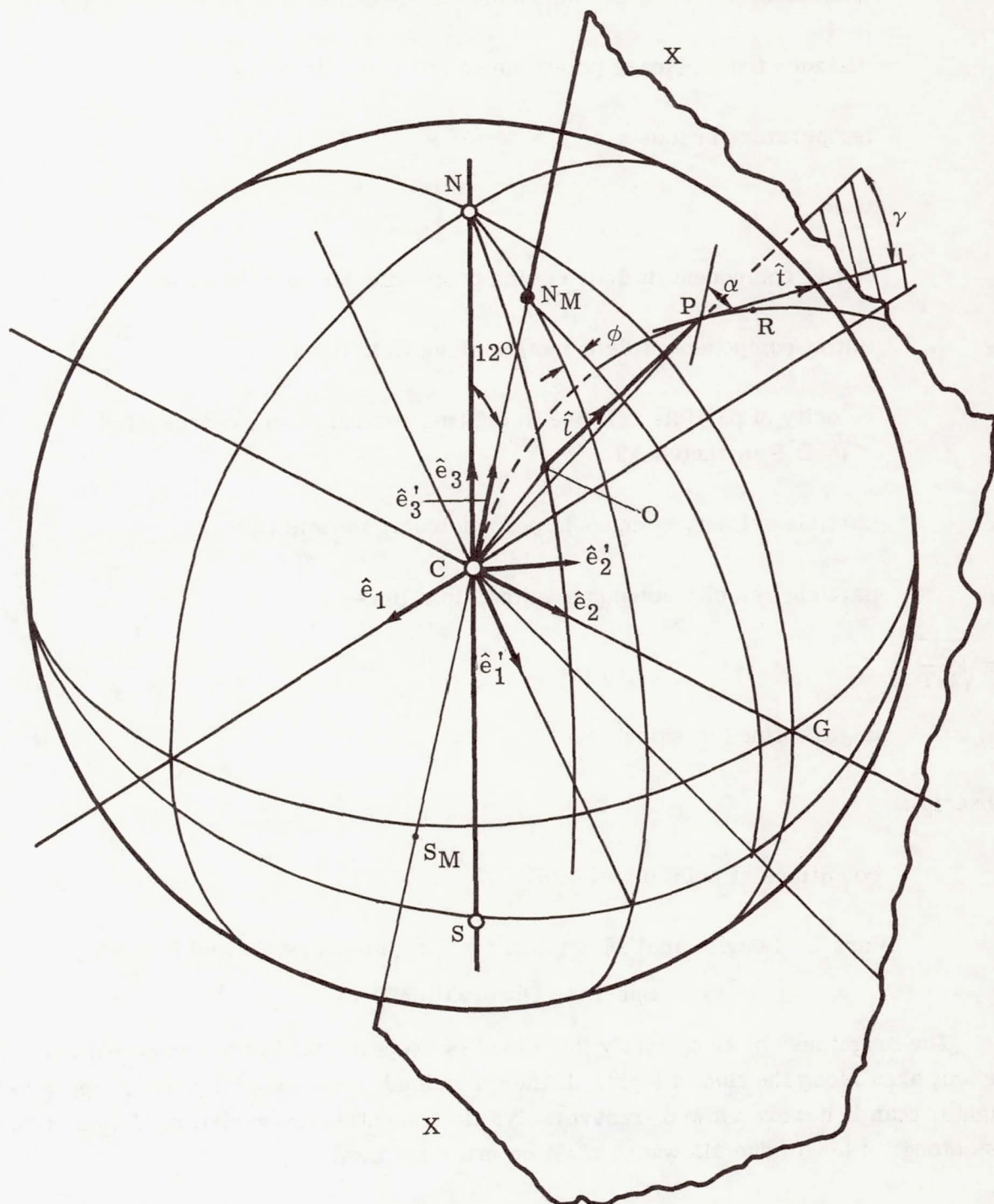
Sketch A4

APPENDIX A

C   earth's center

$\hat{e}_1, \hat{e}_2, \hat{e}_3,$
$\hat{e}_1', \hat{e}_2', \hat{e}_3'$ unit vectors (defined subsequently)

G   intersection of equatorial plane with Greenwich meridian

N   North Pole

N_M north magnetic pole, on meridian 69° west of Greenwich

$\hat{l}$ unit vector directed along line of sight

O   observation station

P   point on field line passing through release point R

R   release point

R_P distance from P to earth's center

R_O geocentric distance from O to earth's center

S   South Pole

S_M south magnetic pole

$S_M N_M$ dipole axis, slanted 12° from earth's axis of rotation

$\hat{t}$ unit vector along tangent to magnetic-field line at point P

α angle subtended between unit vector $\hat{t}$ and line drawn through P parallel to dipole axis

γ angle between $\hat{l}$ and $\hat{t}$

Λ_P geocentric latitude of point P

Λ_O geocentric latitude of point O

ϕ angle between plane $\mathbf{XX}$ containing magnetic-field line and meridional plane CNN_M

Ω_P geocentric longitude of point P

Ω_O geocentric longitude of point O

By introducing the right-handed triad of unit vectors $\hat{e}_1$, $\hat{e}_2$, $\hat{e}_3$ where

$\hat{e}_3$ is directed toward the geographic North Pole

$\hat{e}_2$ lies in the meridional plane through Greenwich

$\hat{e}_1$ is perpendicular to both

the relation between vectors can be expressed

$$\overrightarrow{OP} = \overrightarrow{CP} - \overrightarrow{CO} = \hat{e}_1 L_1 + \hat{e}_2 L_2 + \hat{e}_3 L_3$$

where

$$L_1 = R_P \cos \Lambda_P \sin \Omega_P - R_O \cos \Lambda_O \sin \Omega_O$$

$$L_2 = R_P \cos \Lambda_P \cos \Omega_P - R_O \cos \Lambda_O \cos \Omega_O$$

$$L_3 = R_P \sin \Lambda_P - R_O \sin \Lambda_O$$

Hence, direction cosines of unit vector $\hat{l}$ directed along line of sight

$$l_i = \frac{L_i}{\sqrt{L_1^2 + L_2^2 + L_3^2}} \qquad (i = 1, 2, 3) \qquad (A9)$$

Denote the angle subtended between the tangent to the magnetic-field line at point P and a line drawn through P parallel to the dipole axis by α. Then

$$\alpha = \frac{\pi}{2} - \lambda_M + \tan^{-1}\left(\frac{1}{2 \tan \lambda_M}\right) \qquad (A10)$$

where λ_M is the geomagnetic latitude of point P.

A second right-handed triad of unit vectors $\hat{e}_1'$, $\hat{e}_2'$, $\hat{e}_3'$ is introduced where

$\hat{e}_3'$ is directed along the dipole axis CN_M

$\hat{e}_1'$ lies along the intersection of the meridional plane through the north magnetic pole and the magnetic equatorial plane

$\hat{e}_2'$ is perpendicular to both

These unit vectors are related to the unit vectors $\hat{e}_1$, $\hat{e}_2$, $\hat{e}_3$ by the matrix equation

$$\begin{bmatrix} \hat{e}_1' \\ \hat{e}_2' \\ \hat{e}_3' \end{bmatrix} = \begin{bmatrix} \cos 12^O \sin 69^O & \cos 12^O \cos 69^O & -\sin 12^O \\ -\cos 69^O & \sin 69^O & 0 \\ \sin 12^O \sin 69^O & \sin 12^O \cos 69^O & \cos 12^O \end{bmatrix} \begin{bmatrix} \hat{e}_1 \\ \hat{e}_2 \\ \hat{e}_3 \end{bmatrix} \tag{A11}$$

The unit vector $\hat{t}$ lying along the tangent to the magnetic-field line at point P is given by

$$\hat{t} = \hat{e}_1'(\sin \alpha \cos \phi) + \hat{e}_2'(\sin \alpha \sin \phi) + \hat{e}_3'(\cos \alpha)$$

Hence by using equation (A11)

$$\hat{t} = \hat{e}_1 t_1 + \hat{e}_2 t_2 + \hat{e}_3 t_3$$

where

$$t_1 = \cos 12^O \sin 69^O \sin \alpha \cos \phi - \cos 69^O \sin \alpha \sin \phi + \sin 12^O \sin 69^O \cos \alpha$$

$$t_2 = \cos 12^O \cos 69^O \sin \alpha \cos \phi + \sin 69^O \sin \alpha \sin \phi + \sin 12^O \cos 69^O \cos \alpha$$

$$t_3 = -\sin 12^O \sin \alpha \cos \phi + \cos 12^O \cos \alpha$$

The angle between the line of sight and the tangent to the magnetic-field line, denoted γ, is given by

$$\gamma = \cos^{-1}\left(l_1 t_1 + l_2 t_2 + l_3 t_3\right)$$

Cloud brightness is proportional to the number of particles per unit area along the line of sight, that is

$$\text{Cloud brightness} \propto \frac{n(s,t)}{\sin \gamma(s)} \tag{A12}$$

APPENDIX A

where $n(s,t)$ is the longitudinal density derived in part 2 of this appendix. By using equation (A12) the brightness variation along the cloud length, as viewed from Wallops Island, has been computed at various times, and these results are presented in figures X-12(a) and X-12(b).

APPENDIX B

TRANSVERSE DIFFUSION ARISING FROM FLUCTUATIONS
IN THE MAGNETIC FIELD

In this appendix the equations for determining the transverse diffusion arising from fluctuations in the magnetic field are derived.

If the time-independent magnetic field is denoted by $\vec{B}_0$ and the fluctuations in the electric and magnetic fields by $\vec{E}_1(t)$ and $\vec{B}_1(t)$, respectively, then the force acting on a charged particle in newtons is expressed

$$\text{Force} = e\left[\vec{E}_1 + \vec{v} \times \left(\vec{B}_0 + \vec{B}_1\right)\right]$$

where e is the electronic charge in coulombs, $\vec{E}_1$ is in volts/meter, $\vec{v}$ is in meters/sec, and $\vec{B}_0$ and $\vec{B}_1$ are in webers/meter^2.

It is assumed that the fluctuations in the electromagnetic field are associated with propagating Alfvén waves, thus

$$\left|\vec{E}_1\right| \approx O(v_A B_1)$$

where v_A is the Alfvén wave speed.

In the present instance $v \ll v_A$; hence, to a good approximation the force on a charged particle is given by
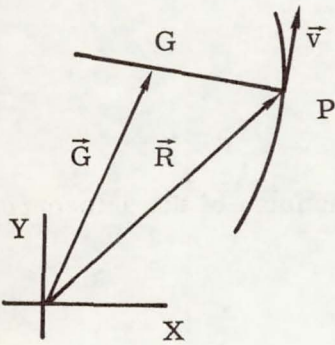
$$\text{Force} = e\left(\vec{E}_1 + \vec{v} \times \vec{B}_0\right) \tag{B1}$$

For the purposes of the analysis which follows sketch B1 is included, in which a steady and uniform magnetic field $\vec{B}_0$ is assumed to be directed into the plane of the paper, and the electric-field fluctuations are assumed to be confined to the plane of the paper. In this sketch the position of the particle is represented by point $P(\vec{R})$ and its guiding center by $G(\vec{G})$. Clearly,

$$\vec{G} = \vec{R} + \frac{m}{eB_0^2} \vec{v} \times \vec{B}_0$$

Sketch B1   and taking the time derivative gives

$$\dot{\vec{G}} = \vec{v} + \frac{m}{eB_o^2}\dot{\vec{v}} \times \vec{B}_o = \vec{v} + \frac{1}{B_o^2}\left(\vec{E}_1 + \vec{v} \times \vec{B}_o\right) \times \vec{B}_o = \vec{E}_1 \times \frac{\vec{B}_o}{B_o^2}$$

Then, with the particle assumed to start at the origin at $t = 0$,

$$\vec{G}(t) = \int_0^t \vec{E}_1(\xi)d\xi \times \frac{\vec{B}_o}{B_o^2}$$

$$G^2(t) = \frac{1}{B_o^2}\int_0^t \int_0^t \left(E_{1,x}(\xi)E_{1,x}(\eta) + E_{1,y}(\xi)E_{1,y}(\eta)\right)d\xi\,d\eta$$

Since the fluctuations are assumed to be isotropic, taking the ensemble average (indicated by $< >$) gives

$$\langle G^2\rangle = \frac{2}{B_o^2}\int_0^t \int_0^t R(\xi-\eta)d\xi\,d\eta \tag{B2}$$

where $R(\tau)$ is the autocorrelation function associated with fluctuations in each of the two components

$$R(\tau) = \left\langle E_{1,x}(t+\tau)E_{1,x}(t)\right\rangle = \left\langle E_{1,y}(t+\tau)E_{1,y}(t)\right\rangle$$

If the correlation time is assumed to be small, then to a good approximation

$$\langle G^2\rangle = \frac{2t}{B_o^2}\int_{-\infty}^{+\infty} R(\zeta)d\zeta \tag{B3}$$

Introducing spectral density gives

$$\langle E^2\rangle = \langle E_x^2\rangle + \langle E_y^2\rangle = \int_0^\infty \Phi_E(\omega)d\omega$$

Spectral density of E_x^2 and E_y^2 is clearly $\frac{1}{2}\Phi_E(\omega)$.

It can be shown that the spectral density is the Fourier transform of the autocorrelation function, that is

$$\Phi_E(\omega) = \frac{4}{\pi}\int_0^\infty R(\tau)\cos\omega\tau\,d\tau$$

Setting $\omega = 0$ in this expression and substituting in equation (B3) yield

$$\langle G^2\rangle = \frac{4t}{B_o^2}\int_0^\infty R(\zeta)d\zeta = \frac{\pi\Phi_E(0)}{B_o^2}t$$

Since

$$\langle E^2 \rangle = v_A^2 \langle B^2 \rangle$$

then

$$\Phi_E(0) = v_A^2 \Phi_B(0)$$

and

$$\langle G^2 \rangle = \frac{\pi v_A^2}{B_o^2} \Phi_B(0)t \tag{B4}$$

Suppose a charged particle leaves the origin at time $t = 0$ and executes a random walk in a plane; then the probability P of its being in a small element of area $d\sigma$ at distance r from the origin at time t is given by

$$P(r)d\sigma = \frac{1}{(4\pi Dt)^{1/2}} \exp\left(-\frac{r^2}{4Dt}\right)d\sigma \tag{B5}$$

where D is the diffusion coefficient appearing in the diffusion equation $\frac{\partial P}{\partial t} = D \frac{\partial^2 P}{\partial r^2}$ and

$$\langle r^2 \rangle = 4Dt$$

In the present example, let it be assumed that at $t = 0$ there is an assemblage of particles clustered around the origin with a Gaussian distribution. Let the initial effective radius, defined as the radial distance to those points at which the density is e^{-1} that at the center, be r_o. Then, after time t the density distribution of particles is given by

$$P(r) = \frac{1}{\pi^{1/2}\left(r_o^2 + 4Dt\right)^{1/2}} \exp\left(-\frac{r^2}{r_o^2 + 4Dt}\right)$$

where

$$4Dt = \langle G^2 \rangle = \frac{\pi v_A^2}{B_o^2} \Phi_B(0)t$$

Thus

$$P(r) = \frac{1}{\pi^{1/2}\left(r_o^2 + \frac{\pi v_A^2}{B_o^2}\Phi_B(0)t\right)} \exp\left(-\frac{r^2}{r_o^2 + \frac{\pi v_A^2}{B_o^2}\Phi_B(0)t}\right)$$

Variation of the effective radius of the cloud r_{eff} with time can be expressed

$$r_{eff} = \sqrt{r_o^2 + \frac{\pi v_A^2 \Phi_B(0)t}{B_o^2}}$$

and bearing in mind that

$$v_A = \frac{B_o^2}{4\pi\rho}$$

where ρ is the plasma density,

$$r_{eff} = \sqrt{r_o^2 + \frac{\overline{\Phi_B(0)t}}{4\rho}}$$

By measuring the rate of growth of effective radius with time and knowing ρ the value of $\Phi_B(0)$ can be estimated.

The following symbols are used in this appendix:

$\vec{B}$ magnetic-field vector

$\vec{B}_o$ uniform and time-independent ambient magnetic field

$\vec{E}$ electric-field vector

$\vec{G}$ location of guiding center of gyrating particle

m mass of particle

$R(\tau)$ autocorrelation function of component electric-field fluctuations

r distance from origin

t time

$\vec{v}$ particle velocity

v_A Alfvén wave speed

ζ, η, ξ variables of integration

$\Phi_B(\omega)$ power spectral density of magnetic-field fluctuations as function of angular frequency

$\Phi_E(\omega)$ power spectral density of electric-field fluctuations as function of angular
        frequency

Subscripts:

x,y   components along X- and Y-axis, respectively

REFERENCES

X-1. Shklovskii, I. S.: An Artificial Comet as a Method for Optical Tracking of Cosmic Rockets. Artificial Earth Satellites, Vol. 4, L. V. Kurnosova, ed., Plenum Press, Inc., 1961, pp. 445-465.

X-2. Haerendel, G.; Lüst, R.; and Rieger, E.: Motion of Artificial Ion Clouds in the Upper Atmosphere. Planetary Space Sci., vol. 15, no. 1, Jan. 1967, pp. 1-18.

X-3. Lloyd, Keith H.; and Golomb, Dan: Observations on the Release of a Cloud of Barium Atoms and Ions in the Upper Atmosphere. AFCRL-67-0144, U.S. Air Force, Apr. 1967. (Available from DDC as AD 654 687.)

X-4. Roederer, J. G.; Hess, W. N.; and Stassinopoulos, E. G.: Conjugate Intersects to Selected Geophysical Stations. Goddard Space Flight Center Contributions to the COSPAR Meeting — May 1965, NASA TN D-3091, 1966, pp. 35-131.

X-5. Longmire, Conrad L.: Elementary Plasma Physics. Interscience Publ., 1963.

X-6. Miller, Carlton S.; Parsons, Frederick G.; and Kofsky, Irving L.: Simplified Two-Dimensional Microdensitometry. Nature, vol. 202, no. 4937, June 13, 1964, pp. 1196-1200.

Super-Schmidt, Wallops
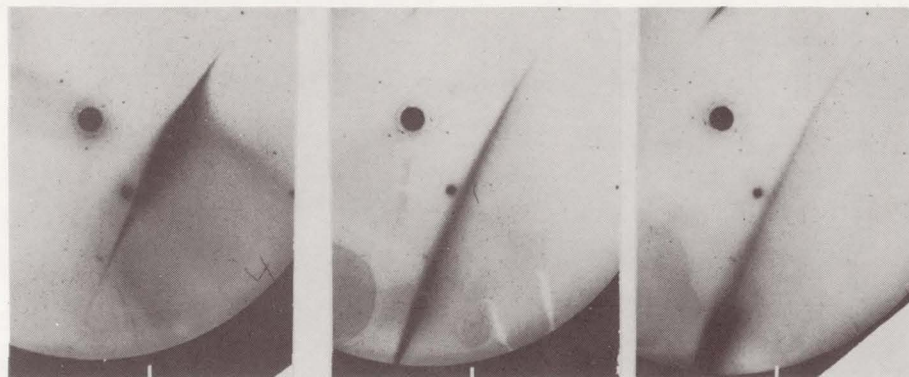
Frame	L14710	L14711	L14712
Exposure duration	7 sec	5 sec	6 sec

K-24, Wallops

Frame	15	21		32
Exposure duration	40 sec	40 sec		2 min

0   2   4   6   8   10

Time after release, min
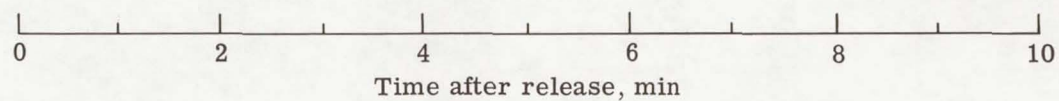
L-71-536

(a) 0 to 10 minutes.

Figure X-1.- Ionized cloud evolution.

Super-Schmidt, Eastville
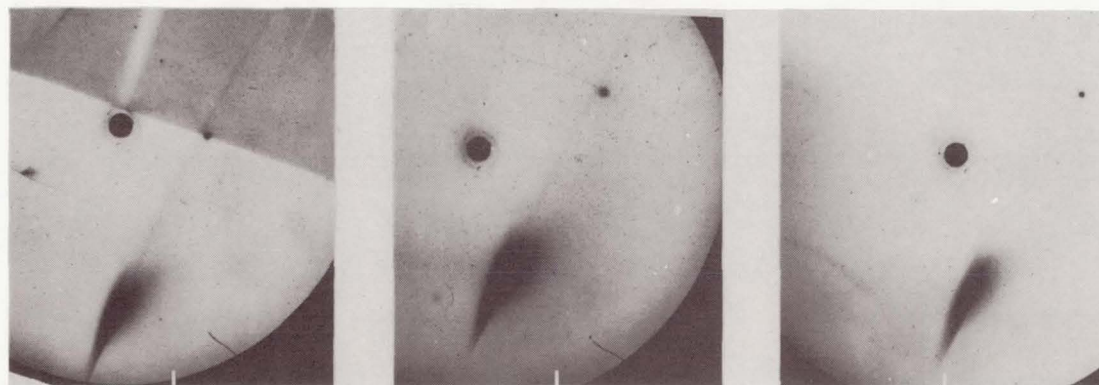
Frame	T7099	T7100	T7101
Exposure duration	5 sec	5 sec	35 sec

K-24, Wallops

Frame	33	34	35
Exposure duration	4 min	1 min	2 min

Time after release, min

L-71-537

(b) 12 to 20 minutes.

Figure X-1.- Concluded.

BC-4, Wallops

Frame	8	9
Exposure duration	1 min	2 min
Time after release	23 min 25 sec	26 min 55 sec

L-71-538

Figure X-2.- Photograph of cloud in later phase of evolution.
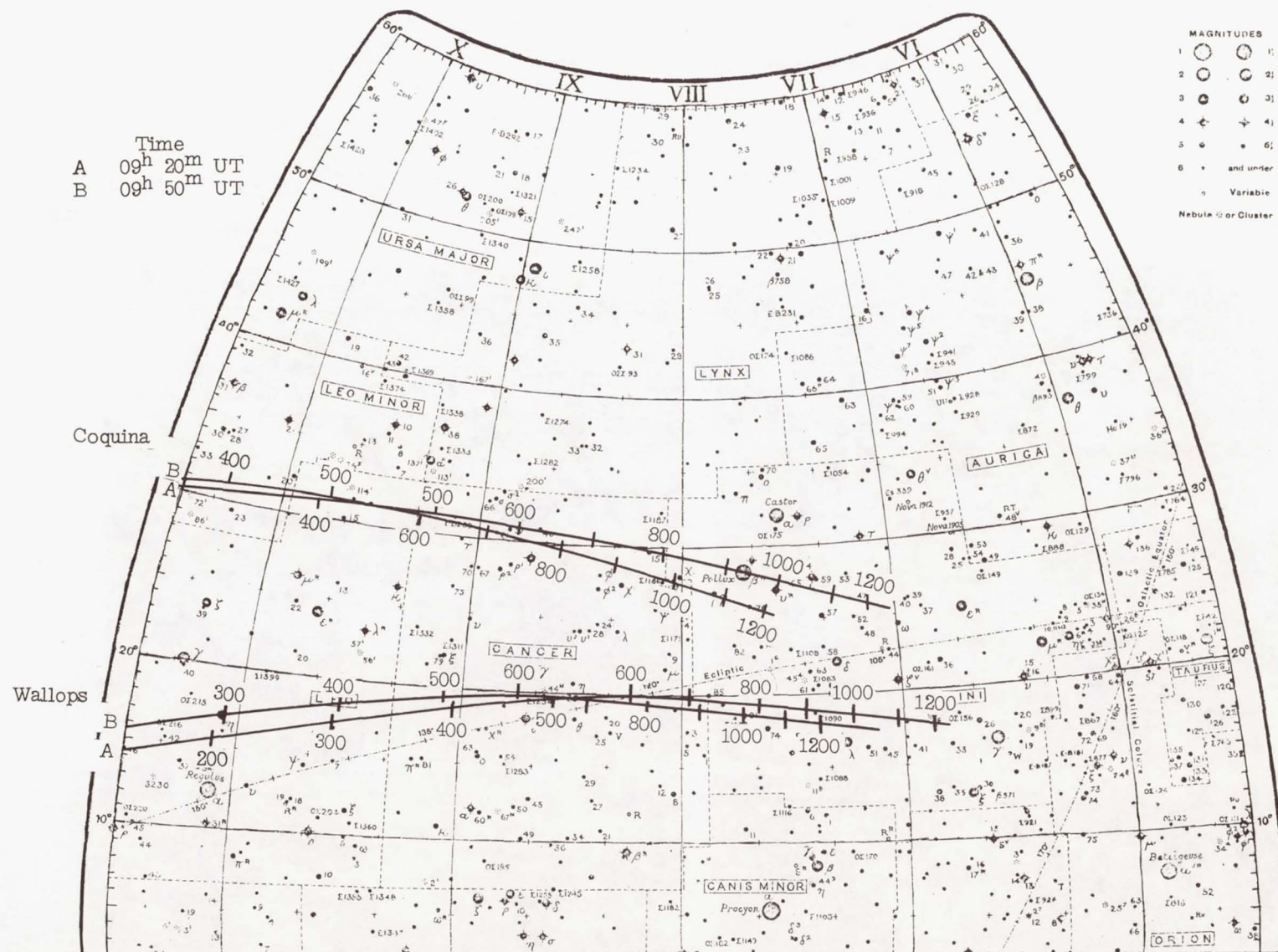
Figure X-3.- Projection of magnetic-field line through release point on celestial sphere as viewed from two observation sites. (Altitude marks at 100-km intervals).
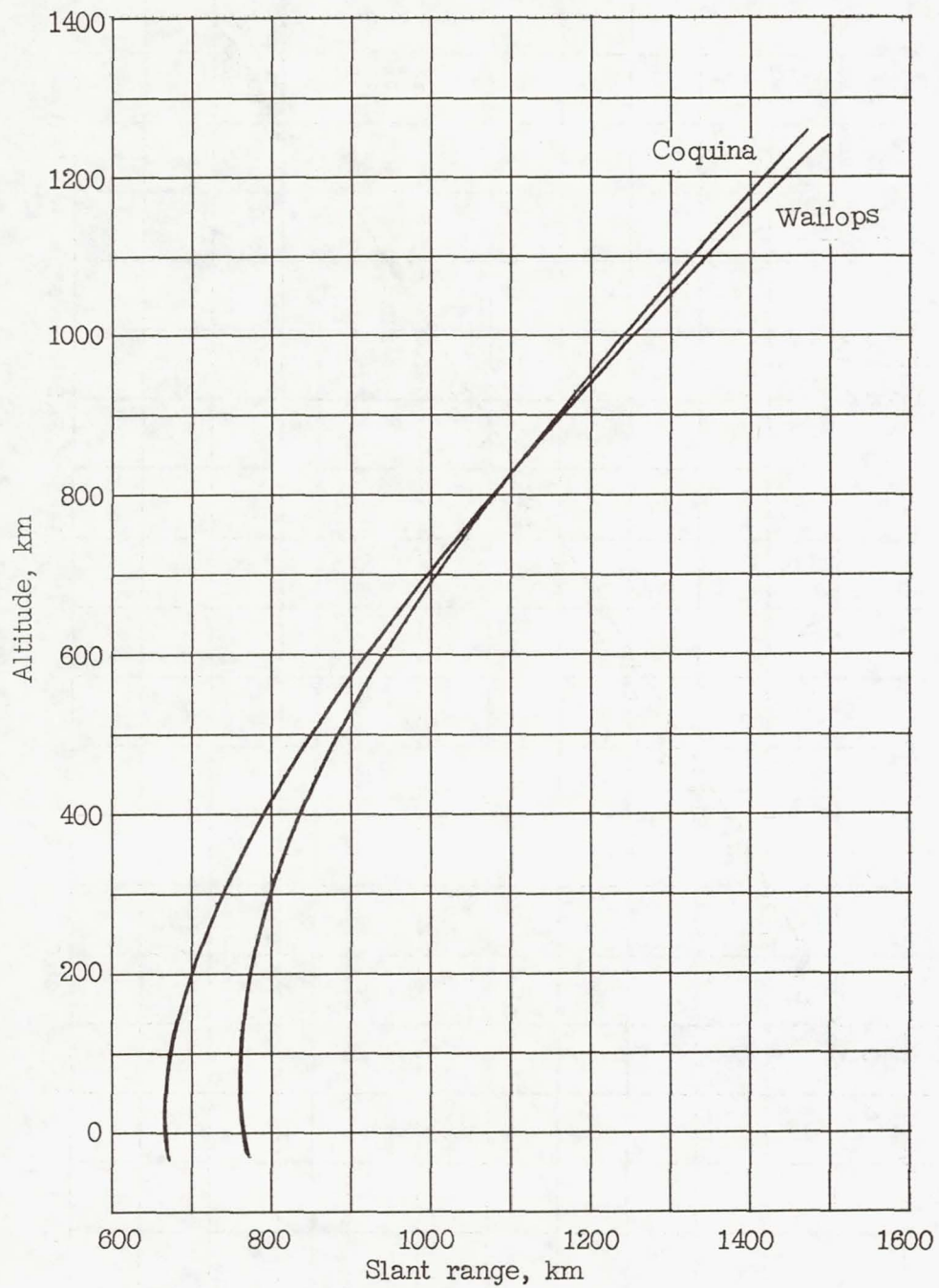
Figure X-4.- Altitude as a function of slant range from two observation sites.
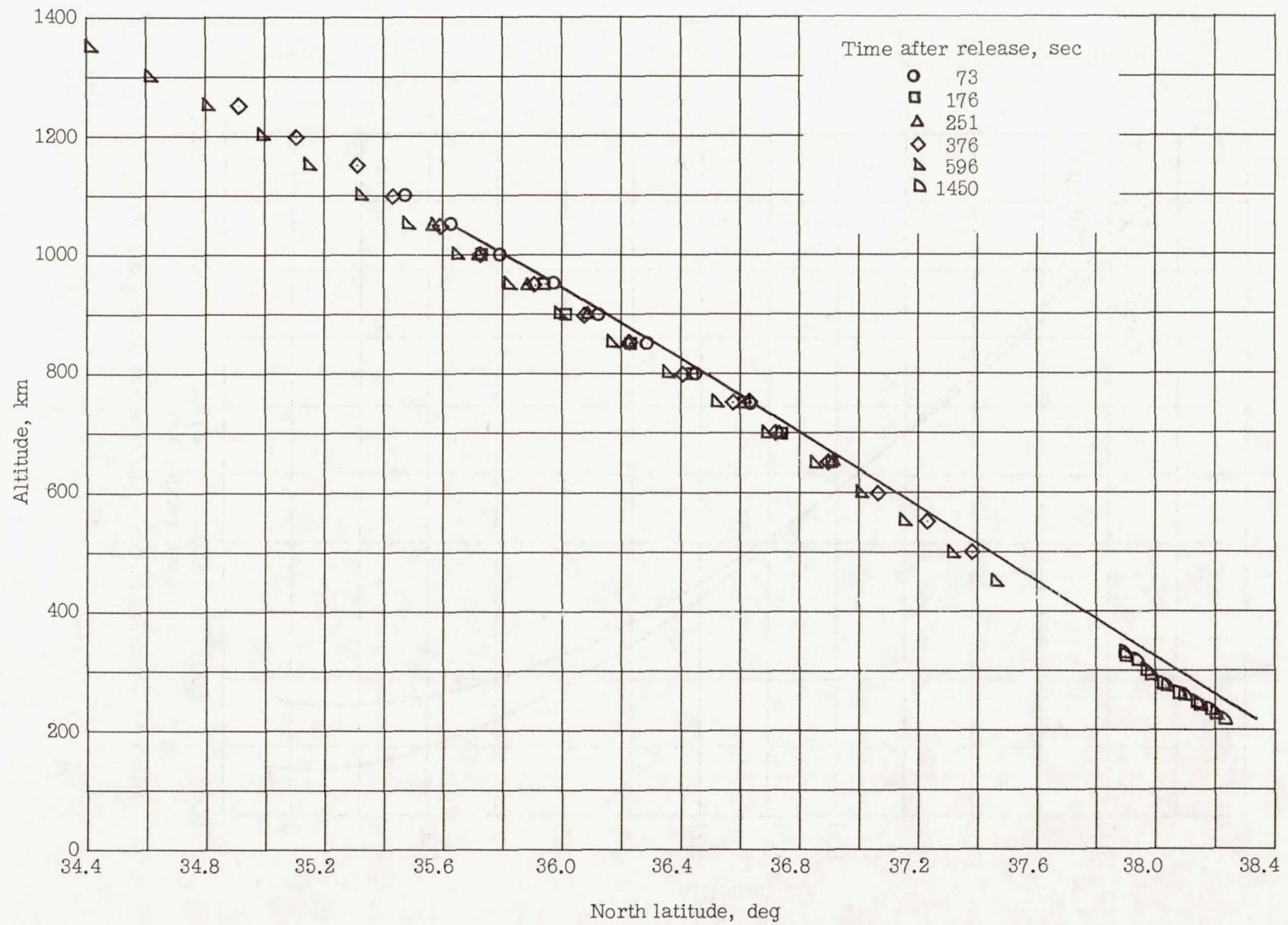
Figure X-5.- Altitude as a function of latitude of points on ionized cloud center line and of time. Javelin second release.
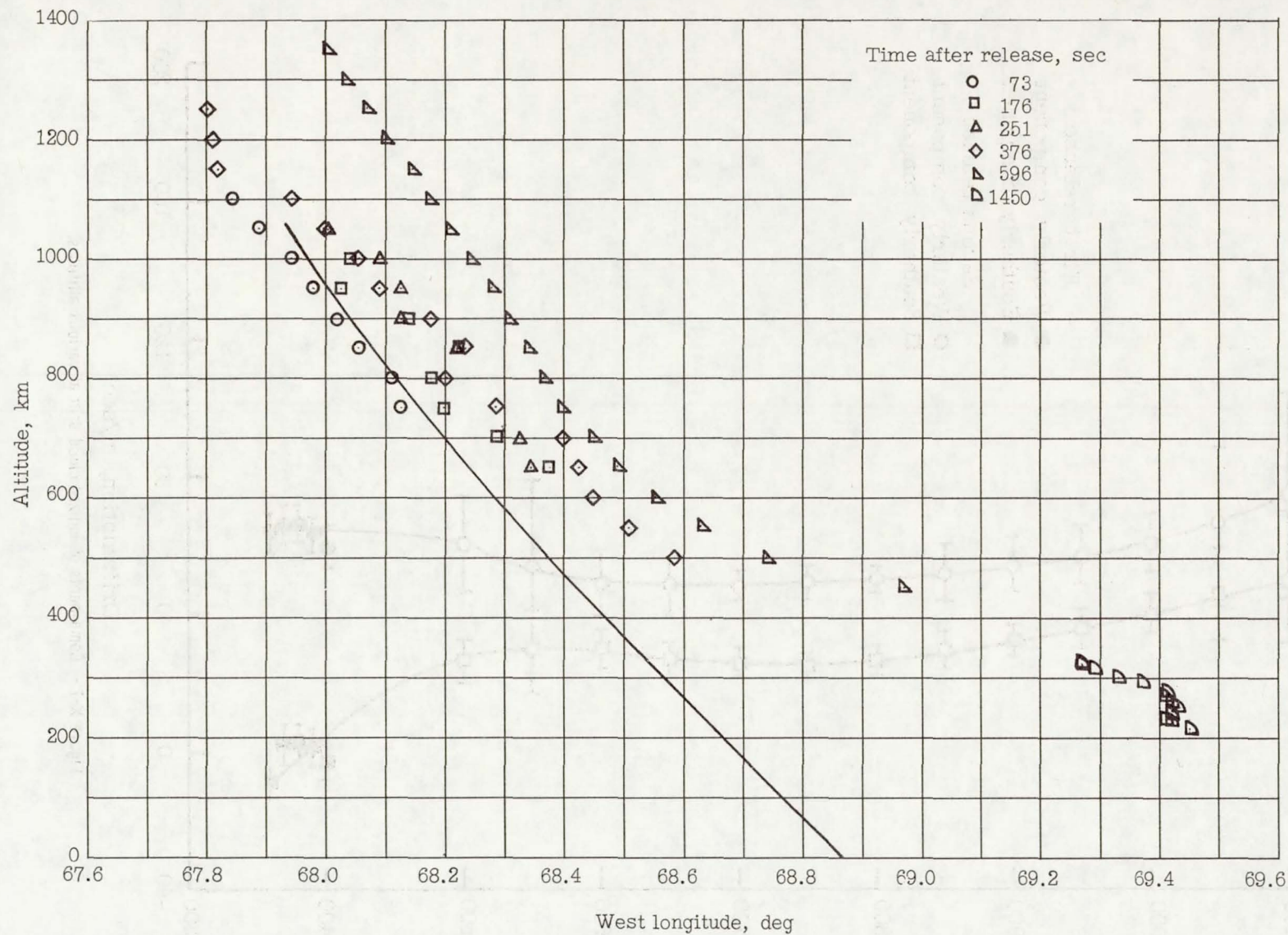
Figure X-6.- Altitude as a function of longitude of points on ionized cloud center line and of time. Javelin second release.
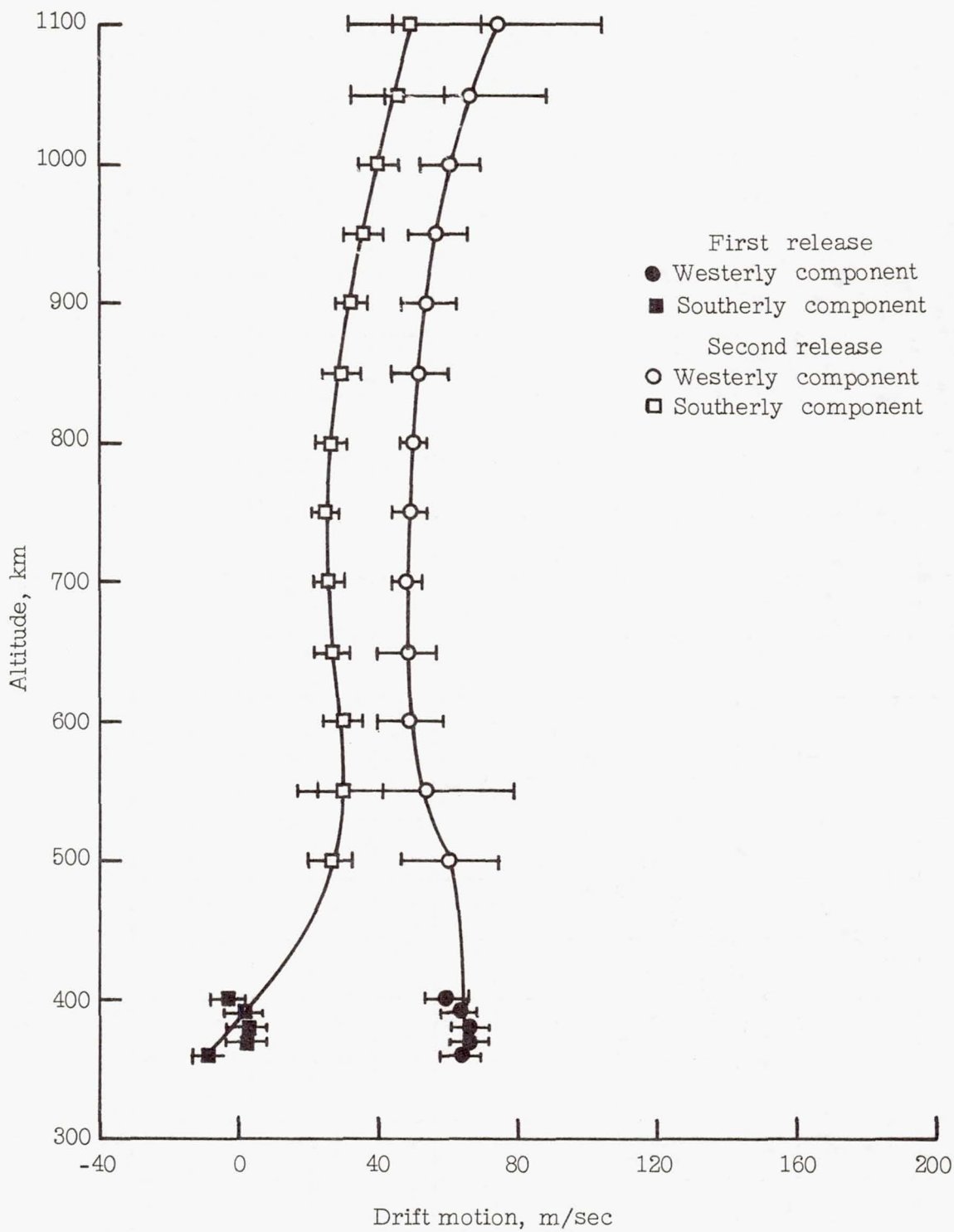
Figure X-7.- Components of ionized cloud drift at various altitudes.
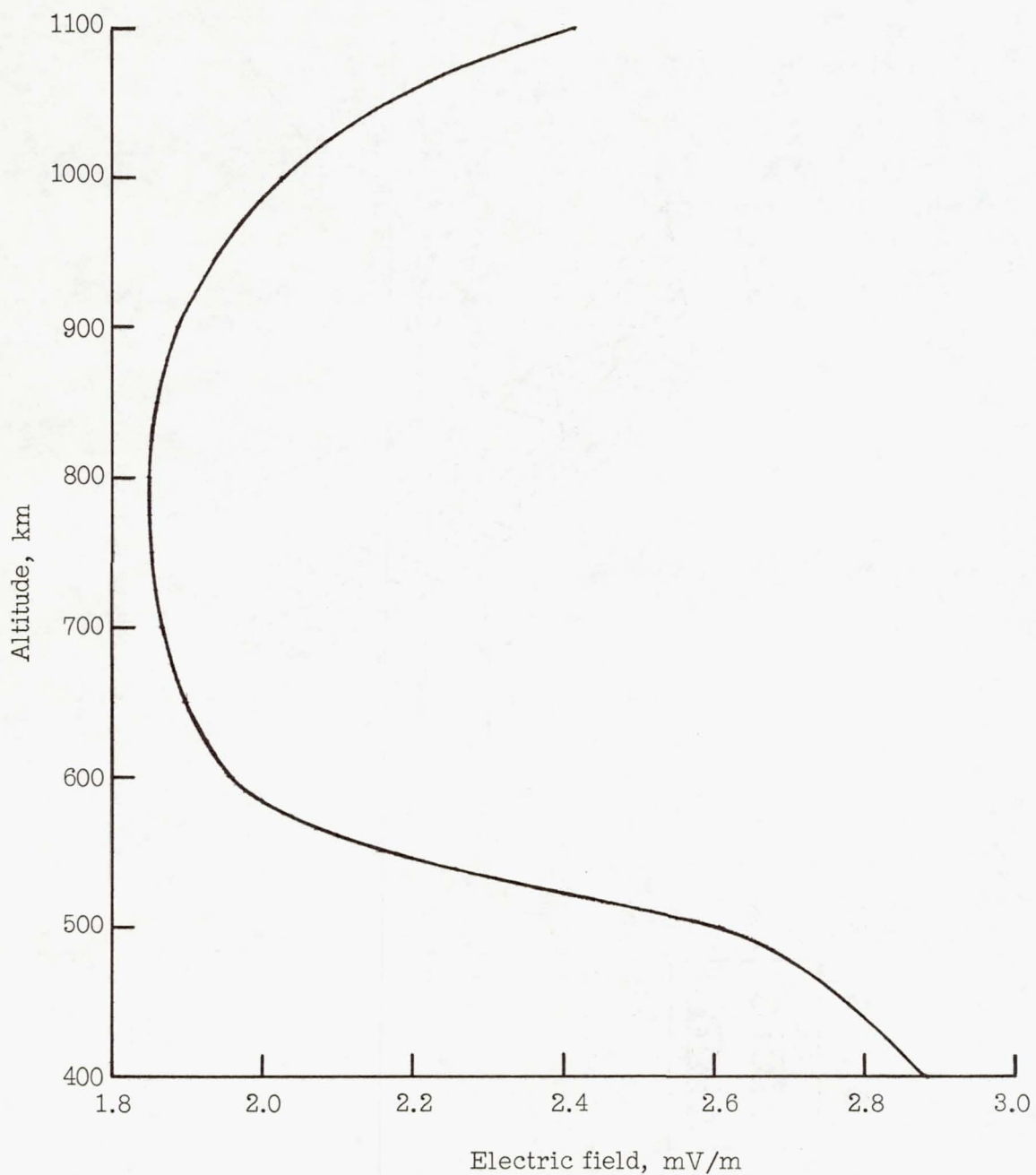
Figure X-8.- Northerly component of electric field as a function of altitude.

134

Ions

Electrons

Cloud cross section,
looking upward along
field lines

Earth surface

Gravity force
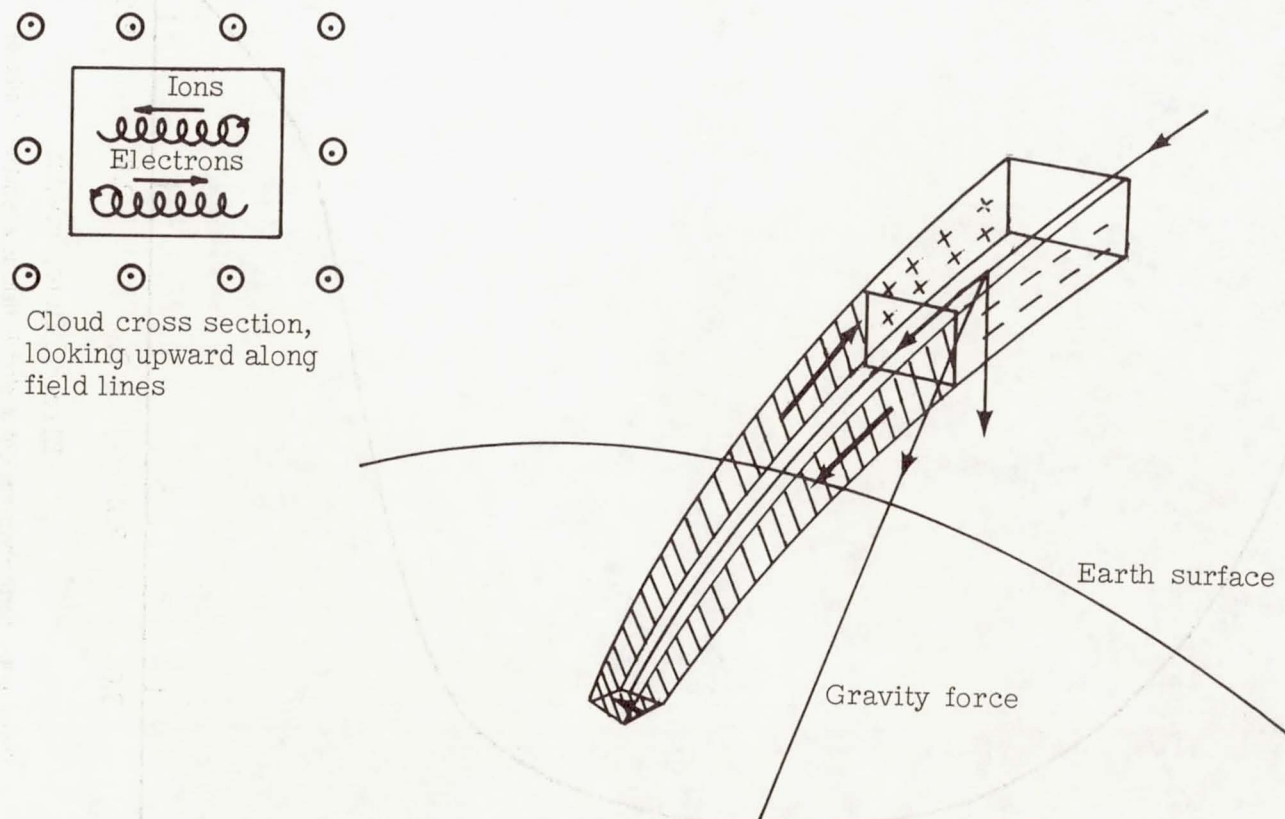
Figure X-9.- Fall of cloud due to polarization.

Exposure duration, 40 sec
Time after release, 3 min 45 sec
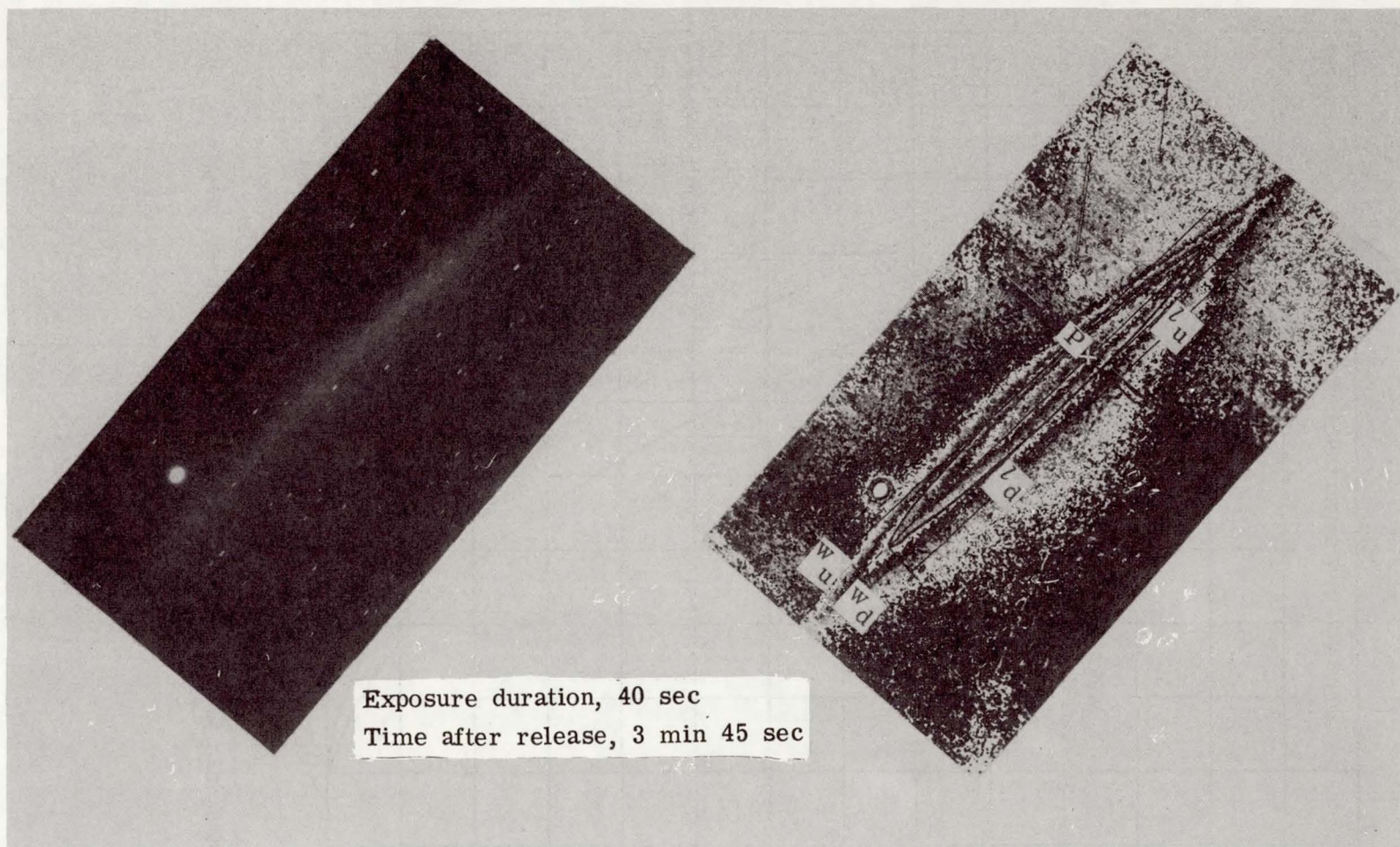
L-71-539

Figure X-10.- Photograph of ion cloud and associated isodensitometer tracing.
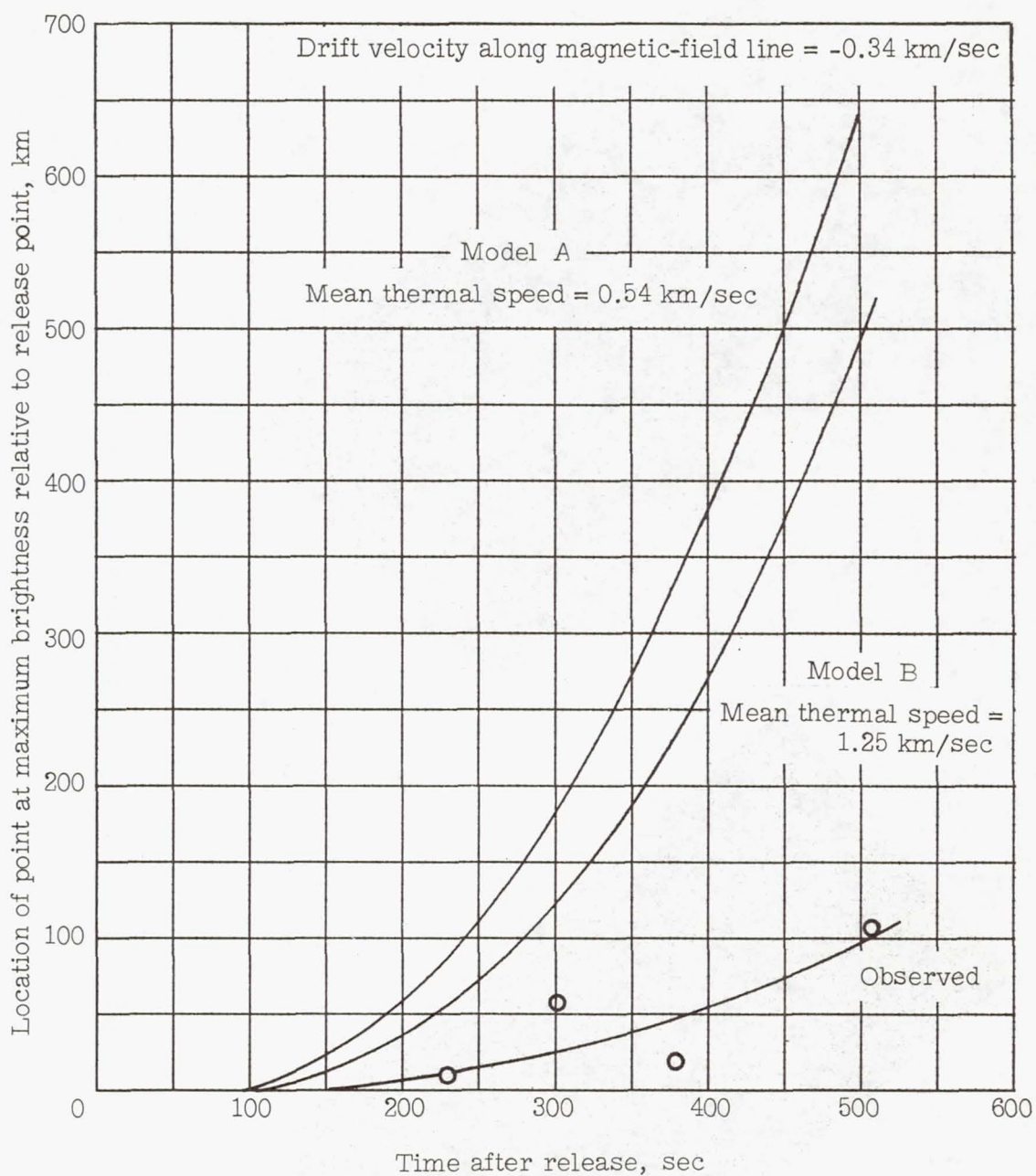
Figure X-11.- Motion of point of peak brightness as viewed from Wallops Island.
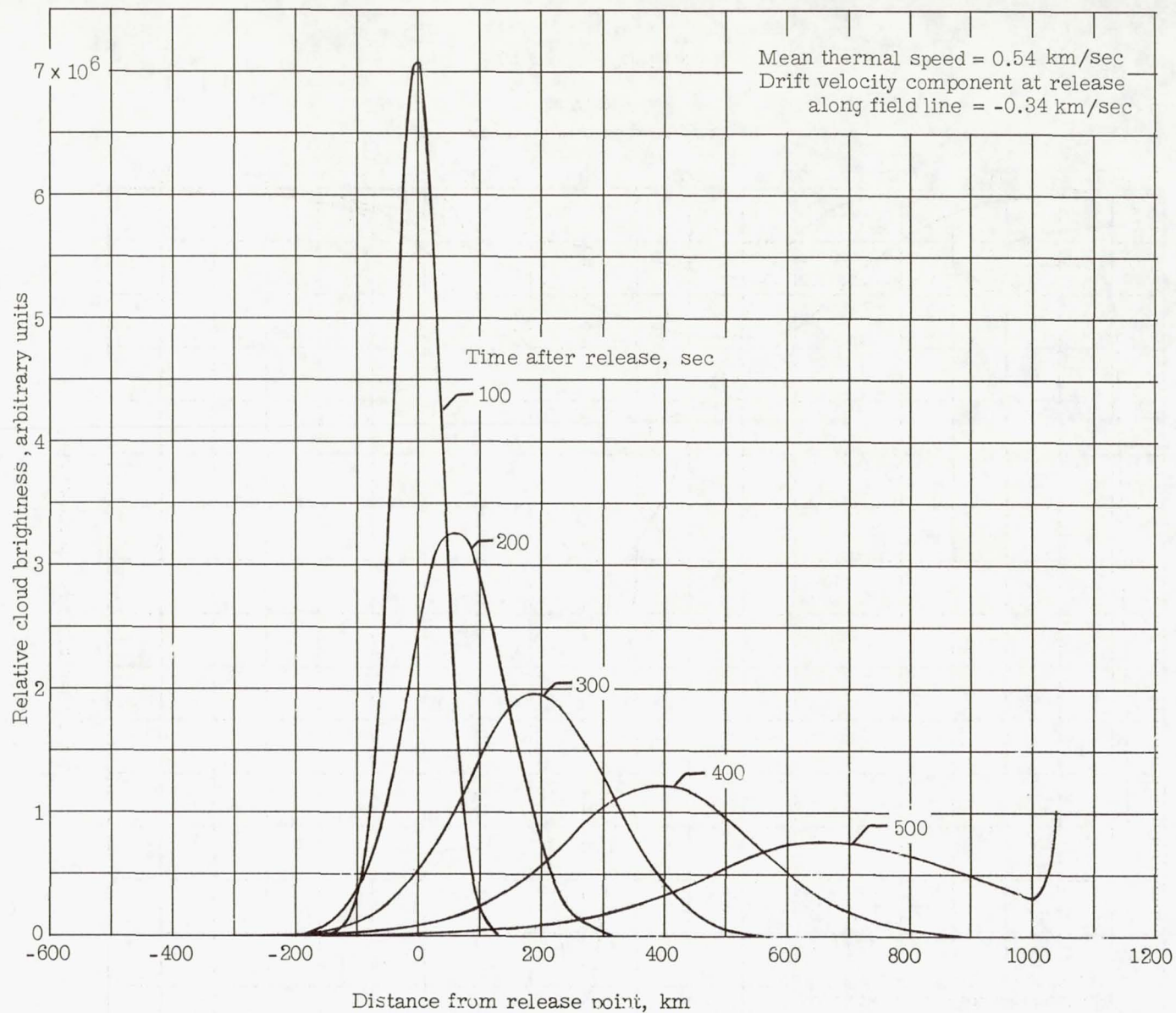
(a) Model A.

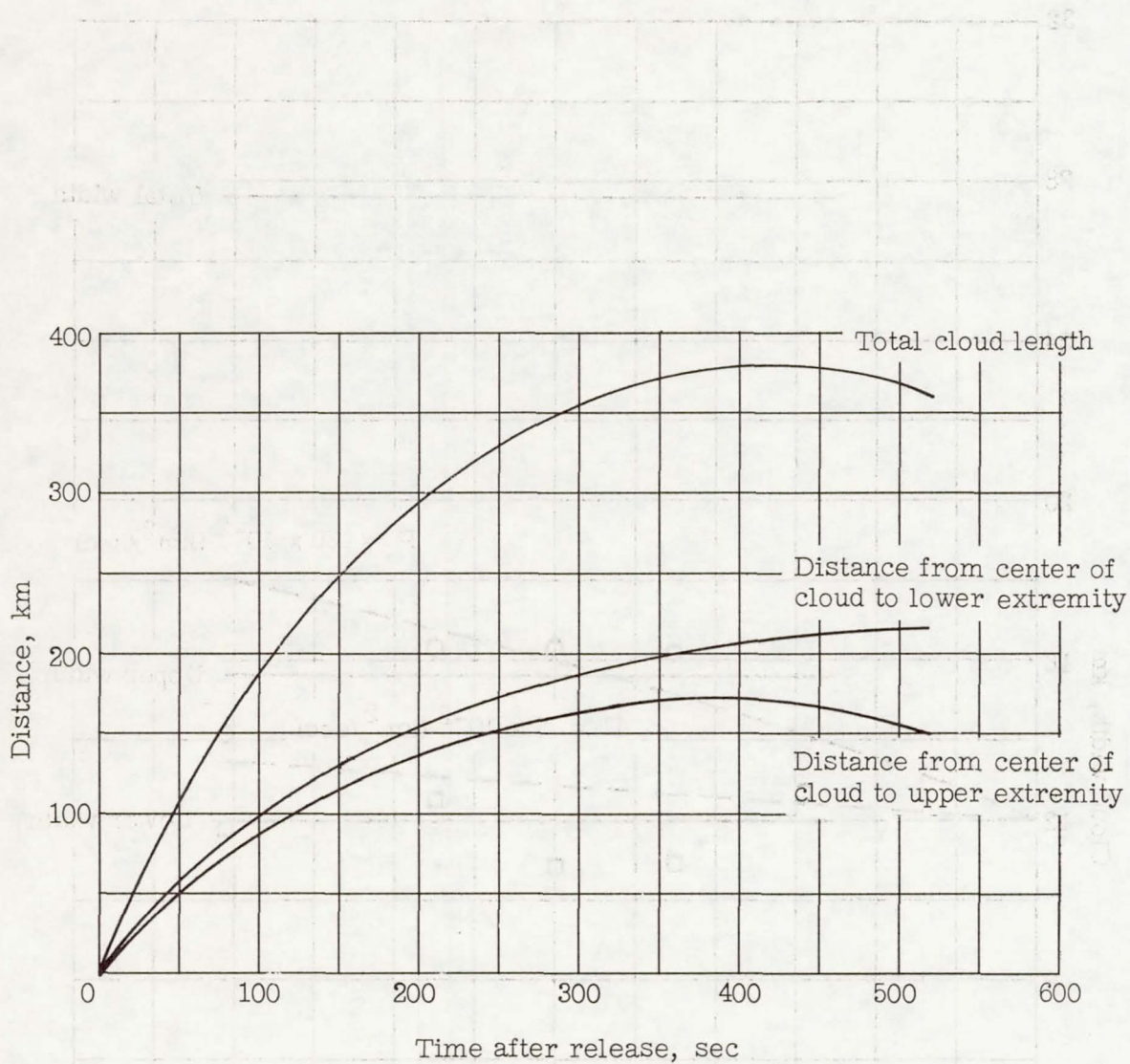Figure X-12.- Theoretical longitudinal brightness distributions as viewed from Wallops Island.

(b) Model B.
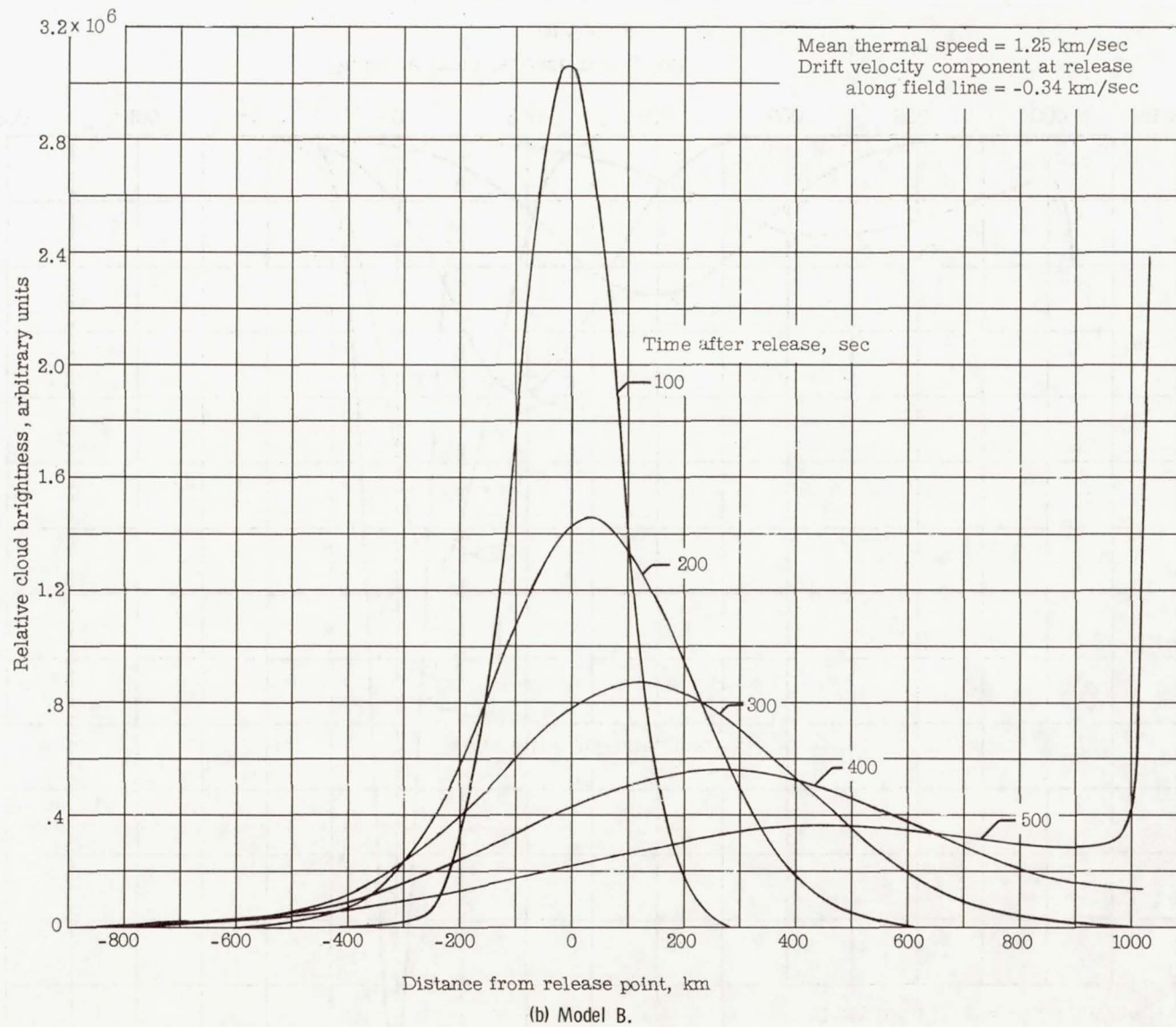
Figure X-12.- Concluded.

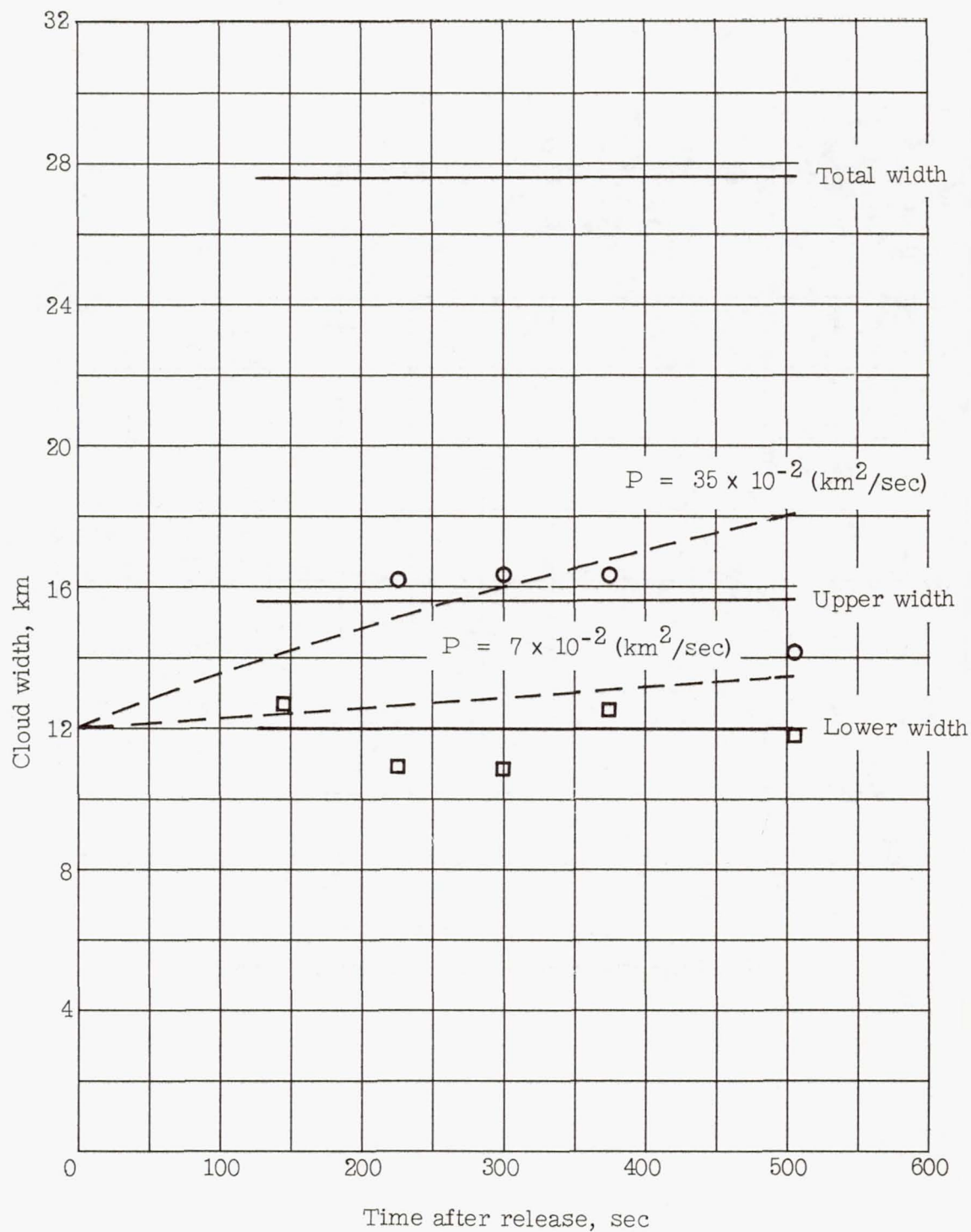Figure X-13.- Longitudinal growth of cloud as a function of time.

Figure X-14.- Lateral growth of cloud as a function of time.

FIRST CLASS MAIL

POSTAGE AND FEES PAID
NATIONAL AERONAUTICS AND
SPACE ADMINISTRATION

"The aeronautical and space activities of the United States shall be conducted so as to contribute . . . to the expansion of human knowledge of phenomena in the atmosphere and space. The Administration shall provide for the widest practicable and appropriate dissemination of information concerning its activities and the results thereof."

— NATIONAL AERONAUTICS AND SPACE ACT OF 1958

NASA SCIENTIFIC AND TECHNICAL PUBLICATIONS

TECHNICAL REPORTS: Scientific and technical information considered important, complete, and a lasting contribution to existing knowledge.

TECHNICAL NOTES: Information less broad in scope but nevertheless of importance as a contribution to existing knowledge.

TECHNICAL MEMORANDUMS: Information receiving limited distribution because of preliminary data, security classification, or other reasons.

CONTRACTOR REPORTS: Scientific and technical information generated under a NASA contract or grant and considered an important contribution to existing knowledge.

TECHNICAL TRANSLATIONS: Information published in a foreign language considered to merit NASA distribution in English.

SPECIAL PUBLICATIONS: Information derived from or of value to NASA activities. Publications include conference proceedings, monographs, data compilations, handbooks, sourcebooks, and special bibliographies.

TECHNOLOGY UTILIZATION PUBLICATIONS: Information on technology used by NASA that may be of particular interest in commercial and other non-aerospace applications. Publications include Tech Briefs, Technology Utilization Reports and Technology Surveys.

Details on the availability of these publications may be obtained from:

SCIENTIFIC AND TECHNICAL INFORMATION OFFICE

NATIONAL AERONAUTICS AND SPACE ADMINISTRATION
Washington, D.C. 20546